2016

Microfluidic Devices with Engineered Micro-/Nanostructures for Cell Isolation

Shunqiang Wang
Lehigh University

Microfluidic Devices with Engineered Micro-/Nanostructures for Cell Isolation

by

Shunqiang Wang

Presented to the Graduate and Research Committee
of Lehigh University
in Candidacy for the Degree of
Doctor of Philosophy

in

Mechanical Engineering

Lehigh University

May 2016

Approved and recommended for acceptance as a dissertation in partial fulfillment of the requirements for the degree of Doctor of Philosophy in Mechanical Engineering and Mechanics.

Student: Shunqiang Wang

Dissertation Title: Microfluidic Devices with Engineered Micro-/Nanostructures for Cell Isolation

_____
Date

_____

Yaling Liu, Dissertation Advisor and Committee Chairman

_____
Accepted Date

Committee Members:

_____

Alparslan Oztekin

_____

Donald Rockwell

_____

Xiaohui (Frank) Zhang

_____

Xuanhong Cheng

Acknowledgements

It was an interesting journey to pursue a Ph.D. degree in Prof. Yaling Liu's group at Lehigh University. This dissertation would not have been completed without supports from my professors, peer friends and my family.

First and foremost, I would like to give my sincere thanks to my advisor, Prof. Yaling Liu. It was Prof. Yaling Liu who provided me the chance to experience such a meaningful and fruitful journey at such a beautiful and prestigious university. He held me to a high standard whiles allowed for lots of freedom on the project selection to capitalize on my strength. I was also always inspired by his accurate foresight on searching for topics which was not only scientifically comprehensive, but practically meaningful. I would like to thanks again for his endless and continuous supports on my career.

I would also like to acknowledge all of my Ph.D. committee members, Prof. Xuanhong Cheng, Prof. Alparslan Oztekin, Prof. Donald Rockwell and Prof. Xiaohui (Frank) Zhang. Without all of your insightful guidance and suggestions, my dissertation would not have been finished to this standard. My special thanks go to Prof. Xuanhong Cheng who guided me through a couple projects. Besides research, she also mentored me and provided lots of critical suggestions on my future career.

Thanks to all of my collaborators, who made the success of these projects possible. Particularly, I would like to thank Prof. Shu Yang at University of Pennsylvania, who provided a tremendous guidance on materials through all projects. Thanks to Dr. Elaine Lee and Dr. Younghyun Cho who helped me a lot in fabricating complex micro/nanopatterns. Their expertise in materials was also greatly appreciated. I would

also like to thank Dr. Yuan Wan, whose expertise in bio-nanomaterials was appreciated. Beyond research, I also appreciate his reference on an internship in China. Great thanks also go to Prof. Susan Perry, who generously allowed me to use her lab for cell culture and microscopy usage. Without this, the dissertation would have been much more delayed.

To my peer colleagues and friends at Lehigh University, I really enjoyed the time to be together with you and will never forget it. Thanks for the tremendous happiness brought by a group of Chinese male labmates including Dr. Jifu Tan, Ran He and Wentao Shi. Thanks for all the great time to be together with other labmates including Dr. Antony Thomas, Jia Hu, Yihua Zhou, Christopher Uhl, Doruk Yunus and Salman Sohrabi. You guys were amazing and thanks for all of the help. Outside of the lab, I was lucky enough to make friends with a sea of talented students, such as Wei Zhang, Yu Song, Dr. Pengda Hong, Hao Wu, Yao Zhang, Yongyang Huang, Han Han, Jiangfan Zhang, Xuanxuan Lv, etc. My special thanks also go to my girlfriend, Yiwei Feng, who also sets a high standard for me which stimulates me to work hard for our future. Her endless support was crucial for me to finish this journey.

Last but not least, I would like to dedicate this dissertation to my family including my beloved parents, Zhiming Wang and Yueping Ye, and my beloved elder brother, Jianshun Wang. Although without very high education, my parents knew the strength of knowledge and provided endless love to support both my brother and me to pursue doctoral degrees. They were open minded which allows us to follow our own heart over the course of the life journey. I would like to thank my brother who continuously

supported me and helped me when confronted with any difficulties. Thanks for taking care of our parents while I could hardly reach them abroad.

Contents

List of Tables

List of Figures

Abstract

Isolation of cells from blood is critical for vast biomedical applications. The focus of this dissertation is on the isolation of circulating tumor cells (CTCs) from patient blood, which contains important prognostic and diagnostic information. Challenges in this field originates from the striking contrast between the rare amount of CTCs (1-10 per mL) and vast other normal cells (millions of white blood cells (WBCs) and billions of red blood cells per mL). Various techniques have been developed to isolate CTCs in the recent decades, while the most demanding clinical requirements lie in two aspects: higher capture efficiency meaning the strong ability to isolate the rare CTCs and higher purity meaning the strong ability to repel all other normal cells. In order to better serve clinical practice, we developed four microfluidic platforms aiming at high capture efficiency and high purity, thus advancing the cancer patient care.

By extending the concept of the hallmark immunoaffinity based grooved-herringbone (HB) chip, we first developed a wavy-HB chip by smoothing the grooved patterns to wavy patterns. The wavy-HB chip was demonstrated to not only achieve high capture efficiency (up to 85.0%) by micro-vortexes induced by HB structures, but achieve high purity (up to 39.4%) due to the smooth wavy microstructures. The HB structures were then further optimized through a refined computational model implemented with cell adhesion probability. The particulate cell transport dynamics was shown to be crucial in determining the optimized geometry for CTC capture. To further enhance the CTC capture, integration of nanostructures was examined due to their intrinsic large surface area-to-volume ratio. By exploring the geometric effects of

nanopillars on CTC capture, we unraveled an interesting linear relationship between CTC capture efficiency and effective nanopillar contact area. We then developed a fabrication approach to deposit nanoparticles on the wavy-HB patterns to form hierarchical micro/nanostructures. The hierarchical wavy-HB chip was demonstrated to achieve a capture efficiency up to ~98% and a high purity performance (only ~680 WBCs per 1 mL blood).

Over the course of the above-mentioned work, there emerges another clinical need which requires captured CTCs to be released and re-cultured for post-analysis such as drug screening. We thus developed two microfluidic chips attempting to achieve this goal. The first platform is an integration of immunomagnetic particles on the developed wavy-HB chip. In addition to the good device performance brought by the wavy-HB patterns, CTCs were able to be released from the capture bed by removing the magnetic field. The collected CTCs labeled with magnetic particles were able to be re-cultured and it was found that these magnetic particles were subject to self-removal during cell proliferations. The second platform was an inclined wavy patterns coated with E-selectin, which was able to form weak adhesion forces with WBCs and CTCs. A proof-of-concept work was performed to demonstrate that WBCs and CTCs were able to be separated along different pathways due to the different adhesion forces and the inclined direction guidance.

With all these developed cancer cell isolation microfluidic chips, we showed our contributions toward effective cancer cell isolation and eventually cancer treatment.

Chapter 1: Introduction

1.1 Background and Motivation

According to the first Global Burden of Disease study, cancer is among the leading causes of death in both developed and developing countries [1]. Among all cancer deaths, Metastasis, defined as the spreading of cancer cells in the primary tumor to distant organs, accounts for the majority while still remains poorly understood [2]. The traditional method to diagnose cancer is biopsy, which studies the tissue or cell sample extracted from the patient [3]. However, the invasive biopsy always accompanies with huge pains, thus bringing lots of discomforts to patients. As an alternative approach, non-invasive liquid biopsy which studies on patient blood sample is attracting more attention nowadays.

Studies of biomarkers for different diseases have been vastly pursued. Three main biomarkers have been identified to effectively indicate cancer status to certain extent, namely, circulating tumor DNA (ctDNA), circulating microRNA (miRNA) and circulating tumor cells (CTCs). For instance, ctDNA was quantitatively measured to evaluate the tumor dynamics which can potentially help clinician make therapy decisions [4]. Circulating miRNA in plasma was used as an indicator to differentiate prostate cancer patients from healthy groups [5]. Similar to these two molecular biomarkers, CTCs behaviors in cellular level have also been demonstrated to act as an effective indicator for cancer status. Clinical studies have been pursued to support the view that

detection of CTCs can be achieved several years before the traditional diagnosis [6-7], thus providing high chances for patients to survive before severe cancer growth. Moreover, amount of CTCs also contains prognostic information, which has been demonstrated to predict overall survival rate in prostate cancer patients [8]. These promising results have inspired researchers to develop various techniques to isolate CTCs from patient blood. Notably, due to the dramatic amount difference of rare CTCs (as few as one in 1 ml blood) and other normal cells (millions and billions in 1 ml blood), CTC detection presents two main technique challenges: 1. How to achieve high CTC capture efficiency, meaning the ability to detect as many CTCs as possible in the blood; 2. How to achieve high selectivity, meaning the ability to differentiate CTCs from nucleated white blood cells (WBCs) and red blood cells (RBCs).

Figure 1-1 Patient blood is injected through a typical microfluidic device for CTC detection.

1.2 Identification of Circulating Tumor Cells and Other Normal Blood Cells

Properties of CTCs and other normal blood cells were summarized in Table 1-1. Although CTCs were generally larger than WBCs, a size overlap still existed for several cancer cell types. So far, the most well-recognized property difference between CTCs and other blood cells were on the cell-specific surface biomarkers [9]. Specifically, CTCs of epithelial origin universally expressed epithelial cell adhesion molecules (EpCAM) which were absent for other blood normal cells, although recent studies revealed that EpCAM underwent a down-regulation through the epithelial-mesenchymal transition (EMT) which brought difficulty in efficiently isolating CTCs based on the anti-EpCAM approach [10]. On the other aspect, there also existed leukocyte common antigens such as CD45 and CD66b. Due to the heterogeneity of CTCs and other normal blood cells especially leukocytes, approaches to isolate CTCs should be carefully selected by taking the most significant difference into account for different applications.

Table 1-1 Properties of CTCs and other normal blood cells

Type / Properties	CTC	WBC	RBC	Platelet	Ref.
Size* (μm)	8-25	6-14	6-8	2-3	[11-14]
Shape	Spherical	Spherical	Biconcave	Biconvex	[14-16]
Stiffness (Young's Modulus)	0.3-1.1kPa	~0.156 kPa	~0.102 kPa	1-50 kPa	[17-20]
Immunoaffinity	Epithelial cell surface markers such as EpCAM	Leukocyte Common Antigens such as CD45 and CD66b			[21-22]

*Note: cell size measurements vary significantly based on the method as well as the cell subtypes.

1.3 Advancing Tumor Cell Isolation using Micro-/Nanotechnologies

As an emerging multi-disciplinary field, nanotechnology raised vast opportunities for cancer detection by interfacing biology, chemistry and engineering. The cell-nanostructure interaction has also been reviewed comprehensively and several basic design principles have been delivered [23]. For the selection of nanomaterials, silicon

nanomaterials are good candidates for CTC study due to their biocompatibility and unique electronic properties [24]. Compared to flat surfaces, nanostructured substrates provide a larger surface area for the immobilization of anti-epithelial cell adhesion molecules (anti-EpCAM), increasing the binding odds between the antibody and membrane receptor and also total binding forces, thus enhancing the CTC isolation efficiency. Moreover, the natural extracellular matrix or basement membrane mimicking nanostructured substrates offered a suitable environment for CTC attachment [25].

Similarly, the advance in microscale technologies also paves new ways for cancer detection. Especially, various established microfabrication approaches including soft lithography allow convenient convergence of multiple disciplinary components [26], which makes it possible to simplify tedious laboratory tests to single device test. With a specific interest, microfluidic in recent years has vastly applied in CTC detections, due to its various advantages including small sample cost, fast result-output, etc. To date, microfluidic devices for CTC detection mainly relies on two different regimes: physical properties (Size [27], density [28] and deformability [29]) or expressions of biomarkers [30-31], which were summarized in Table 1-2. Notably, several hallmark microfluidic devices have been developed by Toner's group: three-generation CTC chips have been developed to achieve highly efficient CTC capture performance. A typical microfluidic setup for CTC capture is shown in Figure 1-1. Other CTC detection techniques have been intensively covered in several review papers [32-33].

Table 1-2 Summary of existed techniques for isolation of CTCs

Isolation Techniques (Structures or Main Mechanisms)		**Efficiency**	**Specificity**	**Ref.**
Immuno-affinity	Microposts	65%	50%	[34]
	Herringbone groves	93%	14%	[35]
Size Difference	Spiral channel	80%	400-680 WBCs/mL	[36]
Density Difference	Density gradient media	70%-90%		[28]
Dielectric Difference	Slanted electrodes	~99%	~94% of WBCs were depleted	[37]

1.4 Limitations of Current Technologies and Research Objectives

Despite all the exciting work reported in literature, there still exist limitations for these technologies in regards of achieving both high capture efficiency and selectivity. For instance, there is a large trade-off between capture efficiency and selectivity for the groove-herringbone device in Toner's work [31]. In another word, high selectivity still remains the main challenge towards achieving high capture efficiency. Specifically, in recent years, integrations of various complex geometry patterns have been proposed to increase CTC interactions with anti-EpCAM coated surfaces. Nagrath *et al.* [9] reported a

microfluidic chip with an array of microposts, which precisely controls the flow path to enhance the CTC-pillar interactions. Due to the inherent property of laminar flow pattern in this platform, the capture efficiency reaches its limitation of 65% in the flow rate of 1.1 ml/hr. To overcome this limitation, approaches to disturb the laminar pattern attracts lots of attention from researchers. Stroock *et al.* [38] firstly reported a staggered herringbone structure to generate passive chaotic mixing. Integration of this structure into microfluidic chips was then widely adopted for CTC capture with significantly increased capture efficiency obtained [31, 39]. While high efficiency was achieved, the selectivity remained poor (14%) [31], likely due to the non-specific trapping of the cell at the sharp corners of the micro-groves.

To overcome these problems and advance tumor cell isolation, this dissertation aims to develop microfluidic devices with novel micro-/nanostructures to achieve both competitively high capture efficiency and selectivity when compared with the ones reported in literature. Specifically, the intermediate goals of this dissertation are described as follows:

(a) Develop and validate a novel microfluidic chip with wavy-herringbone structures for highly efficient and selective isolation of tumor cells.

(b) Optimize the geometry of herringbone structures for highly efficient isolation of tumor cells with an improved numerical model.

(c) Examine the geometric effects of nanopillar height and diameter on isolation of tumor cells.

(d) Develop and validate a novel microfluidic chip with hierarchical micro-/nanostructures for highly efficient and selective isolation of tumor cells

(e) Make a few attempts to develop novel microfluidic chips which are capable to directly isolate CTCs in free suspension

1.5 Dissertation Layout

This dissertation is organized following the roadmap described below. Chapter 2 will discuss the development and prototype of a novel microfluidic chip with wavy-herringbone structures for tumor cell isolation. Both computational prediction and experimental validation will be used to demonstrate the functionality of the proposed chip. Then an improved computational model will be developed and used to optimize the herringbone structures for most efficient tumor cell isolation in Chapter 3. To further improve the tumor cell isolation, nanostructures will be implemented to the developed wavy-herringbone chip. To find the optimized nanostructure geometry, geometric effects of nanopillar height and diameter on tumor cell capture will be examined and geometric guides on nanostructures will also be determined in Chapter 4. By taking the advantages of both micro- and nano-structures in regards of tumor cell isolation, Chapter 5 will discuss the development and prototype of an improved microfluidic chip with hierarchical micro-/nanostructures for better tumor cell isolation. In Chapter 6 and Chapter 7, two attempts will be discussed to directly isolate CTCs in free suspensions. Lastly, Chapter 8 will present a summary of the dissertation and indications for future work.

Chapter 2: Wavy-HB CTC Chip

2.1 Introduction

In the past few decades, microfluidic devices have been extensively employed in the fields of chemical, biomedical and environmental engineering, summarized in a few review articles [40-42]. The device miniaturization using microfluidics leads to low reagent cost, low waste, fast reaction process and the predictable laminar flow pattern in microscale fluid flow [41, 43-45]. One exciting application is the early-stage detection of circulating tumor cells (CTCs) [34, 46], which are rare cells originally shed from a solid primary tumor and ultimately form a secondary tumor site in the course of blood circulation. Increasing studies have also shown strong clinical relevance of CTC amount for early cancer diagnostics [47], metastasis progress [7, 48] and therapy response [49-50]. In various common cancers, including breast cancer, pancreatic cancer and colorectal cancer, CTCs have been found to overexpress epithelial cell adhesion molecules (EpCAMs), which are not found in normal cells. Given the EpCAM expression difference, researchers have designed various microfluidic channels coated with anti-EpCAM for immuno-affinity based CTC detections [34, 51-53]. However, the challenge still lies in the efficiency of detection due to the scarce amount of CTCs, typically 1-10 cells vs. 4 billion red blood cells (RBCs) and 4 million white blood cells (WBCs) per 1 mL of patient blood. The typical laminar flow in a microfluidic device will not be able to address the challenge, especially for limited time and channel length.

Passive mixing within microfluidic devices has been proposed to induce increased collisions between cells and anti-EpCAM coated channel surfaces, thus enhancing the

cell capture [54-55]. One hallmark micro-mixer, first introduced by Stroock *et al.* [56], is the staggered grooved-herringbone (HB) mixer. The asymmetric grooved-HB structures stretch and fold the flows in the cross-section, yielding chaotic flows that are essential for generating efficient mixing. By adopting this principle, Stott *et al.* [35] developed a HB-chip for high-throughput and efficient CTC capture, where in-vitro clinical utilities have been demonstrated with a capture efficiency of up to 79% under low shear rates of ~13/s. The cell dynamics in the micro-vortex flow induced by grooved-HB structures have also been studied extensively [57-58], which provide design guidelines for specific applications. Moreover, the structure simplicity of the grooved-HB structure allows for its wide integration into various platforms to enhance the cell-surface interactions. Wang *et al.* [54] integrated grooved-HB structures on the top of nanostructured substrates, where the chaotic effect induced by grooved-HB dramatically enhanced the CTC capture performance with capture efficiency of up to 95% at a flow rate of 0.5 mL/h. Similar enhancements have been demonstrated in the NanoVelcro chip developed by Tseng's group [59-60] and CTC chips developed by Fan's group [55, 61].

Besides capture efficiency, purity should also be taken into consideration when evaluating the performance of a CTC capture device. Purity is the ability to resist non-specific capture of WBCs, and is normally defined as the ratio of the number of captured CTCs to the total number of captured cells. It is highly desired to achieve both high capture efficiency and high purity [32]. Yet, the trade-off between CTC capture efficiency and purity remains a universal problem for existing microfluidic platforms. In general, cell adhesion probability on a surface decreases with increased shear rate [62-63], which applies to both CTCs and WBCs. In another word, higher CTC capture efficiency

is normally achieved under lower shear rate, under which WBCs tend to be non-specifically captured, resulting in a relatively low purity. This is especially true for the grooved-HB microfluidic chip, where trough regions with ultra-low shear rate (as shown in Figure 2-1(e)) have a high chance to trap WBCs. As a result, although high capture efficiency up to 79% was obtained in grooved-HB device, the purity was sacrificed down to 14% [35]. One strategy to improve purity is to eliminate the low shear sharp corners, which are prone to non-specific binding for WBCs while keeping the chaotic effect provided by HB structures. Here, we fabricated a microfluidic chip integrated with wavy-HB structures (Figure 2-1(a)), where the smooth waves are expected to allow for smooth shear rate transitions and eliminate the ultra-low shear rate regions. *In vitro* tests with whole blood spiked with CTCs were performed in both grooved-HB chips and wavy-HB chips. The results show that similar capture efficiency is obtained in both chips, while the wavy-HB chip showed a 39.4% purity, significantly higher than the 25.7% in the grooved-HB chip under the same shear rate of 400/s. In the high shear rate range (200/s to 400/s), the wavy-HB chip showed up to two-fold higher purity than the grooved-HB chip.

In the following sections, the working principle for the proposed wavy-HB chip is first introduced. The capture performance was simulated numerically and compared with the grooved-HB chip. Then the fabrication method of wavy-HB chip is described followed by its morphology characterization. *In vitro* tests in both grooved-HB chips and wavy-HB chips were investigated and the test results were compared side-by-side in both chips. Cell distribution profiles were also studied to help understand the performance differences between the grooved-HB chip and the wavy-HB chip.

2.2 Method and Materials

2.2.1 Microfluidic Chip Design, Fabrication and Assembly

Both grooved-HB chip and wavy-HB chip consist of a patterned polydimethylsiloxane (PDMS) layer at bottom and a PDMS channel layer on top, which are aligned and bonded after O2 plasma treatment. The grooved-HB PDMS layer was replicated from patterned master, which was fabricated by photolithography method [64]. The optimized device layout was sent to CAD/Art Services to make the photomask, which was then used to make the patterned master with SU8-2050 (MicroChem, Newton, MA). The thickness of the pattern was controlled by the spinning speed of SU8 according to the datasheet provided by vendor, which determined both the channel depth and the groove depth. The pattern thickness was measured by a profilometer (Alpha-Step D-100 stylus profiler). To facilitate release of the PDMS mold to the SU8 master, 1H,1H,2H,2H-Perfluorodecyltrichlorosilane (FDTS) (Alfa Aesar) was coated on master by vapor deposition [65].

A reflow approach, which has been widely used to make micro-lenses [66-67], was adopted and modified to make the wavy-HB master, as shown in Figure 2-5(a). In detail, a grooved-HB PDMS layer was first fabricated as mentioned above, which was then bonded to a glass slide to ensure a relatively stiff PDMS layer. Meanwhile, an SU8 photoresist layer was spun on a silicon wafer, which was soft baked at 95 °C to remove solvent. The grooved-HB PDMS layer was then placed onto the photoresist at 95 °C for replication via capillary flow, during which air bubbles were carefully removed by pressing the bonded glass. The whole device was cooled down to room temperature (RT) and an uncured photoresist grooved-HB pattern was thus replicated by peeling off the

PDMS layer. To create smooth wavy pattern, the uncured photoresist pattern was heated to 55 °C, where the photoresist could reflow to a certain extent. The heating period was well controlled and checked every 10 s by optical microscope till the waves were formed (typically 7-10 mins). Devices with different total heating periods were fabricated to ensure at least one of the resulted undulations was of the desired dimensions. Finally, the wavy-HB SU-8 pattern was UV cured at 365 nm with an intensity of 4.6 mW/cm^2, followed by a treatment of FDTS. The micropattern topography and morphology was examined by a profilometer and an optical microscope. Due to thermal reflow, the final pattern depth decreased from 63 μm (grooved-HB) to 45 μm (wavy-HB). To ensure the wavy-HB chip has a similar depth of the grooved-HB chip for later cell capture comparison, we used the grooved-HB chip with a groove depth of 45 μm.

2.2.2 Cell Culture and Blood Preparation

HCT-116, a colorectal cancer cell line, was used as a model CTC cell line in this study. Cultured at 37 °C, HCT-116 cells were incubated with Dulbecco's Modified Eagle's Medium (Sigma Aldrich) supplemented with 10% fetal bovine serum (Invitrogen) and 1% penicillin/streptomycin (Sigma Aldrich). Media was refreshed every 2-3 days. When cells reached 80-90% confluency, they were subcultured and 0.05% Trypsin–0.53 mM EDTA was used for cell detachment. Fresh human whole blood samples with Li Heparin as the anti-coagulant agent were purchased from Innovation Research.

2.2.3 Cell Capture Test and Imaging

Before the cell capture test, both the grooved-HB chip and the wavy-HB chip were functionalized with anti-EpCAM following a chemistry reaction described in

literature, as illustrated in Figure 2-1 [68]. Briefly, 5% (v/v) 3-mercaptopropyl trimethoxysilane (MPTS) in ethanol was first injected through the microfluidic chips for 30 mins. at RT. Chips were then incubated with 0.01 mM N-y-maleimidobutyryloxysuccinimide ester (GMBS) in ethanol for 30 mins at RT, followed by an overnight incubation of 10 µg/mL NeutrAvidin in phosphate buffered saline (PBS) at 4 °C. Within 4 hrs of the flow test, the devices were incubated with 10 µg/mL [68-69] biotinylated goat anti-human EpCAM in 1% (w/v) bovine serum albumin (BSA) in PBS solution for 2 hrs at RT, followed by a purging process with 3% BSA solution containing 0.05% Tween20 for 30 mins. Between each injection, PBS or ethanol solution was used to flush away any unbound molecules in the suspension. To ensure the consistency for each device, all the injections were performed using a syringe pump (Harvard Apparatus) at a flow rate of 5 mL/hr.

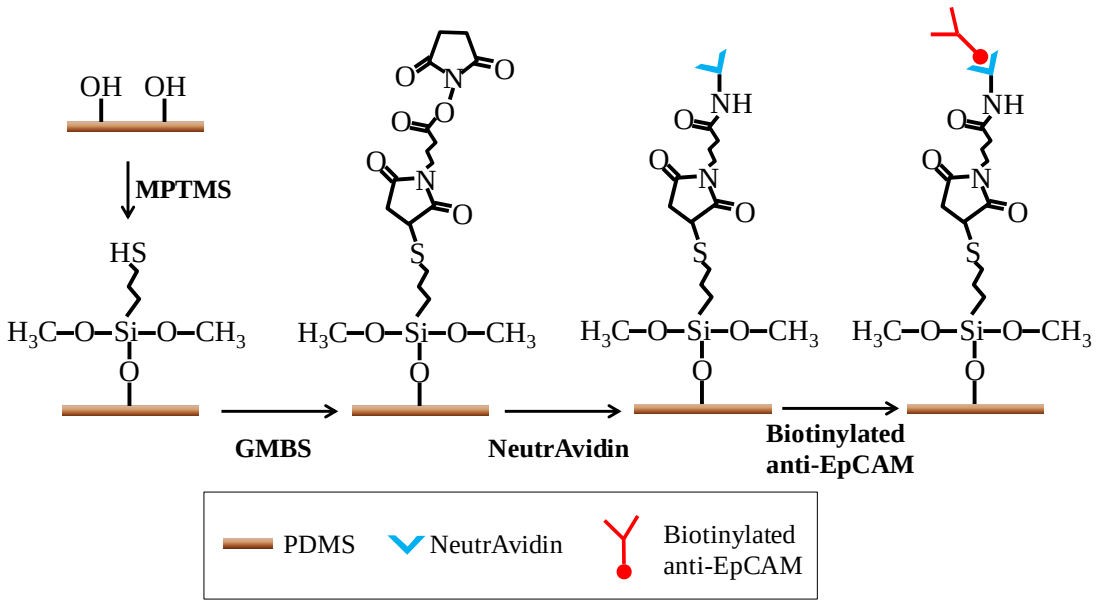

Figure 2-1 Illustrative flow chart of surface functionalization on PDMS.

HCT-116 cells detached from culture disks were diluted in PBS solution to 103-

105/mL which was calculated by a hemocytometer. To reduce the cell sedimentation in the tube during the flow test, 4 mg/mL alginated PBS solution was adopted which mimics the blood viscosity [70]. For blood tests, pre-labeled HCT-116 cells with cell-tracker (Life Technology) were spiked into blood and fully mixed by gentle pipetting. Cell samples of 50-250 µL were then injected into the microfluidic chips using a syringe pump in prescribed flow rates. Immediately after the cell injection, PBS buffer solution was injected to remove all suspended cells at a flow rate of 3.6 mL/hr with a total volume of 1 mL. Captured cells were then fixed using 4% paraformaldehyde for 25 minutes at RT and incubated with 0.2% Triton X-100 in PBS for 5 minutes to permeabilize cell membranes. Cell nuclei were subsequently stained with DAPI solution for 20 minutes. After finishing the staining process the devices were flushed by PBS solution and kept at 4 °C. To differentiate tumor cells and WBCs, only cells that were cell-tracker positive and DAPI positive were treated as HCT-116 cells, while cells which were cell-tracker negative and DAPI positive were treated as WBCs. Only cells with intact morphology were considered.

2.2.4 Cell Viability Assay

Viability of captured tumor cells was studied by performing LIVE/DEAD assay. Specifically, a cocktail including 1 µM calcein-AM and 1 µM ethidium homodimer (EthD-1) was flushed through the microfluidic chip. After 25 mins' incubation at RT, PBS solution was added to remove the LIVE/DEAD cocktail. Stained tumor cells were then observed under fluorescent microscope. Only cells which are calcein-AM (+) and EthD-1 (-) are treated as live, while cells which are EthD-1 (+) are treated as dead. Cell

viability was defined as the ratio between the number of live cells and the total number of captured cells.

2.2.5 Finite Element Simulation

Customized MatLab codes combined with Comsol simulations were developed [71-72] to simulate the cell dynamics in the microfluidic chips. Following previous simulation studies [58], cells were treated as particles following streamlines to simplify the simulation process. Cell-cell/cell-fluid interactions and the non-Newtonian effects are over the scope of this study and not included in this model. In the Comsol model, sidewalls were set as the periodic boundaries, which mimic the real setup where there are repetitive parallel units. At least 282143 meshes were used to ensure its accuracy and all the simulation results were then exported to MatLab for computing the particle motion. Cells were treated to be captured when the cell-surface distance was smaller than the radius, i.e., 10 μm.

2.3 Results and Discussions

2.3.1 Working Principle

The wavy-HB chip is different from the traditional grooved-HB chip by replacing the sharp corners in the latter with smooth wavy structures. The wavy-HB chip consists of repetitive units, each of which has six wavy-HB structures in the 1st-half cycle staggered with another six wavy-HB structures in the 2nd-half cycle, as depicted in Figure 2-2. The design parameters were selected based on prior studies on the mixing effect of the grooved-HB chip [73-75]. However, we note that most of prior studies have not considered the inherent particulate properties of cells: the main contribution for

enhanced cell capture comes from cell-surface direct collisions while the center rotational flow might not contribute to the cell capture. To our knowledge, only one pilot study by Forbes *et al.* [58] provides a design guide explicitly based on cell-surface interactions. By using the particulate model described in the Methods section, the optimized parameters were determined and we found that most optimized parameters are similar to those in the previous mixing studies: channel height of 50 μm in the range of 30 μm-110 μm, wave amplitude (equivalent to half of groove depth) of 22.5 μm in the range of 6 μm-440 μm, short/long arm length of 100 μm/200 μm in the range of 100 μm-800 μm and oblique angle between HBs and the flow axis of 45 degrees in the range of 30°-150°. Detailed geometrical information is shown in Figure 2-2(c-e). The numerical optimization processes for these parameters are not discussed in detail in this study except for the wavelength, which differs from other literature work. As shown in Figure 2-3, the pattern period was optimized in the range of 40 μm-240 μm, with 160 μm selected in this study for the concept validation of the proposed wavy-HB chip.

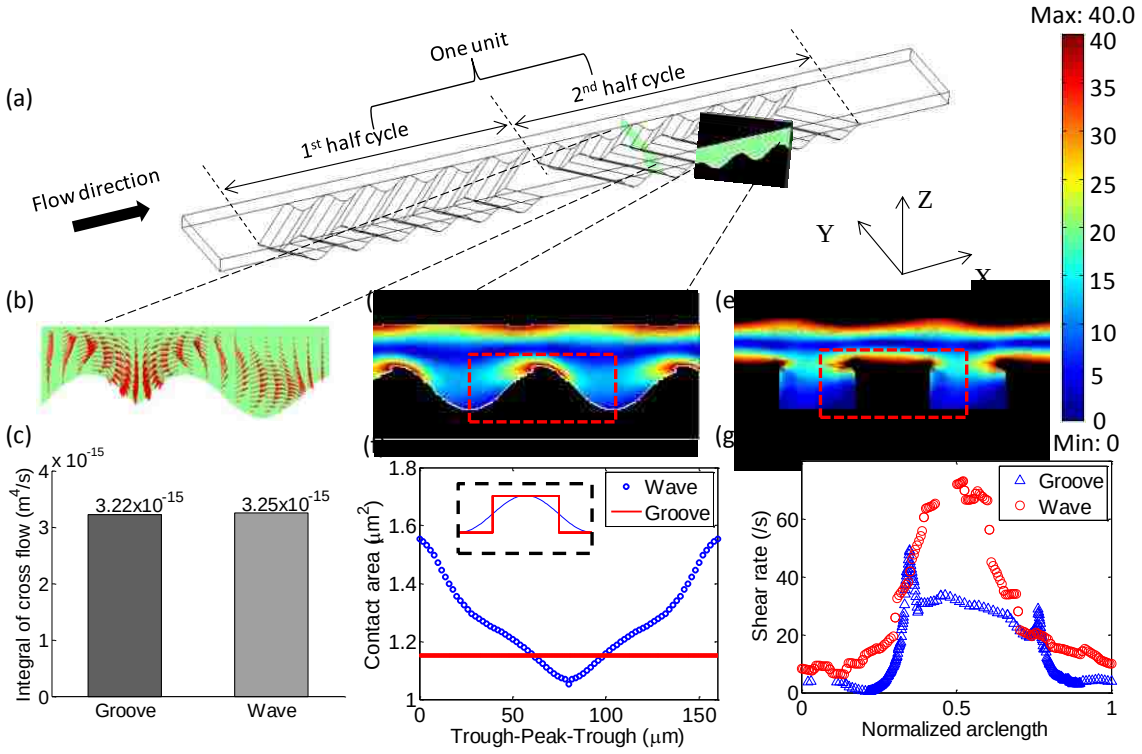

Figure 2-2 Working mechanism of the wavy-HB microfluidic chip for highly efficient and selective CTC capture. (a) Schematic figure of a single unit of the wavy-HB pattern. (b) Flow velocity components in the cross-section illustrate the micro-vortex. (c) Integral of cross flow over the unit for both grooved- and wavy-HB patterns. The contours of the shear rate in (d) wavy- and (e) corresponding grooved-HB chips. The color bar is shown with the unit of /s. The distortion of the images is due to cut-off of the range in order to make the color map clear. The rest area over the range is filled in black. (f) Theoretical analysis of cell-surface contact area along one period for both wave and groove patterns. For the groove pattern, two data points (2.31 μm^2) are not shown when a cell is located in the intersection between the bottom and the side wall. (g) The shear rate along the arc length of both a groove and wave period (trough-ridge-trough: indicated by the dashed line in (d) and (e)) with a distance of a cell radius away from the surface. Here, the arc length is normalized to its period for both patterns.

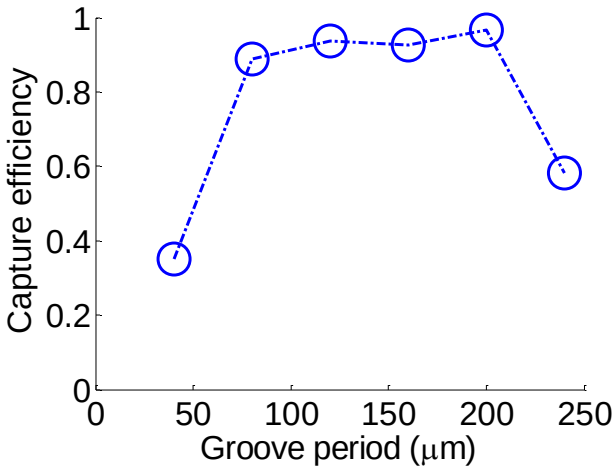

Figure 2-3 Numerical simulation reveals the effect of the groove period on capture efficiency.

With the prototype model built, the working mechanism of the wavy-HB chip is explained from capture efficiency and purity. Capture efficiency is defined as the amount ratio of captured tumor cells to the total spiked tumor cells. Purity is defined as the amount ratio of captured tumor cells to the total captured cells including tumor cells and non-specifically captured WBCs [34-35].

To achieve high cell capture efficiency, we used HB structures here to take advantage of the chaotic effect and micro-vortices as illustrated in Figure 2-2(b). To quantify the mixing effect, the integrals of cross-flow in one unit for both grooved-HB chips and wavy-HB chips were calculated following:

$$f_I = \int \sqrt{v^2 + w^2} dV \tag{2-1}$$

where v and w are velocity components in y and z directions, respectively. The comparison results showed that the wavy-HB chip has nearly the same flow mixing performance as that of the grooved-HB chip (see Figure 2-2(c)). In addition to the mixing effect, pattern surface area and cell-surface contact area were considered to predict cell

capture efficiency. Here, cell-surface contact area was calculated for the fractional cell membrane with a separation distance of a ligand-receptor bond length, i.e. 20 nm [72], from the substrate. On substrates of different surface curvatures, cells have different cell-surface contact modes. As sketched in Figure 2-4(a-b), on a grooved-HB pattern, a cell contacts the flat region of the patterned surface vertically, while on a wavy-HB pattern, the cell contacts the surface either on the concave trough or the convex peak. Although Figure 2-4(c) shows that the total pattern surface area of the wavy-HB pattern is slightly less than that of the grooved-HB pattern (6.34x10-8 μm^2 vs. 8.98x10-8 μm^2), the effective cell-surface contact area for the wavy-HB pattern outweighs that for the grooved-HB pattern along the majority surface of one period, as shown in Figure 2-2(f). Both theoretical and numerical investigations suggest a comparable cell capture performance for the wavy-HB chip compared to the grooved-HB chip.

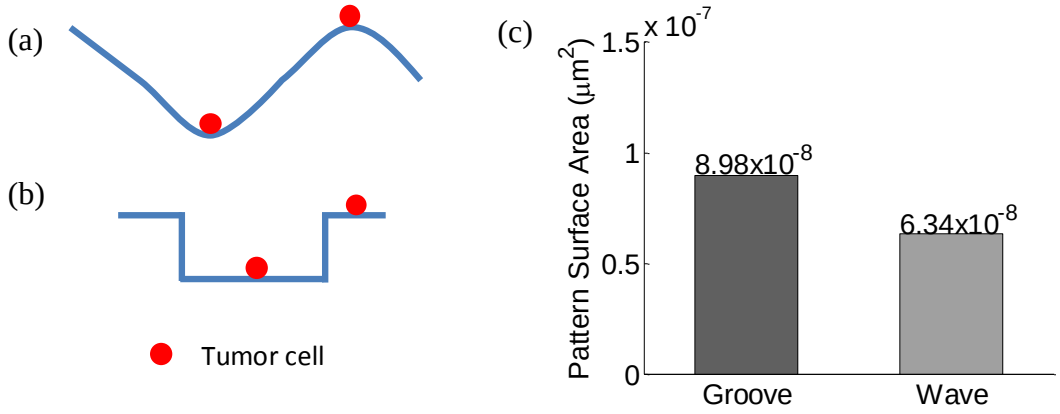

Figure 2-4 Illustrations of cell-surface contact modes on (a) wavy pattern and (b) grooved pattern. Plot is not in scale. (c) Total pattern surface area for one period of groove and wave patterns calculated based on prescribed geometries.

To achieve high cell capture purity, we integrated smooth wavy structures into the wavy-HB chip, as illustrated in Figure 2-2(a, d). The smooth corners in the wavy-HB

chip eliminate regions with ultra-low shear rate presented in the grooved-HB chip, which tend to trap WBCs non-specifically. The shear rate at the wall was derived as follows,

$$\dot{\gamma} = \frac{6Q}{H^2 W} \tag{2-2}$$

where Q is the flow rate, H and W are the height and width of the channel, respectively. The shear rate at a specific location was calculated from the spatial derivation of the local velocity as follow,

$$\dot{\gamma} = \sqrt{\left(\frac{\partial u}{\partial y}\right)^2 + \left(\frac{\partial u}{\partial z}\right)^2 + \left(\frac{\partial v}{\partial x}\right)^2 + \left(\frac{\partial v}{\partial z}\right)^2 + \left(\frac{\partial w}{\partial x}\right)^2 + \left(\frac{\partial w}{\partial y}\right)^2} \tag{2-3}$$

where u, v and w are the component velocities in the x, y and z direction, respectively. As indicated in Figure 2-2(g), under the same inlet flow condition with a shear rate of 60/s, the minimum shear rate in the wavy-HB chip (6.41 /s) is almost 15-fold higher than that in the grooved-HB chip (0.44 /s). It was also noticed that the ultra-low shear rate happens in both bottom left and right corners in the grooved-HB chip. As a result, the wavy-HB chip is expected to have a better performance in purity when compared with the grooved-HB chip.

2.3.2 Wavy-HB Chip Design, Fabrication and Assembly

Figure 2-5(a) shows the reflow fabrication process for making a wavy-HB silicon master. The reproducibility of the fabrication method were validated by measuring the wavy profiles in three fabricated samples. Figure 2-6 indicates that the reflow method is consistent in generating wavy patterns, although further improvement is still needed. The undulation features of the wavy-HB structures were qualitatively observed using optical microscopy in Figure 2-5(b), with detailed dimensions measured in Figure 2-5(c). To

further characterize the wavy structures, a replicated PDMS wavy-HB layer was cut along the wave propagation direction and observed under the microscope. Figure 2-5(d) clearly shows that wavy structures were obtained from the reflow process with a wavelength of 160±2 μm and an amplitude of 22.5±1.5 μm (see Figure 2-5(e)). Figure 2-5(f) shows a typical assembled wavy-HB chip under flow tests. To perform comparison flow tests, geometry equivalent grooved-HB chips were fabricated and assembled following the traditional photolithography method (Images not shown).

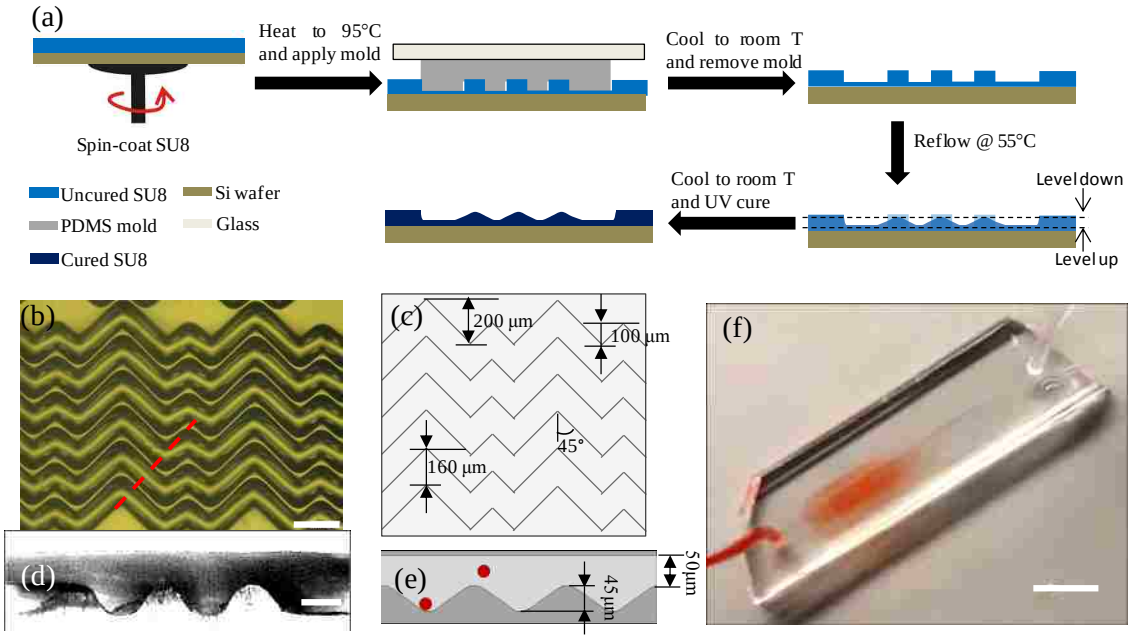

Figure 2-5 Illustration of the wavy-HB chip and its fabrication process. (a) Fabrication process of the wavy-HB master. The "level down" and "level up" are due to the photoresist melting. Micrograph images of (b) top view for the silicon molds (Scale bar, 200 μm) and (d) side view for the assembled chip (Scale bar, 50 μm) illustrate the detail periodic designs and the wavy structures. The assembled chip was cut along the dashed line marked in (b) to obtain the side view. (c) and (e) sketch the layout of the wavy-HB structures with the detailed parameters. The red spheres stand for cells flowing in the channel. (f) Sample injection into a wavy-HB microfluidic device consisting of one inlet and one outlet. (Scale bar, 10 mm)

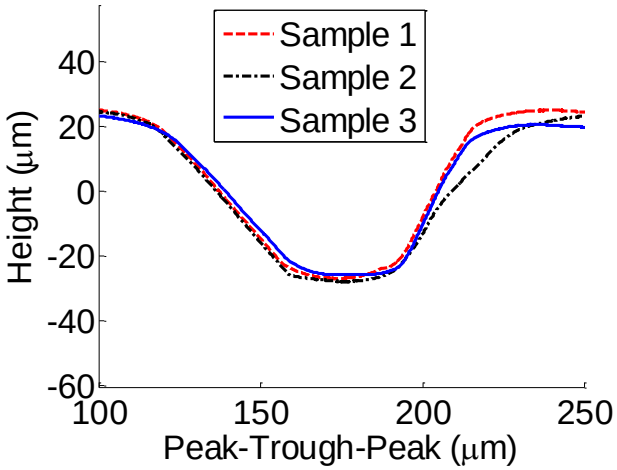

Figure 2-6 Profilometer results of the wavy pattern for three samples made by the reflow approach.

2.3.3 Wavy-HB Performance Validation by Cell Capture Tests

To evaluate the device performance, the distributions of both CTCs and WBCs along the flow direction were investigated first. Shear rate ranging from 60/s to 400/s, which were commonly used in literature [35, 76], was studied here. Captured CTCs and non-specifically bound WBCs in the first 20 sections of each window with a width of 1.14 mm were counted and normalized in percentage, as shown in Figure 2-7(a)-(d). It is found that focusing regions of CTCs tend to move towards the tail sections with increasing shear rate in both grooved-HB and wavy-HB chips (Figure 2-7(a)-(b)). This shift is speculated due to the increased shear force proportional to the increasing shear rate, which agrees well with the results in literature [59]. Interestingly, the wavy-HB chip presents a relatively more uniform distribution with the focusing sections shifted more towards the tail section when compared with the grooved-HB chip. It can be explained by the fact that the smooth wavy patterns lack extremely low shear-rate sections (namely, the sharp trough sections in the grooved-HB chip), allowing for more cells to flow

towards the tail section, which is especially reflected at lower shear rates (60/s and 100/s). WBCs also exhibit a similar trend with the focusing sections shifting towards the tail sections with the increasing shear rate (Figure 2-7(c)-(d)), although the trend is not so significant compared with that for CTCs. This is attributed to the inherent weak non-specific capture force for WBCs, which allows WBCs to have a relatively longer flow pathway. It is also noticed that there are small percentages of peaks in the entry section under lower shear rates (60/s and 100/s), which are probably due to the geometry transition from the flat plane to the patterned regions, namely, wavy or grooved structures.

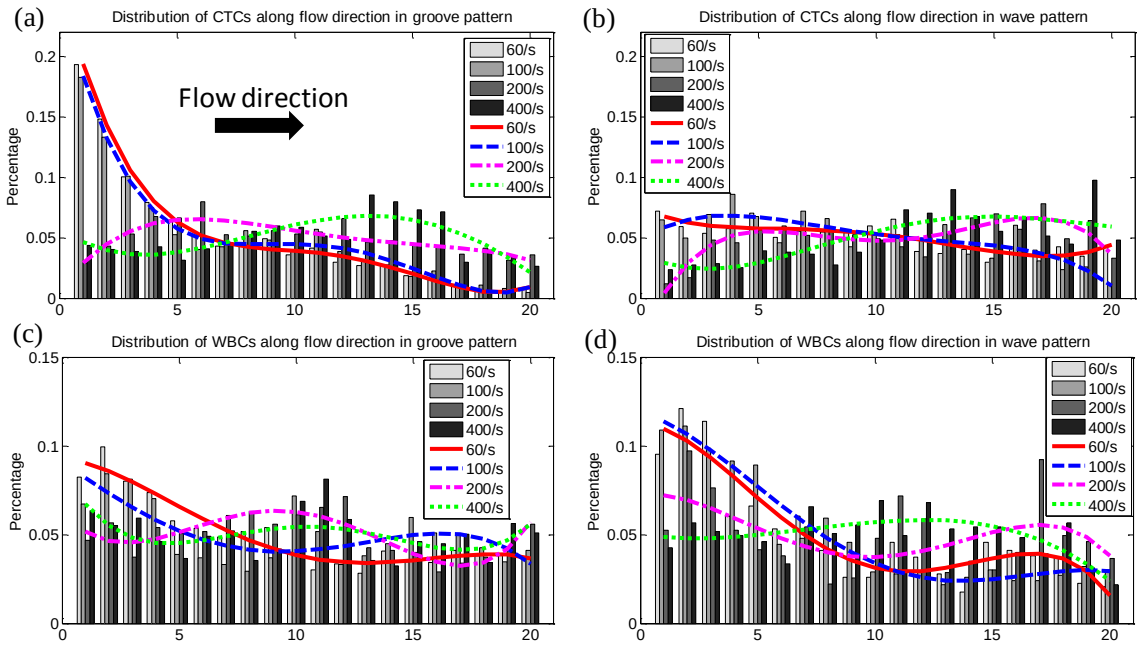

Figure 2-7 Distributions of CTCs along flow direction in (a) grooved patterns and (b) wavy patterns; Distribution of WBCs along flow direction in (c) grooved patterns and (d) wavy patterns. The microfluidic device is equally divided into parallel sections along the flow direction, with the first 20 sections with a width of 1.14 mm shown here. Curve fitting are adopted in each group to indicate the trend of the cell distribution profile.

To demonstrate the performance of the proposed wavy-HB chip, cell tests in both PBS buffer solution and whole blood were performed. To differentiate tumor cells and WBCs, fluorescent images were recorded through the whole chip. As illustrated in Figure 2-8(a)-(c), only cells of celltracker (+) and DAPI (+) were treated as tumor cells, while cells of celltracker (-) and DAPI(+) were treated as WBCs. The overall trend of capture efficiency and purity under different shear rates agrees well with literature results [59]: Figure 2-8(d) shows that capture efficiency decreases with increased shear rate in all cases due to the decreased duration for cell-surface interactions and the increased shear detachment force; Figure 2-8(e) shows that purity increases with increasing shear rate mainly due to the increased shear detachment force to flush away more WBCs (non-specific, weak bonds) than tumor cells (specific, strong bonds). In comparison to the grooved-HB chip, the wavy-HB chip has a similar cell capture performance with a difference smaller than 10.0% in most test conditions, which was already indicated by the similar mixing effects in Figure 2-2(c). On the other hand, the wavy-HB chip performs significantly better than the grooved-HB chip in purity especially in the high shear rates of 200 /s and 400 /s: enhancements of 43.4% (36.7%±2.2% vs. 25.6%±1.7%) and 53.3% (39.4%±4.3% vs. 25.7%±2.1%) are achieved, respectively. In another word, much less WBCs were non-specifically captured in the wavy-HB chip. Under the highest capture efficiency condition (i.e. 60/s) where 1 mL blood test was performed, around 2500 WBCs were captured on the wavy-HB chip in comparison to 4500 WBCs on the grooved-HB chip. These results also agree with the previous finding that HB pattern overweighs the micropost-based CTC-Chip (around 5000 WBCs) in terms of the purity [34-35]. By

introducing asymmetrical structures, Sheng *et al.* [55] improved the purity but the amount of non-specific WBC was still around 3500.

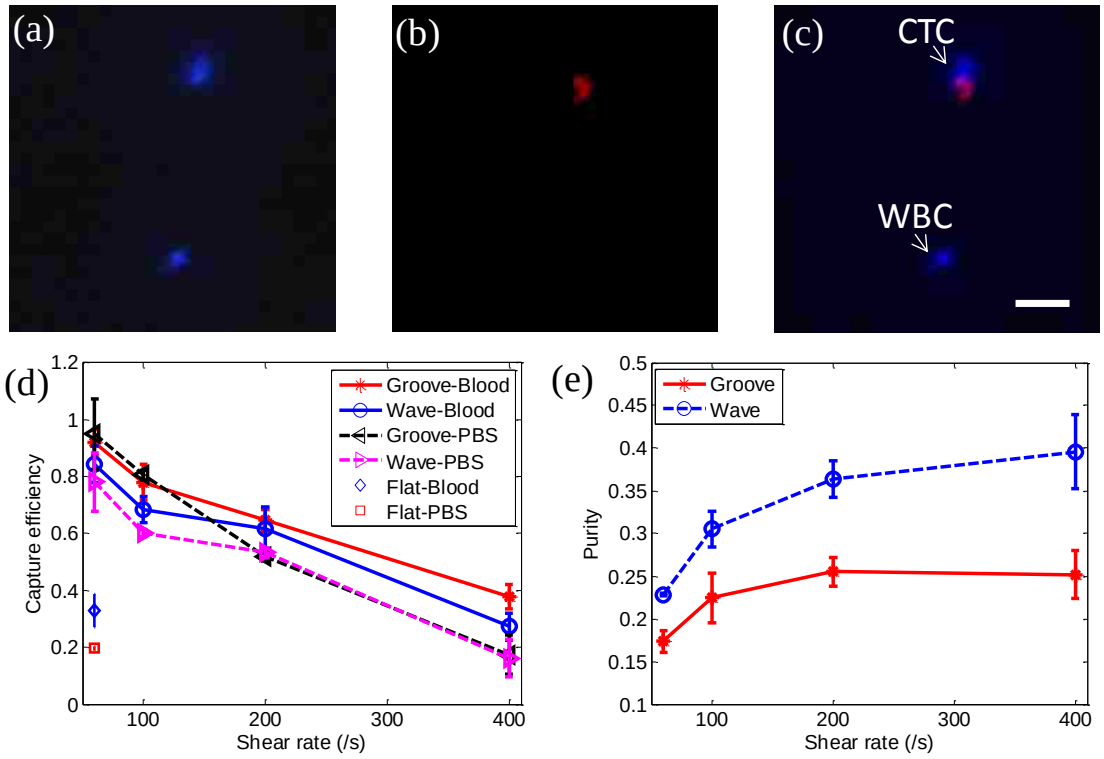

Figure 2-8 Tumor cells capture in the wavy-HB and grooved-HB chips (a)-(c) Cell-tracker and DAPI fluorescent differentiation of tumor cells and WBCs. Both tumor cells and WBCs are DAPI positive in (a), while only pre-labeled CTCs are cell-tracker positive in (b). The merged image in (c) shows only cells which are DAPI (+) and cell-tracker (+) are regarded as tumor cells, while cells which are DAPI (+) and cell-tracker (-) are regarded as WBCs. (Scale bar, 80 μm) (d) Capture efficiency *vs.* shear rate in the grooved-HB chip, the wavy-HB chip, and the flat device. (e) Purity *vs.* shear rate in both chips. Error bars stand for standard deviations in three independent experimental trials.

Notably, higher tumor cell capture efficiency was achieved in blood cases compared to PBS cases in both wavy-HB chips and flat devices, as shown in Figure 2-8(d). Taking the shear rate of 60/s as an example, an enhancement of 8.83% was obtained in the wavy-HB chip (85.0%±6.8% vs. 78.1%±10.1%). Furthermore, an enhancement up to 67.4% was obtained in the control flat channel (32.8%±5.8% vs. 19.6%±0.9%). We hypothesize that

the enhancement comes from the margination effect of tumor cells towards the channel surface. It has been suggested that more deformable red blood cells would migrate towards the channel center while the stiffer tumor cells are repelled towards the channel surface [77]. By comparing the enhancement level for the wavy-HB chip and the flat device, it was also suggested that the margination effect induced by blood contributes more in the flat channel. The margination effect in the wavy-HB chip might be disturbed and thus reduced by the micro-vortexes. Interestingly, although similar enhancement attributed to blood was not observed in the grooved-HB chip at 60/s (92.1%±4.6% *vs.* 95.0%±12.4%), an enhancement up to 123.5% was obtained at high shear rates, i.e., 200/s and 400/s. This suggests that the existence of normal cells contributes more to efficient tumor cell capture at high shear rate, although the mechanism is not clear yet.

The viability of tumor cells under different shear rates was also studied by performing the LIVE/DEAD assay in both grooved-HB and wavy-HB chips, using the flat channel as a control. Figure 2-9(a)-(d) show typical micrographs of LIVE/DEAD assay results under 60/s and 400/s for both chips. Cell viability was then calculated by counting the amount of live cells and dead cells in these fluorescent images. As illustrated in Figure 2-9 (f), the viability decreases with increased shear rate, indicating that captured tumor cells are prone to lose their function under high shear rate. The comparison reveals that the wavy-HB chip offers a higher cell viability than the grooved-HB chip, suggesting that the captured tumor cells are more physically intact in the wavy-HB chips. Especially under the high shear rate of 400/s, the cell viability enhancement in the wavy-HB chip is more significant over the grooved-HB chip with an 11%

improvement (89.29%±4.91% vs. 80.65%±2.64%). It is speculated that more cell deaths are attributed to damages induced by sharp corners in the grooved-HB chip.

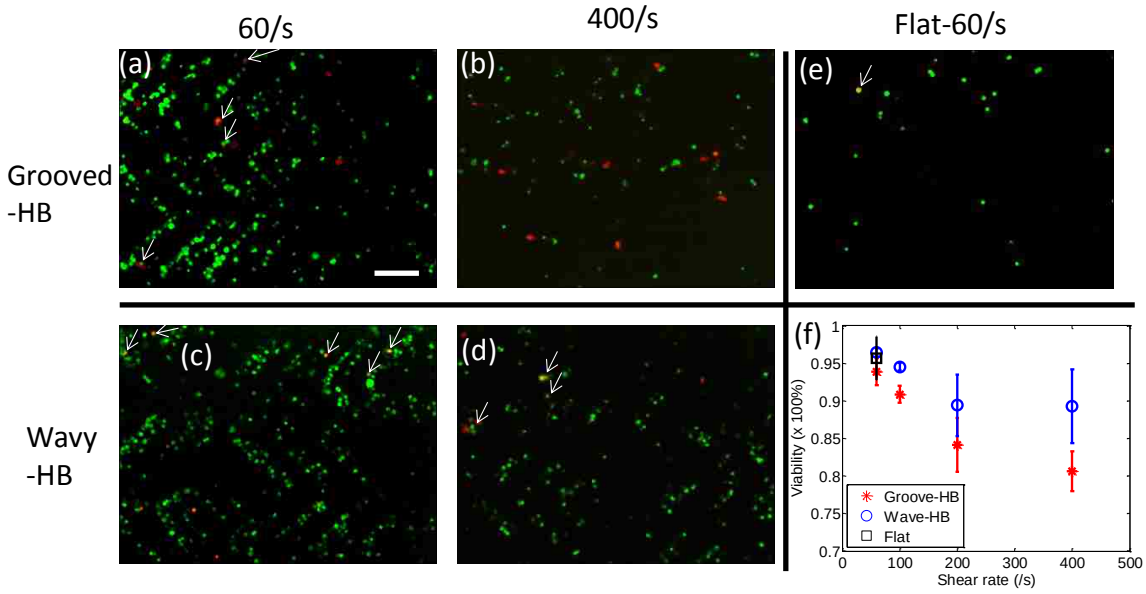

Figure 2-9 Viability of captured tumor cells in the wavy-HB and grooved-HB chips. Representative fluorescent micrographs of the captured tumor cells in the grooved-HB chip after LIVE/DEAD a under the shear rate of (a) 60/s and (b) 400/s. LIVE/DEAD stain results in the wavy-HB chip under the shear rate of (c) 60/s and (d) 400/s, respectively. (e) LIVE/DEAD stain results in the flat channel under the shear rate of 60/s. Cells which are calcein-AM (+) and EthD1 (+) are treated as dead, as indicated by white arrows in (a)-(e). (f) Quantitative analysis of viability of captured tumor cells in the wavy-HB and grooved-HB chips under different shear rates. Error bars stand for standard deviations in three independent experimental trials. (Scale bar, 160 μm)

In addition, the clinical utility of the wavy-HB chip was also validated by the isolation of tumor cells in PBS buffer solution at concentrations of 10, 100, 500 and 1000 cells/mL. The test shear rate was 60/s for all cases, where capture efficiencies of around 80% were achieved, as shown in Figure 2-10. The linear regression study results show that the device has a consistent performance under the test conditions with different spiked tumor cell amounts. This suggests that the wavy-HB chip has the potential to fulfill the clinical requirement to detect very rare CTCs, i.e., 1-10 cells/mL blood.

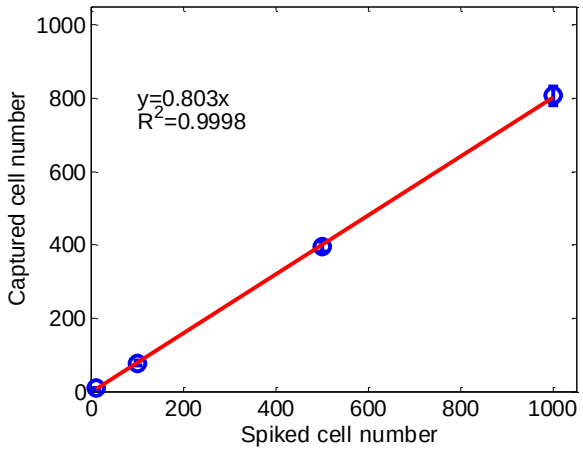

Figure 2-10 Linear regression analysis of the captured cell amount versus spiked cell amount. HCT-116 cells at various concentrations were spiked in PBS buffer solution and captured cell amount were then counted. Error bars stand for standard deviations in three independent experimental trials.

2.3.4 Cell Distribution along One Pattern Period and Its Indication for Device Performance

Distribution of tumor cells and WBCs along a single pattern period was then studied. Representative fluorescent optical micrographs of tumor cell distributions in the grooved-HB chip and wavy-HB chip are shown in Figure 2-11(a) and (b), respectively. A period is defined as the region between two consecutive troughs which is equally distributed into 20 sections following the flow direction, as illustrated in Figure 2-11(c)-(f). For tumor cell distributions under increased shear rate, grooved-HB patterns have a focusing region in the trough close to the upstream groove sidewall, with the section shifting more towards the groove side wall. On the other hand, wavy-HB patterns have a relatively focusing region shifting from the lower upstream slope to higher upstream slope, as shown in Figure 2-11(c)-(d). For WBC distributions under increasing shear rate, grooved-HB patterns have focusing regions in both upstream and downstream trough

regions with the section shifting more towards the downstream trough section, while wavy-HB patterns have focusing sections shifting from trough sections to the regions close to the peak, as shown in Figure 2-11(e)-(f). Notably, the WBC distributions under increasing shear rate exhibit a dramatic difference in these two chips: WBCs tend to be trapped in the trough sections close to the downstream side wall for the grooved-HB chip, especially under larger shear rates (200/s and 400/s) as shown in Figure 2-11(e), while for the wavy-HB chip, WBCs shift from the trough to the regions close to the peak where shear detachment force is large and WBCs detachment is easy to happen as shown in Figure 2-11(f). This trend difference is probably attributed to the geometry difference: the sharp grooved structure resists WBCs from rolling upwards to the ridge while the smooth wavy structure allows WBCs to roll towards to the peak region. Following this reasoning, under larger shear rates, more WBCs in the wavy-HB chip are prone to be pushed from the trough to the peak, where the shear detachment force is relatively larger as shown in Figure 2-2(d). As a result, the wavy-HB chip is subjective to a high purity under larger shear rate, which agrees with the experimental data in Figure 2-8(e).

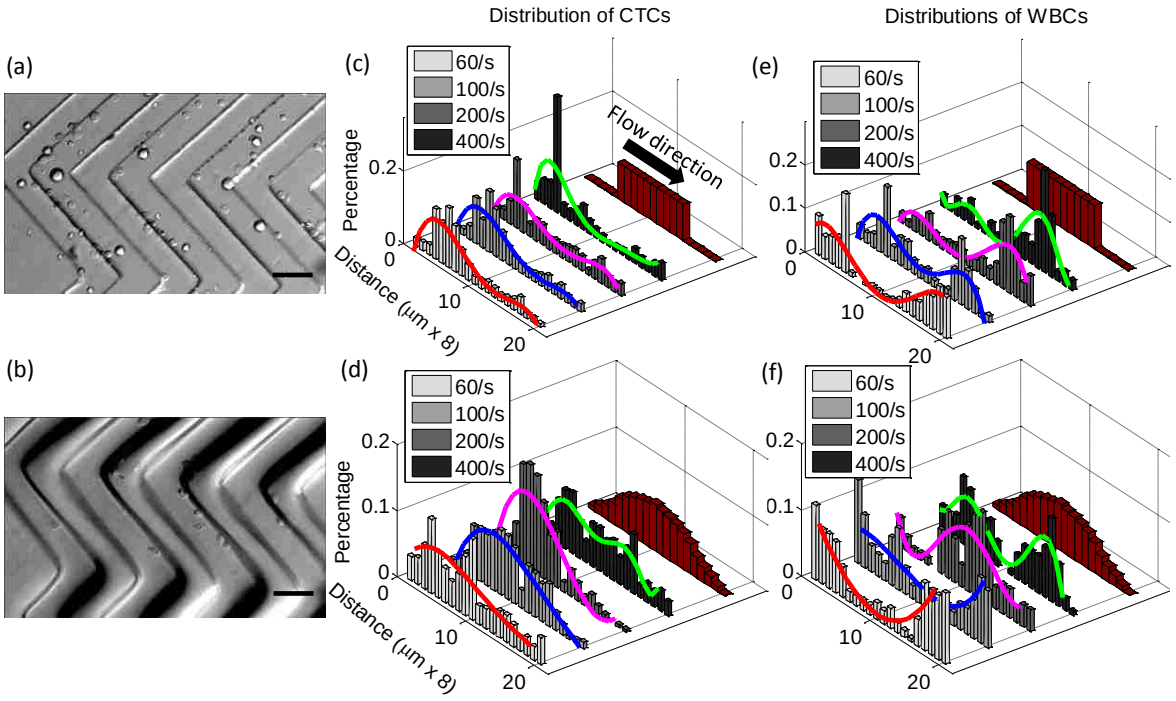

Figure 2-11 Illustrative micrograph images of tumor cells distributions in (a) a grooved-HB chip and (b) a wavy-HB chip. (Scale bar, 80 μm) Quantitative distributions of tumor cells along one pattern period in (c) the grooved-HB chip and (d) the wavy-HB chip. Distribution of WBCs along one pattern period in (e) the grooved-HB chip and (f) the wavy-HB chip. One pattern period is defined as trough-peak-trough indicated as the dotted line in (a) and (b). A pattern period is equally divided into 20 sections along the flow direction with a width of 8 μm. Schematic images of the divided patterns are also shown in (c)-(f). Curve fits are used to indicate the cell distribution patterns.

2.4 Discussion

The distribution profiles of tumor cells and WBCs shown in Figure 2-11 are explained by a two-regime based mechanism, i.e. adhesion-detachment force balance and cell-surface contact frequency. In other words, the peak capture regions are always where there are more cell-surface contacts with the pre-requisite of the adhesion force large enough to resist the shear detachment force. In the grooved-HB patterns, two factors contribute to the cell distribution: (1) large cell-surface contact frequency exists in both groove sides and the ridges, as shown in Figure 2-12(c); (2) cells experience larger shear

detachment forces in the ridges and smaller ones in the troughs, as indicated in Figure 2-2(d)-(e) and Figure 2-2(g). As a result, both tumor cells and WBCs tend to be collected in the trough sections close to the groove sides, as indicated in Figure 2-11(c) and Figure 2-11(e). Moreover, with increasing shear rate, tumor cells tend to be focused close to the upstream sidewalls while WBCs are close to the downstream sidewalls, which is reasoned due to the difference in adhesion force. The weaker non-specific adhesion force for WBCs yields a shift of focusing regions towards the smaller shear rate sites, namely, the troughs close to the downstream sidewalls. Similarly, in the wavy patterns, with relatively strong adhesion forces due to the larger cell-surface contact areas, tumor cells tend to be collected in the higher upstream sections, which have higher cell-surface contact frequency (Figure 2-12(c)). With the increasing shear rate, the slight shift towards the higher downstream sections is due to the increasing detachment force that makes cell distribution more uniform. On the other hand, WBCs are speculated to readily shift along the wave due to weak adhesion forces. At lower shear rates (60/s and 100/s), WBCs are easily removed in the regions with higher shear rate, i.e. ridge, thus they tend to be collected at the troughs where the shear rate is low (see Figure 2-2(d)). With shear rate continuously increasing to higher values (200/s and 400/s), non-specifically captured WBCs are pushed back and forth along the wave and their distributions shift as indicated in Figure 2-11(f). The detail non-specific adhesion mechanism for WBCs on anti-EpCAM coated surface is not clear so far.

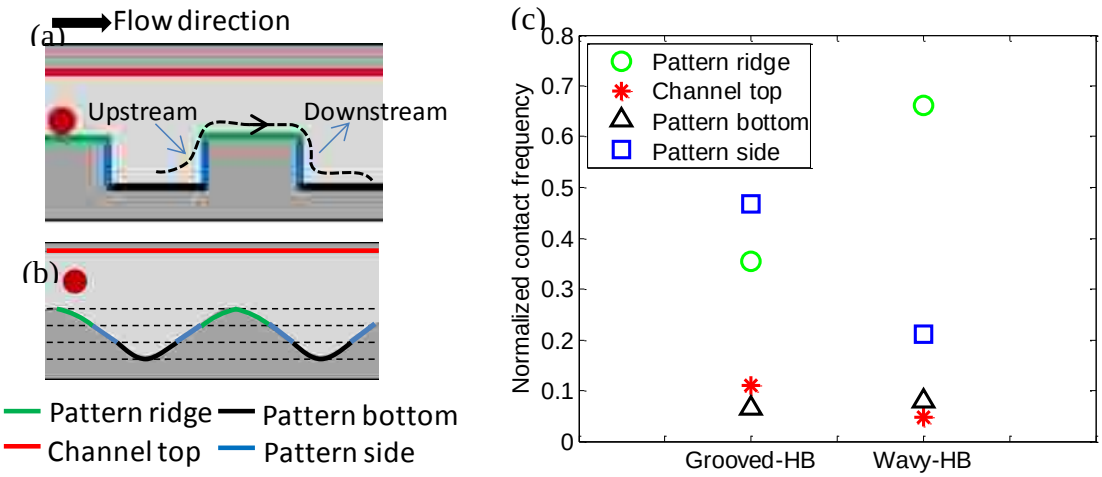

Figure 2-12 Numerical simulation reveals cell-surface contact frequency in the grooved-HB chip and the wavy-HB chip. The locations for cell-surface interactions, including the pattern ridge (green), channel top (red), pattern bottom (black) and pattern side (blue) in (a) the grooved-HB chip and (b) the wavy-HB chip. The upstream and downstream along one streamline is illustrated in (a). (c) Normalized cell-surface contact frequency in different locations for both chips.

The tumor cell capture experimental results are in good agreement with the computational prediction. On one hand, the overall tumor cell capture efficiency is well predicted by the integral of cross flow, which indicates similar mixing effects between grooved-HB and wavy-HB chips. The slight difference of capture efficiency might be attributed to the decreased surface area during the reflow process, where the surface areas of a single pattern period for the grooved-HB and wavy-HB pattern are 8.98×10-8 m^2 and 6.34×10-8 m^2, respectively (see Figure 2-4(c)). It should be noted that local distribution does not necessarily offer the overall picture of the tumor cell capture efficiency. As shown in Figure 2-7, although a larger portion of tumor cells are trapped in the head sections of the grooved-HB chip, the distribution decreases very fast along the flow direction. On the contrary, the wavy-HB chip shows a relatively uniform distribution along the whole flow direction. To evaluate cell capture efficiency, accumulation of

captured cell across the whole chip should be considered. On the other hand, the computational results are used to explain the local distribution of tumor cells. For example, compared to the wavy-HB chip, the trough section for the grooved-HB chip has lower shear rate (see Figure 2-2(d-e)) but shows similar cell surface contact frequency (see Figure 2-12(c)). As a result, a larger proportion of captured tumor cells are present in the trough section for the grooved-HB chip in comparison with the wavy-HB chip as shown in Figure 2-11(c-d). Meanwhile, the lower shear rate in the trough region also brought more WBCs to be non-specifically captured, which was confirmed by the WBC local distributions as shown in Figure 2-11(e-f).

In literature, there have been a few attempts to develop tumor cell isolation chips derivative from the grooved-HB patterns [59, 78-79], but all with sharp corners. Our theoretical and computational analyses reveal the fundamental limitation of the sharp grooved patterns, i.e., ultra-low shear rate regions close to the groove corners (see Figure 2-2(g)) thus increasing the chance of non-specific cell capturing. By introducing the smooth wavy-HB structures in the current configuration, ultra-low shear rate regions are eliminated as shown in Figure 2-2(g). Our results have demonstrated an enhanced purity by 43.4% compared to that from the grooved-HB structures, which is crucial for down-stream analysis like high quality cell profiling and thorough genomic analysis [80-81]. For example, it is an essential need to achieve high purity for DNA microarray analysis [82]. Enhanced purity obtained in our wavy-HB chip can reduce the influence introduced by impure WBCs, leading to a more reliable gene data analysis. Further enhancement can be achieved by introducing asymmetry between the trough and ridge sections of the wave, as WBCs are easily trapped in the trough as shown in Figure 2-11(e-f), which is also

suggested by other work [55]. More importantly, the proposed idea to smooth sharp grooves can be adopted as a general strategy in other existing devices to improve the purity while preserve capture efficiency.

Challenges still exist on the anti-EpCAM based approach for CTC isolation. First, CTCs present heterogeneous phenotypes for different cancer types [83] and EpCAM expression levels could also be down-regulated over the course of metastasis and dissemination [84]. Thus, the capture yield may drop for CTC subpopulations of non-epithelial and EpCAM down-regulated phenotypes. A potential strategy to tackle this challenge is to vary the antibody type in the wavy-HB chip [85]. It was also demonstrated that higher antibody coating density can enhance CTC isolation34, which can reduce the loss of EpCAM down-regulated CTCs. Another challenge for the current approach lies in how to effectively release captured CTCs. Xu *et al.* [86] tried to directly detach the captured CTCs by flushing air while the release efficiency was only 45% partially due to the dead volume in the sharp groove. This can be significantly improved in our smooth wavy pattern by eliminating the sharp groove regions where cells are readily trapped. To further overcome this problem, we can replace anti-EpCAM by other environment stimulated substances, like aptamers [87] and polymer materials [88]. We believe the combined high efficiency and high purity in our wavy-HB chip together with the modified surface coating will allow for further enhancement of CTC capture and post-analysis for various applications.

2.5 Conclusion

In summary, a wavy-HB chip coated with anti-EpCAM has been demonstrated with high efficiency and purity in isolation of tumor cells from the spiked whole blood.

Due to the staggered HB structures adopted from the hallmark grooved-HB chip, high capture efficiency up to 85.0% is achieved by the induced passive mixing. In comparison with the grooved-HB chip with sharp corners, the wavy-HB chip has the smooth wavy patterns, leading to nearly two-fold enhanced cell capture purity up to 39.4%. The enhancement is mainly due to the lack of the ultra-low shear rate regions in the grooved-HB chip. In addition, the wavy-HB chip serves as a better tumor cell isolation platform in that its inherent gentle nature induced by the smooth undulations (maximum shear rate is 645.9 /s compared to 1084.1 /s in the grooved-HB chip in the shear rate of 400 /s) protects cells from deformation forces and keeps cells intact. Despite the promising results achieved in the wavy-HB chip, it is noticed that the trade-off between capture efficiency and purity still exists. It has been suggested that integration of nanostructures could potentially address this issue [54, 89-90], which will be implemented into our wavy-HB chip in the future. Further, patient blood samples will be tested on the wavy-HB chip to validate its clinical utility.

Chapter 3: Geometry Optimization for Grooved-HB Chip

3.1 Introduction

Using of microfluidic chips for capturing circulating tumor cells (CTCs) has raised lots of interests recently and various microfluidic platforms have been developed with demonstrated clinical utilities [91-94]. One main criteria to evaluate the device performance is to achieve high CTC capture efficiency, which is defined as the ratio of amount of captured CTCs and the total number of CTCs. Among those methods developed in literature, immnuoaffinity based approach has been widely adopted to achieve this goal. This is attributed to the fact that most CTCs are cells of epithelial origin and uniquely over-expressed epithelial cell adhesion molecules (EpCAM), which other normal cells do not express. Due to the laminar nature of flow in a typical microfluidic device, interactions between cells and the microfluidic wall are not readily accessible which is essential for cell capture. Therefore, the main challenge for achieving the goal of high CTC capture efficiency lies in how to effectively bring CTCs close enough to anti-EpCAM coated surfaces to form ligand-receptor capture bonds.

In recent years, integrations of various complex geometry patterns into microfluidic chips have been proposed to increase CTC interactions with anti-EpCAM coated surfaces. Nagrath *et al.* [34] reported a microfluidic chip with an array of microposts, which precisely controls the flow path to enhance the CTC-pillar interactions. The inherent laminar flow property limits its capture efficiency to 65% in the flow rate of

1.1 ml/hr. To overcome this limitation, approaches to disturb the laminar pattern attracts lots of attention from researchers. Stroock *et al.* [56] firstly reported a staggered herringbone structure to generate passive chaotic mixing. Integration of this structure into microfluidic chips was then widely adopted for CTC capture with significantly increased capture efficiency [35, 78, 87]. The NanoVelcro CTC chip developed in Tseng's group [59, 95] consisted of both herringbone PDMS structures and nanopillars, which achieved a capture efficiency up to 95%. By tuning the pillar size and spacing, maximized CTC capture occurred when the pillars had an estimated diameter of 120 nm and spacing of 140-200 nm [68].

The key mixing mechanism in the herringbone structure lies in the transverse flow patterns which stretch and fold the fluid volumes, thus allowing a short distance for fully mixing. Numerous studies have also been performed to quantitatively investigate the herringbone geometry effect on the flow mixing. Stroock *et al.* [56] evaluated the mixing performance of different HB devices by measuring the mixing length from confocal microscopy imaging. However, its complexity in device fabrication and repetitive flow tests limits its applications to a certain extent. Instead, owing to its inherent easy access, computational fluid dynamics (CFD) methods have been extensively applied on studies of geometric optimization studies. Various characterization methods have been adopted to evaluate the mixing effect including maximum striation thickness measurement [73, 96] residence time analyses [97-98] and Poincare maps analysis [99]. A general criterion for the optimized mixing effect of a HB device has been concluded by Lynn [74]. That is: (1) the HB structure has an optimized width fraction of the short arm of 1/3 and an optimized

oblique angle of 45°; (2) The mixing effect strongly relies on the groove depth ratio while weakly depends on the channel aspect ratio.

However, although the herringbone structure is widely used to enhance the flow mixing, concerns regarding these adopted geometry guides for enhancing CTC capture still hold, in that enhanced internal flow mixing does not necessarily lead to an increase of CTC-surface interactions. Flow mixing happens in the whole cross-section indicating the strength of the inter-diffusion, thus it does not fully correlate to the ability to push CTCs towards the anti-EpCAM coated surface. From this perspective, a model to consider the cell-surface interactions is needed. Forbes *et al.* [58] pioneered the study to research on the particle-surface interactions in a herringbone micromixer. When it comes to the specific field of CTC capture study, the limitation lies in the fact that it does not directly correlate to the capture efficiency with geometry parameters, nor does it consider the cell adhesion probability which exists in CTC capture studies [76, 100-101]. As such, a more comprehensive model considering the adhesion probability is in need for optimizing the herringbone geometries for enhanced CTC capture.

In what follows, the computational model with adhesion probability is firstly introduced. Then the model is validated through an experimental comparison in terms of both capture efficiency and cell capture distribution. A systematic study is lastly pursued to investigate the geometrical effects of various parameters of herringbone structures on CTC capture. The conclusion obtained from this work can provide as a geometry guide for researchers to optimize and design their devices accordingly, rather than running repetitive experimental tests in devices with a huge matrix of different geometries.

3.2 Numerical Methods

In this study, we developed an in-house code integrated with finite element method (FEM) based flow simulation to study the cell transport and capture dynamics. This numerical approach was carried out in three steps. First, FEM simulations of the flow domain were performed to obtain flow velocities, pressure and other derivatives using the fluid dynamics module in COMSOL, a widely used software in computational fluid dynamics (CFD) [71, 102-103]. Then cells were simulated to transport in the flow domain following the governing equation. Under prescribed criterions regarding cell-surface interactions, flowing cells were determined to be captured or not.

3.2.1 Flow domain simulation

For a microdevice of herringbone structures, the geometry was designed following the outline proposed by Stroock *et al.* [56], where repetitive herringbone grooves were staggered to induce chaotic effects. To simplify the simulation, only one unit of herringbone grooves was considered, as shown in Figure 3-1. The unit consists of a flow channel and two half cycles of herringbone grooves. In this study, various parameters were investigated including the number of grooves for one half cycle (n), intersection angle between two grooves (θ), channel height (h), groove depth (d), channel width (w), the percentage (p) of a groove width (w_g) out of a groove pith (w_p), asymmetric factor (β) defined as the fraction of the narrow arm in a channel width. After the model was built with the prescribed geometrical parameters, tetrahedral elements were applied for meshing the model with a minimum element quality of 0.047. A grid convergence study was performed to investigate the mesh quality. Mesh refinements

ended until difference smaller than 2% was achieved for both flow velocities and pressures between two simulations.

In the fluid domain, alginated phosphate buffered saline (PBS) solution with a density of 1.007×10^3 kg/m^3 and a viscosity of 3.3×10^{-3} Pa·s was used as the medium [70]. The boundary conditions were set as follows: a parabolic flow profile was assigned to the inlet where it was assumed that the flow field was fully developed; a gauge pressure of 0 was assigned to the outlet; side walls were set as periodic boundary which mimics the real application where there are many parallel units; all other surfaces were set as wall where the velocity was equal to 0. The flow domain was then simulated by solving the incompressible Navier-Stokes equation below:

$$\rho\vec{U} \cdot \nabla\vec{U} = -\nabla P + \mu\nabla^2\vec{U} \tag{3-1}$$

where U is the flow velocity, P is the pressure, ρ and μ are the density and viscosity of fluid medium, respectively.

3.2.2 Cell Transport Dynamics

In-house developed codes were used to simulate the cell transport in a microfluidic device. To simplify the simulation, cells were treated as dots with a virtual radius of 10 μm and a density of 1.06×10^3 kg/m^3. Fluid-cell interaction and cell-cell interaction were neglected in this model. These simplifications were also adopted in other studies in literature [58]. More comprehensive studies taking these factors into account could be found elsewhere [104-105], while it was too computationally expensive and time consuming for a geometrical study.

To simulate cell transport dynamics, a dose of cell-mimicked particles with a constant supply of 1000 particles per 0.1 s were periodically injected through the inlet, which mimics a continuous cell injection. The flowing cells transported in the microfluidic chip following the governing equation as shown below,

$$m\dot{\boldsymbol{v}} = \boldsymbol{F}_{adv} + \boldsymbol{F}_{sed} + \boldsymbol{F}_{diff} + \boldsymbol{F}_{shear} \tag{3-2}$$

where m and $\boldsymbol{v}$ are the mass and velocity of a single cell, respectively. $\boldsymbol{F}_{adv}$, $\boldsymbol{F}_{sed}$, $\boldsymbol{F}_{diff}$ and $\boldsymbol{F}_{shear}$ are the force induced by advection flow, cell sedimentation resulted from cell weight and fluid floating, Brownian Motion induced diffusion and shear induced migration, respectively. Here, a time-scale analysis was performed to evaluate the dominance of each force [58]. Given the geometry used in Stroock's work [56], the time scale induced by diffusion was $t_{diff} = D_h^2 / D$ which equals to 1.51×10^6 s; the one by shear induced migration was $t_{shear} = D_h^2 / \dot{\gamma} R_p^2 D_\varphi$ which equals to 1.96×10^8 s; the one by sedimentation was $t_{sed} = 9D_h\eta / 2\Delta\rho g R_p^2$ which equals to 28.3s; the one by advection was $t_{adv} = D_h / U$ which equals to 0.08s, where $D_h = 4A/P$ (A is the channel cross-section area and P the perimeter), D is the diffusivity of the particle. It was noticed that t_{diff} and t_{shear} were several orders of magnitude larger than t_{adv} and t_{sed}. In other words, the cell transport in the microfluidic chip was dominated by advection force and sedimentation force, while the Brownian motion induced diffusion force and the shear induced

migration force were neglected. Thus, the governing equation was simplified to the format described as follows:

$$m\dot{\boldsymbol{v}} = \boldsymbol{F}_{adv} + \boldsymbol{F}_{sed} \tag{3-3}$$

3.2.3 Cell Capture and Adhesion Probability Integration

Flowing cells were treated to contact with the capture bed when the cell-surface distance was smaller than the radius of a cell, i.e., 10 μm. With the fact that the cell-surface interaction is a dynamic process which involves the continuous breakage/formation of ligand-receptor bonds, adhesion probability was introduced to reflect this overall performance and determine whether a cell was firmly captured, which was formulated as below [62]:

$$P = m_r m_l K_a^o A_c \exp\left(-\frac{\lambda}{K_B T}\frac{F_{\text{dislodge}}}{m_r A_c}\right) \tag{3-4}$$

where m_r and m_l are the receptor density and ligand density, respectively, K_a^o is the receptor–ligand association constant at zero load, A_c the contact area, λ the bond length, $K_B T$ the thermal energy and F_{dislodge} the dislodging force. Several studies in literature have also adopted the adhesion probability to study the CTC capture in various microfluidic devices [100, 106]. However, for a specific biological problem like CTC capture in this study, hurdles usually existed due to the lack of information about m_r, m_l, K_a^o and λ. A few attempts have been made to overcome this problem. Notably, Smith [100] firstly introduced two lumped parameters A and B to simplify the formula into the format as shown below:

$$P = A\exp\left(-B\tau\right) \tag{3-5}$$

where $A = m_r m_l K_a^o A_c$ and $B = -\frac{\lambda}{K_B T}\frac{k}{m_r A_c}$. Meanwhile, it was assumed that the dislodging force was proportional to the shear stress. With this simplified lumped model, the unknown reduced to only A and B, compared to five parameters in eqn. (3-4).

In equation (2), *A* described the probability when the shear rate was zero and *B* denotes the trend of adhesion probability under different shear stress. By taking advantage of these properties, we calculated *A* and *B* based on two experiments. To determine *B*, a Hele-Shaw design was created where the shear stress linearly decrease in the flow direction [107]. Cell capture test was then performed to study the cell distribution along the flow direction. Here, a high concentration of 10^6/mL was applied so that the assumption held that a constant concentration was over through the whole device. As a result, the adhesion probability was directly proportional to the amount of captured cells at each shear stress. A curve fit of the adhesion probability vs. shear stress was then performed to obtain *B*. To determine *A*, a cell capture test was performed in a herringbone microfluidic device under a prescribed shear rate. By iterating *A*, a best match could be found between the experimental result and the computational result. Thus, the integrated model with adhesion probability was established and ready for following geometrical studies.

3.3 Experiments

3.3.1 Microfluidic Chip Design and Fabrication

To experimentally obtain *A* and *B*, both Hele-Shaw design and herringbone design were drafted by AutoCAD software. Specifically, the Hele-Shaw design had an inlet width of 5 mm and channel height of 100 μm, while the geometry profile of two side walls were defined to achieve a linearly decreased shear stress along the flow direction: $y = \frac{125}{50 - x}$ (mm) . The herringbone structure was designed to follow the geometry in Stroock's work [35]. These designs were then sent out to CAD Inc. for photomasks. Standard photolithography method was used to fabricate the SU8 master mold, followed by a silane treatment to make the surface hydrophobic which allows for an easy peeling of PDMS.

3.3.2 Surface Functionalization

To capture rare tumor cells, antibodies against epithelial adhesion molecules (anti-EpCAMs) were coated on the channel surface which allow for bond formations uniquely with tumor cells. This was achieved following a standard surface functionalization process [35]. Briefly, PDMS slabs were plasma treated and assembled into a microfluidic device, immediately followed by an incubation of 5% (v/v) 3-mercaptopropyl trimethoxysilane (MPTS) in ethanol for 30 min. at room temperature (RT). The device was then incubated with 0.01 mM N-y-maleimidobutyryloxysuccinimide ester (GMBS) in ethanol for 30 mins and another overnight incubation of 10 μg/mL NeutrAvidin in PBS at 4 °C. Before the test, biotinylated goat anti-human EpCAM in 1% (w/v) bovine serum albumin (BSA) in PBS

solution was added to the device and incubated for 2 hrs at RT, followed by an incubation of 3% BSA solution containing 0.05% Tween20 for 30 min to reduce non-specific cell capture. PBS or ethanol solution was used to remove the excessive solution from the previous injection. To make each functionalization consistent, a syringe pump (Harvard Apparatus) was used for each injection at a flow rate of 3.5 mL/hr.

3.3.3 Cell Culture

HCT-116 cells was used as a model cancer cell line in this study as colorectal cancer is among the most common cancers [108]. Cell culture medium comprised of Dulbecco's Modified Eagle's Medium (Sigma Aldrich), 10% fetal bovine serum (Invitrogen) and 1% penicillin/streptomycin (Sigma Aldrich) was renewed every 2-3 days. 0.05% Trypsin–0.53 mM EDTA was used to detach cells upon 80-90% confluency.

3.3.4 Cell Capture Test

Before cell capture test, detached cells were counted by hemocytometer and diluted in alginated PBS solution. For each cell experiment, a syringe pump was used to inject the cell solution at a prescribed flow rate. 1 mL PBS solution was then injected to remove all suspended cells at a flow rate of 3.5 mL/h. For long-term imaging, all captured cells were fixed by 4% paraformaldehyde for 15 mins at RT and then kept at 4 °C. All microfluidic devices were then imaged by a regular microscope to count captured cells.

3.4 Results and Discussion

3.4.1 Numerical Model

Figure 3-1(a) shows a COMSOL simulation results for a typical herringbone microfluidic chip. The flow streams were disturbed by the asymmetric grooves, which is essential for cell-surface interactions and further cell capture. More clearly illustrated in Figure 3-1(b), the vortex effect in the cross-section was critical to shift flowing cells towards the antibody coated capture bed. This chaotic effect was also widely demonstrated experimentally and numerically by studying the mixing of fluorescent and clear solutions [56, 109]. Figure 3-1(c) outlined all geometric parameters in a herringbone unit. To perform a comprehensive geometric study, each parameter was carefully considered within a specified range. The basic criterion for selecting values for a parameter was to cover as many possibilities as possible and refer to the trend of the numerical results. More details can be referred to the section of *Geometric Optimization*. Figure 3-1(d) describes a scenario where a flowing cell contacts the capture bed. Based on the adhesion probability, cells were determined either to keep firmly captured or detach. Specifically, a random between 0 and 1 was generated upon a cell contacted the capture bed. Meanwhile, the adhesion probability P for the cell was also calculated following eqn. (3-5). If P was larger than the random number, the cell was treated to be firmly captured. Otherwise, the cell was treated to be transiently tethered and continued to flow following the governing equation.

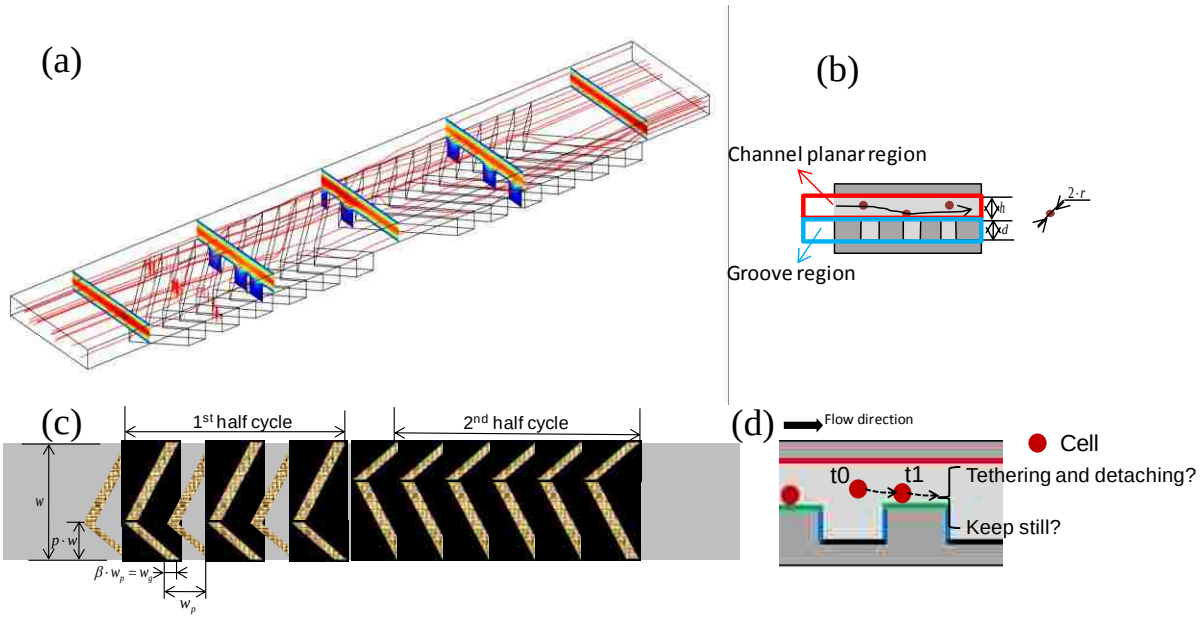

Figure 3-1 (a) Typical flow domain of one unit in a herringbone microfluidic chip simulated by COMSOL. (b) The chaotic flow pattern for enhanced cell-surface interactions in a cross-section. Schematic diagrams of a herringbone unit with all annotated geometrical parameters from (c) top view and (d) side view. A scenario of flowing cell to be firmly captured or not determined by adhesion probability is illustrated in (d).

To determine the adhesion probability for a flowing cell, unknown *A* and *B* in eqn. (3-5) should be evaluated first. Notably, different cancer cell types have varied biomolecule characterizations, which make *A* and *B* unique for each cancer cell line and each test condition with different antibody coating density. In this study, HCT-116 cells and an anti-EpCAM coating density of 10 μg/mL [68-69] were investigated. As described in the section of *Numerical Methods*, experiments combined with corresponding simulations were used to calculate *A* and *B*. As for *B*, since it reflects the adhesion probability under different shear stresses, a cell capture experiment was performed to extract *B* in a Hele-Shaw microfluidic chip, where the shear stress decreases linearly along the flow direction [107, 110]. Figure 3-2(a) shows the linearly decreasing shear

stress along the flow direction. The microfluidic chip was divided into multiple parallel sections along the flow direction with a width of 1 mm. The shear stress in the middle of each section was used as the average value. The amount of captured cells in each section was counted and normalized to the one in the last section where the shear stress was the smallest. Figure 3-2(b) shows an exponential fit of *B* following the format of eqn. (3-5). Based on the data fit, *B* was calculated as 7.3.

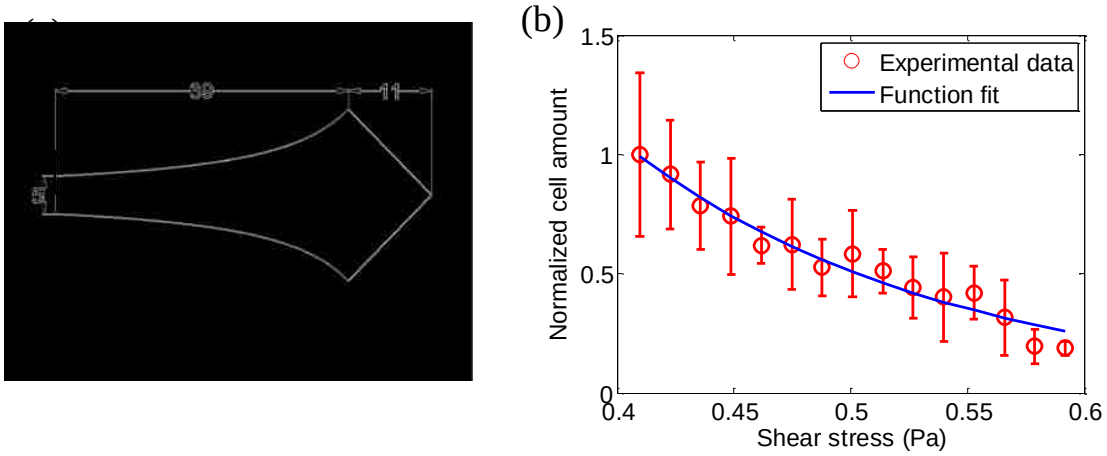

Figure 3-2 (a) A Hele-Shaw design with shear rate linearly decreasing along the flow direction ; (b) Normalized cell amount along the flow direction. The channel is divided into equal sections with a microscope window width of 1 mm. Cell amounts in continuous microscope windows are normalized by the average of cell amount in the last window section where the shear rate is the smallest. Error bars stand for standard derivation from five independent windows in each cross-section. An exponential curve fit is then applied to obtain the value of B.

As for *A*, it reflects the magnitude of adhesion probability under a certain shear stress. Specifically, the intrinsic ability for a cell to be firmly captured is positively proportional to *A*. To calculate *A*, we introduced a ridge-bottom ratio of amounts of captured cells which considered the capture performance on both groove ridges and groove bottoms. Cell capture experiments were first performed and captured cells on both groove ridges and groove bottoms were counted to calculate the ridge-bottom ratio. As

shown in Figure 3-3(a), this was repeated at four different shear rates which covered the range widely used in literature [35, 76]. On the other hand, attempts of numerical simulations to match with the experimental results were taken by substituting *A* of different values ranging from 0.01 to 500. For each *A*, ridge-bottom ratios at these four shear rates were calculated. The least square method was then used to calculate the sum of squared residuals between the numerical results and experimental results, as shown in Figure 3-3(b). It reveals that with increasing *A*, the overall trend of the error decreases first and then increases. The zoom-in image shows that the minimum error happens when *A* equals to 3.0. In other words, *A* with a value of 3.0 best reflects the real experimental condition. To be noted, Figure 3-3(b) also suggests that *A* smaller than 0.01 or larger than 500 leads to larger errors, thus these values were not tested.

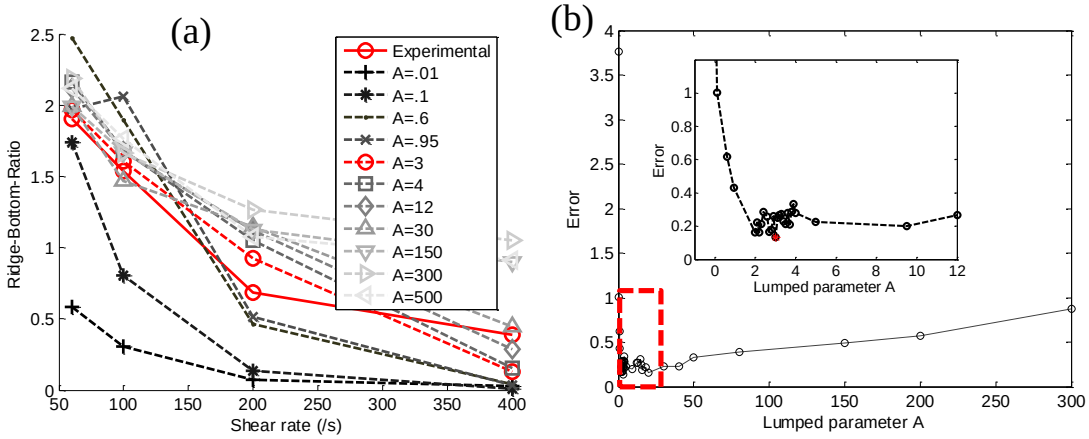

Figure 3-3 (a) Comparison of the ridge-bottom ratio of the captured cell amount between experimental and numerical results under various attempts of *A* ranging from 0.01 to 500. (b) The error calculated by the least square method under different *A*. The zoom-in image shows the optimized value for *A* where a smallest error exists.

By substituting both *A* and *B* to eqn. (3-5), the adhesion probability was simplified to be only dependent on the shear stress which was a function of the cell

position. As a result, a numerical model of cell dynamics integrated with adhesion probability was built and used for the geometric optimization study as detailed below.

3.4.2 Geometric Optimization

As shown in Figure 3-4(a), the capture efficiency slightly changes with the increasing number of the grooves, reaching the plateau after 6. In Figure 3-4(b), with increasing groove intersection angles, the capture efficiency first increases and then decreases in the turning point between 90^o and 120^o. The maximum capture efficiency happens at the groove angle of 90^o, where the stretching and folding of transverse flow reaches maximum thus generating significant mixing effects.

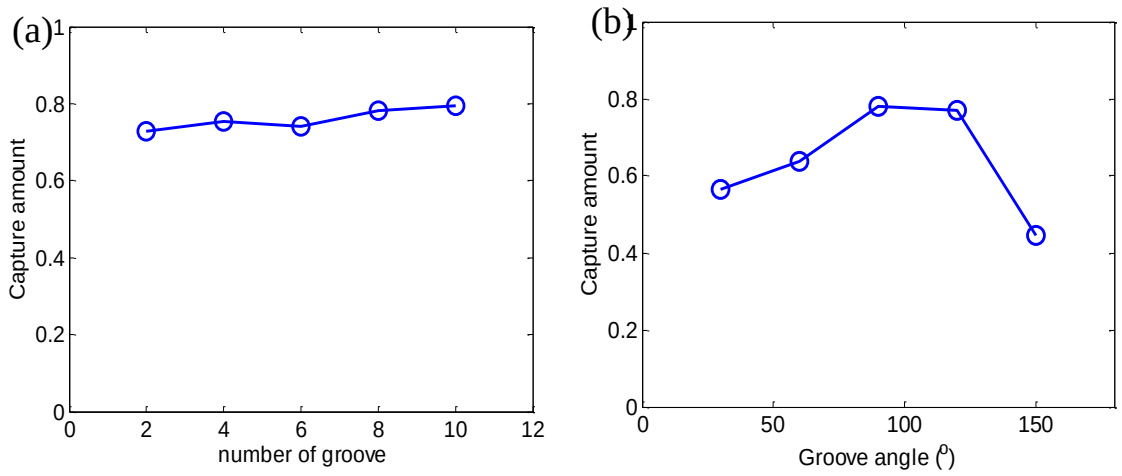

Figure 3-4 Numerical results of normalized capture amount under (a) different number of grooves per half cycle and (b) different groove intersection angles.

In Figure 3-5(a), *h/r* and *d/h* act differently on capture performance: capture efficiency decreases with increasing *h/r*, while it increases with increasing *d/h* and reaches a plateau after 1. This is explained as follows: with increasing *h/r*, the increasing free space for cell travel and relatively reduced chaotic effects allow for less cell-surface

interactions. On the other hand, with *d/h* increasing in the range of 0.2-1, the chaotic effect in the cross section can be enhanced, thus bringing more cells towards the capture bed. The interesting fact happens in the range of 1-4 where increasing *d/h* has little effect on the capture performance, which is speculated as the result of rare influence of the flow field induced by the extremely large hydraulic resistance in the groove bottom. In Figure 3-5(b), capture efficiency decreases with the increasing width periods, where the longer transverse travel distance weakens the mixing effect. Meanwhile, the increasing percentage of the short arm is shown to increase the capture efficiency, which is different from the result in literature where *d/h* of 1/3 is optimized for mixing. This significant difference is attributed to the fact that although asymmetric geometry can enhance the transverse flow thus increasing the mixing effects, it does not necessarily indicate enhanced cell-surface interactions. In other words, mixing effect is an overall term to evaluate the flow domain, while the cell capture only occurs close to the wall which cannot be determined by the overall flow pattern. This explanation again supports the view that mixing effect cannot be directly adopted to optimize the geometry for enhanced cell capture and an explicit model is needed for the geometry design.

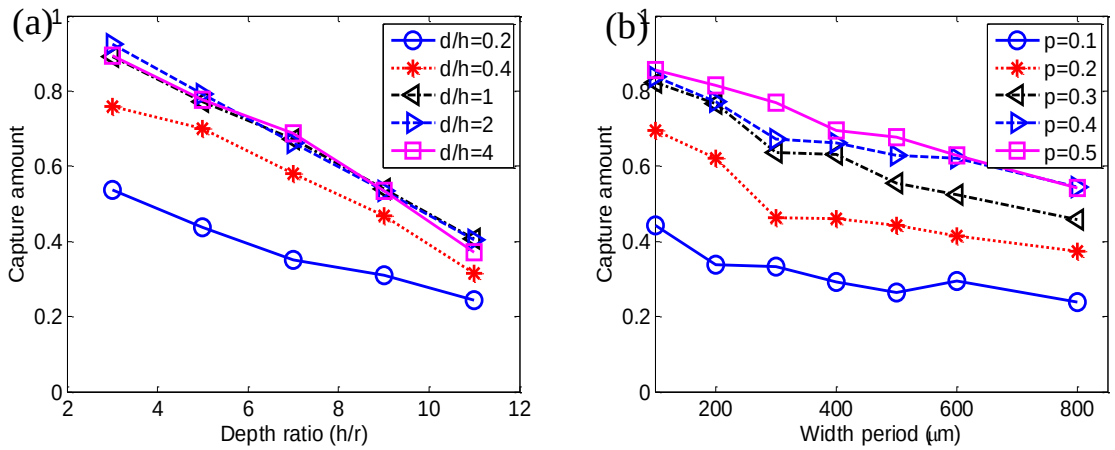

Figure 3-5 (a) Numerical results of normalized capture amount under different channel widths and different asymmetrical factors. (b) Numerical results of normalized capture amount under different channel heights and different groove depths.

In Figure 3-6(a), for a specific groove pitch, the overall trend of capture efficiency with increasing groove percentage is first increasing and then decreasing. This trend is explained by the trade-off of hydraulic resistance in the groove region and the channel planar region as shown in Figure 3-1(d). The hydraulic resistance is calculated as $R \approx 8\eta L / R_h^2 A$ in a channel with a rectangular cross-section. The hydraulic resistances in the groove section and the corresponding channel section can thus be calculated as $R \approx 8\eta L_{eff} \left(w_g + d_g \right)^2 / w_g^3 d_g^3$ and $R \approx 8\eta w_g \left(w_{eff} + h \right)^2 / w_{eff}^3 h^3$, respectively. Take the groove pitch of 200 μm as an example, as shown in Figure 3-6(b). Two different regimes are existed divided by the intersection point where hydraulic resistance in the groove region and the channel planar region are balanced: in regime I where hydraulic in the groove region is larger, with increasing trough widths, the rotational flow in the vertical direction is enhanced, thus increasing the cell deflection and cell-surface interactions; in regime II where hydraulic in the channel region is larger, with increasing trough width,

the continuously decreasing hydraulic in the groove region allows more cells freely flow in the groove region with less cell-surface interactions due to the decreased cell deflection effect. Given the mechanism, the trend of capture efficiency exactly follows the transition of regime I to regime II, where regime I dominates in the range of 0.1-0.5 while regime II in the range of 0.5-0.9.

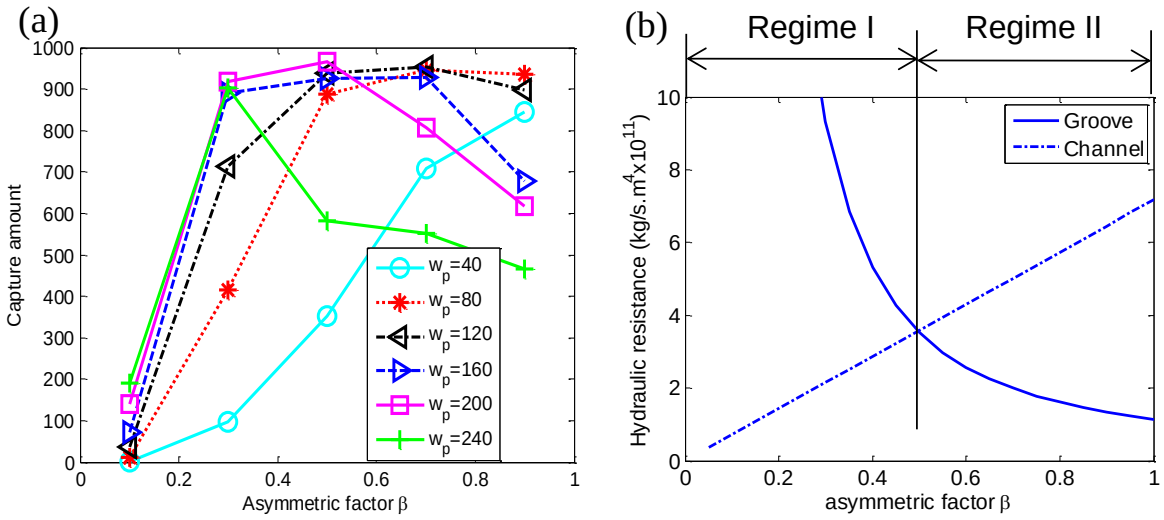

Figure 3-6 (a) Numerical results of normalized capture amount under different groove pitches and groove widths. (b) Theoretical hydraulic resistance calculated for both the bottom groove and the upper plain channel in a herringbone microfluidic chip with a groove pitch of 200 μm. The intersection point indicates a flow resistance balance between the groove and the plain channel.

To unravel the capture efficiency in a specific microfluidic device, it is essential to understand the cell-surface contact frequency in different areas. Specifically, the higher the cell-surface contact frequency, the larger chance for a cell to be captured. A HB microfluidic device is divided into four different sections where the cell-surface contact frequency is calculated respectively, as sketched in Figure 3-7(a). Given the fact that a few recent studies indicated the critical role of the groove asymmetry in determining the CTC purity performance which is another important criterion in

designing a microfluidic device [55], the effect of the groove asymmetry is of special interest in this study. Figure 3-7(b) shows the cell-surface contact frequency in the prescribed areas under various groove asymmetric factors. The overall trend of the total contact frequency agrees well with that of the capture efficiency, which first increases and then decreases with increasing asymmetric factors. Furthermore, it suggests that cells have the largest chance to contact with the groove ridge. In the respect of designing optimized microfluidic chips, it will be most effective if any strategy is introduced to enhance cell capture in the groove ridge section. For example, since nanostructures was found to enhance the CTC capture due to the increased cell-surface contact area, an integration of nanostructures on the groove ridge can contribute most to the enhanced CTC capture. Especially in certain situations where difficulties lie in fabricating nanostructures uniformly over the groove-HB structures [111], a local integration of nanostructures on the groove ridge can suffice.

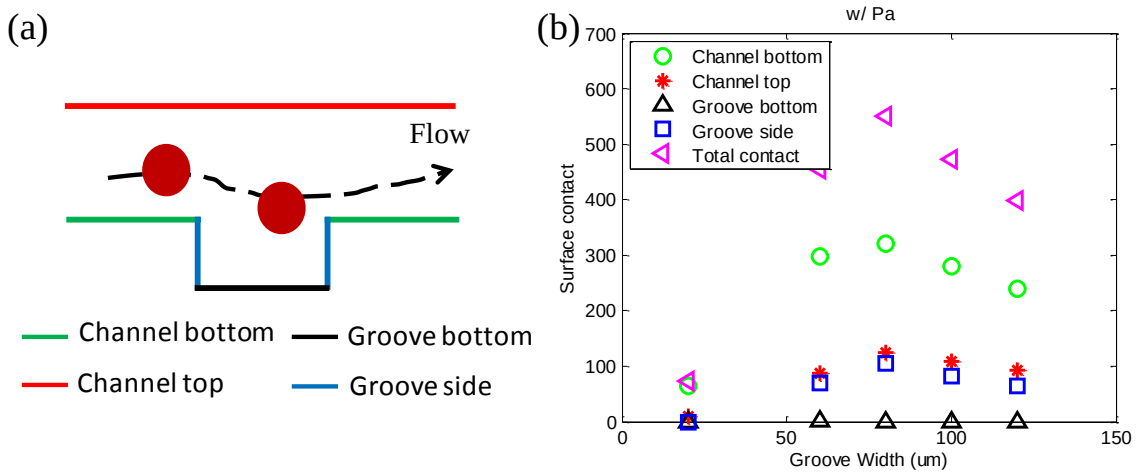

Figure 3-7 (a) Schematic diagram of a herringbone microfluidic chip from the side view. The channel surface is divided into four sections marked in different colors. (b) Numerical results of cell-surface contact frequencies in different sections under different groove widths with a fixed groove pitch of 160 μm.

3.5 Conclusion

We present an explicit computational model integrated with adhesion probability to investigate geometric effects on tumor cell capture performance for a HB microfluidic device. To evaluate the adhesion probability for specific cell lines and antibody coating conditions, two sets of microfluidic experiments combined with corresponding simulations are used to extract two lumped parameters which directly determine the adhesion probability. In this study, HCT-116 cells and 10 μg/mL anti-EpCAM coating condition were used an example to demonstrate the approach to determine these two lumped parameters. By using the developed computational model, a better understanding of geometric effects on tumor cell capture was achieved for a hallmark HB microfluidic device. Most significantly, the results suggest a short arm ratio of 0.5 for optimized tumor cell capture which is against from 1/3 obtained from most studies [56, 112]. This difference is attributed to the intrinsic difference between particulate cell model and pure mixing model. Specifically, our model integrates the particulate cellular properties, while most works in literature [112-114] only reply on the mixing effect to design a HB microfluidic device for CTC capture which cannot directly reflect the cell-surface interactions. As a result, this improved computational model can provide a more accurate and reliable geometric design criterion for optimized tumor cell capture in microfluidic devices. One limitation on the current model lies in the neglect of cell-fluid interactions which are also important in determining cell motions in the scale of most tumor cell capture microdevices [104-105]. A more comprehensive model will be implemented in our future work.

Chapter 4: Geometric Effects of Nanopillars for CTC Capture

4.1 Introduction

Circulating tumor cells (CTCs) are cells that shed from a tumor mass and circulate in peripheral blood. Detection and analysis of CTCs can guide cancer diagnosis, prognosis and treatment [84, 115-116]. Isolation of CTCs from patients' blood attracts significant attention as a first step toward CTCs analysis. A variety of techniques have been developed in the past decades, which rely mainly on physical properties (e.g., size, density and deformability) [117-119] or expressions of biomarkers [30, 43, 120-122]. However, most of these methods failed to show clinical validity or utility, thus remained in the laboratory settings due to their limited isolation efficiency and the rarity of CTCs, i.e., as few as 1 CTC per 1 mL peripheral blood. Therefore, improvement of CTC isolation efficiency and specificity is a pressing issue.

Recently, nanostructured substrates have emerged as a promising CTCs detection and isolation platform since they can provide high isolation efficiency (80-95%, normally ~90%) [123-127]. The cell-nanostructure interaction has also been reviewed comprehensively and several basic design principles has been delivered [23]. For the selection of nanomaterials, silicon nanomaterials are a good candidate for CTC study due to their biocompatibility and unique electronic properties [24]. Compared to flat surfaces, nanostructured substrates provide larger surface area for the immobilization of anti-epithelial cell adhesion molecule (anti-EpCAM), increasing the binding odds between

antibody and membrane receptor and also total binding forces, thus enhancing CTC-isolation efficiency. Moreover, the natural extracellular matrix or basement membrane mimicking nanostructured substrates offer a suitable environment for CTCs attachment. In previous studies, nanostructures with size ranging from 30 to 1150 nm have been employed for CTCs isolation, and high efficiency was reported in all cases. For instance, 88% of cancer cells were captured onto antibody immobilized silicon nanowires (SiNWs) with diameter of 50-160 nm [128]; high isolation efficiency up to 95% was reported on antibody grafted silicon nanopillars (NPs) with diameter in the range of 100-200 nm [39]; cancer cell isolation efficiency on antibody grafted spherical particles with diameter of 232 nm was 4-5 times higher than on a flat surface [129]. Nanostructured surfaces with halloysite nanotubes was also demonstrated to enhance the CTC recruitment with a three-fold increase for MCF7 cells, while nonspecific leukocytes adhesion was prevented [130]. Meanwhile, efficient CTC capture with high selectivity has also been reported by using functionalized graphene oxide nanosheets [131] or soft polystyrene nanotube substrates [132]. Recently, developing multifunctional platforms modified with nanostructures comes to be of significant research interests for biomedicine applications. A nanodendritic silica coating has been developed to not only efficiently capture CTCs, but also own the ability to directly monitor the results due to its transparency under water [133]. Controlled CTC release after cell capture has also aroused more attention since it is very important for subsequent cell analysis [134]. A thermoresponsive substrate with NPs was developed to capture targeted CTCs and then release CTCs in a prescribed manner [135]. Efficient CTC capture and release process has also been achieved by using programmable fractal gold nanostructures through an electrochemical method [136].

Nevertheless, preferred nanostructure geometry is still unclear for CTCs isolation. A quantitative study of the relationship between capture efficiency and nanostructure geometry is necessary for the optimization of substrate topographical design for CTC isolation. At the same time, morphology of captured cancer cells on nanostructured substrates is not conclusive either. In previous reports, the captured cells were found to be flatter on aptamer grafted nanostructured substrates than that on planar surfaces: cells changed from a globular shape to a semielliptical one [30, 137]. The flatter shape of captured cells indicated that more receptors on the cell membrane make contact with immobilized antibodies; meanwhile, the decreased cell height further prevented them from being eluted under high shear stress [137]. Contrarily, it was reported that the high aspect ratio of bare SiNWs and polystyrene (PS) NPs support cell adhesion but restrict cell spreading due to insufficient area for development of micron-scale focal adhesion [138-139]. Furthermore, nanostructured substrates may also influence the pseudopodia formation. Captured cells showed either significant lamellipodia or filopodia on nanostructured substrates with certain aspect ratios [140].

In this study, we investigated the effects of NP geometry on cell capture yield, cytomorphology and pseudopodia formation. Capture yield is defined as the ratio of cells captured on the NP substrate to total number of cells initially loaded. Our results showed that capture yield is linear to effective contact area of the NP substrate. Dense NPs with smaller diameter yield larger effective contact area, thus were preferred. However, once the spacing between NPs was smaller than the size of a microvillus (<100 nm) or was too large (>800 nm), cell capture yield and specificity were significantly impaired. We also confirmed that the formation of either lamellipodia or filopodia correlates with adhesion

status and eluting strength. Specifically, under the same shear stress, lamellipodia were generally formed on NPs with high aspect ratio (>10) where captured cells were firmly attached; furthermore, significant filopodia formation was observed on NPs with low aspect ratio where captured cells were more prone to detach, indicating filopodia might obtain newborn adhesive force to resist shear stress mediated detachment [141].

4.2 Experimental Details

4.2.1 Fabrication of Silicon Wafers Covered with NPs

Silicon wafers covered with NPs with different diameters were fabricated by metal assisted chemical etching [142]. In detail, the silicon surface (Si (100), B-doped, 0.004-0.007 Ωcm) was cleaned by a RCA-I approach. Deionized water, ammonia solution (25%) and hydrogen peroxide (30%) were mixed in ratio of 5:1:1. The solution was heated up to 80 degrees and silicon chips were cleaned for 15 mins. Afterwards nanospheres (polystyrene (PS) with diameters: 1.39 µm, 722 nm and 390 nm) were deposited by a modified Langmuir-Blodgett technique in monolayer for lithographic structuring. In the next step the PS-spheres were etched in O_2-plasma to reduce their diameters. Following silver (30-60 nm) was evaporated onto the surface. PS-spheres were lifted off by dichlormethane in an ultra-sonic bath and the chips were rinsed with acetone, ethanol and deionized water. Thus a metal film on silicon with specific openings was created. The size of the openings correlates with the size of the plasma-etched PS-spheres. After that etching in a hydrofluoric acid and hydrogen peroxide based solution was carried out. The solution consists of 37 mL deionized water, 12.5 mL hydrofluoric acid (40%) and 0.5 mL hydrogen peroxide. The chips were etched for 5 mins. The metal film sinks into the silicon, which is solved by the etching solution. In the end, around 1 µm

long NPs were obtained and silver was removed by concentrated nitric acid for 2 mins. The diameter of the NPs is equal to the size of the opening in the metal film and is also equal to the diameter of the PS-spheres after plasma-etching. Finally, 5 x 5 mm wafer substrates with NPs of diameter ranging from 120 nm to 1100 nm were attained.

4.2.2 Surface Functionalization of Anti-EpCAM

Prior to the surface functionalization, all the wafer substrates were washed using a three-step cleaning process (acetone, isopropyl alcohol and DI water), and dried under nitrogen [120]. Then, wafer substrates were fixed in 35x10 mm petri dishes and treated with oxygen plasma to confer the hydroxyl groups on the substrate surface. In order to chemically modify the substrate, a three-step surface functionalization process was immediately applied. They were firstly pretreated with 5% (v/v) 3-mercaptopropyl trimethoxysilane in ethanol for 30 minutes at room temperature (RT), followed by incubation with 0.01mM N-y-maleimidobutyryloxysuccinimide ester (GMBS) in 200 proof ethanol for 30 minutes at RT. NeutrAvidin was then immobilized to GMBS by incubating the substrates with 10 µg/ml NeutrAvidin in phosphate buffered saline (PBS) overnight at 4^{o}C. Within 24 hours of the experiment, 10 µg/ml biotinylated goat antihuman EpCAM solution in PBS containing 1% (w/v) bovine serum albumin (BSA) were added to the substrate for 2 hours at RT. After each reaction, PBS or ethanol, depending on the solvent used in the previous step, was used to remove unbounded molecules. One hour prior to running the cell test, the substrates were purged with 3% BSA with 0.05% Tween20.

4.2.3 Cell Culture and Cell-test Sample Preparation

PC3 prostate cancer cells was selected as an appropriate platform for optimization study of capture of CTCs, as lower concentration of EpCAM, namely 51667 molecules per cell, was expressed for PC3 cells [120]. PC3 cells were cultured at 37 ^{o}C in 5% CO_2 in F-12K growth medium containing 1.5 mM L-glutamine supplemented with 10% fetal bovine serum (FBS) and 1% Penicillin/Streptomycin with media change every 2-3 days. Cells were then released through incubation in 0.05% Trysin-0.53 mM EDTA at 37oC for around 5 minutes. Hemocytometer was used to count cells and according dilution was subsequently pursued to reach a cell concentration around 105/mL [128]. The cell concentration was selected also for ensuring the yield of a large result data pool to reach a reliable conclusion.

4.2.4 Cell-capture Yield Test and Cell Detachment Test

For the cell-capture yield test, 20 μL of cell solutions was added to the wafer substrates and immediately followed by incubation at 37 ^{o}C in 5% CO_2 for different incubation time mentioned in the manuscript. Next, 2 mL of PBS buffer solution was added to the petri dish, which was then fixed on the shaker. Different shaking speeds and different lasting time were applied to detach PC3 cells, followed by removing all suspensions. Both regular microscope and scanning electron microscopy (SEM) were applied to analyze the results including cell amount, geometry and morphology.

For SEM specimen preparation, a standard procedure reported in our previous work [137] was followed. Briefly, Cells were firstly fixed with 4% paraformaldehyde at 4 ^{o}C for 1 hr. Next, paraformaldehyde was removed and cells were rinsed by PBS buffer

solution twice. Cells were then dehydrated in ethanol with a concentration gradient of 20%, 30%, 50%, 70%, 85%, 95%, and 100% (15 minutes in each solution). After treatment of 100% ethanol, all cell samples were lyophilized overnight. Finally, dehydrated cells were sputter coated with gold and imaged by Zeiss 1550 SEM. Images of cells from both upright view and tilted view were scanned for post-analysis.

4.2.5 Quantitative Analysis of Cell-capture Yield, Cell Morphology and Substrate Wettability

To calculate cell capture yield, SEM images were taken section by section throughout the whole substrate and amount of captured cells was then counted. As for the quantitative analysis of cell morphology, SEM images of top view were used for calculating the apparent contact area by tracing the boundary of captured cells using ImageJ software (NIH). Meanwhile, SEM images of tilted view were used for measuring the height of the captured cells, which was modified by the tilted angle of the stage (80 degrees). For each SiNP substrate type, 20 cells that were well separated from other cells were measured. Furthermore, wettability of functionalized and non-functionalized substrates was evaluated by measuring their contact angles. 1.5 μL, 3 μL and 4.5 μL of water droplet was added to the substrates and images were then analyzed using "contact angle" plug-in in ImageJ.

4.2.6 Calculation of Maximum Displacement of One Individual NP

For one individual NP with diameter of 120 nm, it endures both focal complex force (0.8-0.9 nN/μm^2) [143] and ligand-receptor bond force ($6.7\times10^{-6}\,dyn$ for one bond) [144]. Focal complex force was applied in the top surface of NP and ligand-receptor bond

force in both top surface and side wall. Following this boundary setup, an FEM study using Comsol software was pursued to study the maximal displacement.

4.2.7 Study of Substrate Wettability through Cassie's Law

In our NP substrate system, with the fact that the substrate surface was silicon dioxide which was hydrophilic, the Cassie's law gave the contact angle θ as $\cos\theta = f_1 \cos\theta_1 + f_2 \cos\theta_2$, where f_1 and f_2 are the fractions of the solid phase (namely packing density of NPs) and water phase which compose the entire surface, respectively. θ_1 and θ_2 are contact angles for the solid phase and water phase, respectively. Noticed $\theta_2 = 0$ for water phase. So the equation of contact angle θ were simplified as: $\theta = \arccos\left(f_1 \cos\theta_1 - f_1 + 1 \right)$.

4.3 Results and Discussion

4.3.1 Fabrication and Characterization of NP Arrays

Anti-EpCAM coated NPs with diameter ranging from 100 to 1100 nm, spacing ranging from 30 to 800 nm, and fixed height of 1 μm were prepared. A schematic of the fabrication process and a tilted SEM image of fabricated NPs are shown in Figure 4-1(a) and 1(b), respectively. The average diameter, spacing and standard deviation (SD) of each group (n=30) are summarized in Table 4-1. The variations of diameter and spacing from each group are within 2-8%, arising from the size distribution of PS-spheres and different O_2 plasma treatment time. To avoid truncated cone structures or collapse of NPs all groups were etched for 5 minutes only, and thus NPs with same length of 1 μm were obtained.

Table 4-1 Geometrical Properties of NP arrays. Different groups are named as "NP" followed by their average diameters.

Group	Diameter of NPs [nm]	Spacing [nm]
NP120	118.2±9.4	154.3±17.5
NP200	204.8±7.3	154.9±14.9
NP300	292.7±11.3	38.7±2.5
NP550	571.5±36.5	144.0±10.5
NP650	649.6±38.1	797±126.1
NP1100	1147.8±23.1	189.2±25.0

We first characterized various NPs' compliance, packing density and wettability. Bending compliance affects the adhesion, spreading and migration of attached cells [140, 145], and was calculated as:

$$C = \frac{64h^3}{3\pi ED^4} \tag{4-1}$$

where h and D are the height and diameter of NPs, respectively; E is Young's modulus of NPs with a value of 70 GPa [146]. Figure 4-1(c) shows NPs with smaller diameter yield a larger compliance, indicating a potential of a larger deformation. As such, NP120 with smallest diameter were considered for deformation analysis. When an individual NP120 is subjected to both focal complex force (0.8-0.9 nN/μm^2) [143] and ligand-receptor bond force ($6.7\times10^{-6}\,dyn$ for each bond [144] and approximately 51667 EpCAM per PC3 cell [31]), its maximal tip displacement is 0.0046 nm (Figure 4-1(d)). With such negligible

deformation, all NPs were considered as rigid. SEM images further confirm that most of NPs stand straightly (Figure. 4-3(b-c) and Figure 4-6(f-g)). With a hexagonal NP array, packing density η was calculated as:

$$\eta = \frac{\sqrt{3}\pi}{12\left(1+{D_g}/{D}\right)^2} \tag{4-2}$$

where D_g is the spacing between two neighboring NPs. As shown in Figure 4-1(c), NPs with larger diameter were more densely packed. For comparison purpose, a denser ($\eta = 0.71$) and a sparser ($\eta = 0.18$) packing pattern were obtained from NP300 and NP650, respectively, due to their extraordinary spacing (Table. 1). We then investigated the wettability of NPs by studying the contact angles of water droplets on substrates. On a heterogeneous surface, nanostructured patterns have been reported to enhance surface hydrophobicity or hydrophilicity [147]. As a result, SiNP substrates were enhanced to be superhydrophilic due to its hydrophilic nature of oxidized surface in air with contact angle less than 10°. The measurement results are well fitted with the values calculated by applying Cassie's law (Figure 4-1(e) and see Supporting Information S2 for more details). It should be noted that surface functionalized with antibodies insignificantly increased wettability due to the inherent superhydrophilic property of NPs.

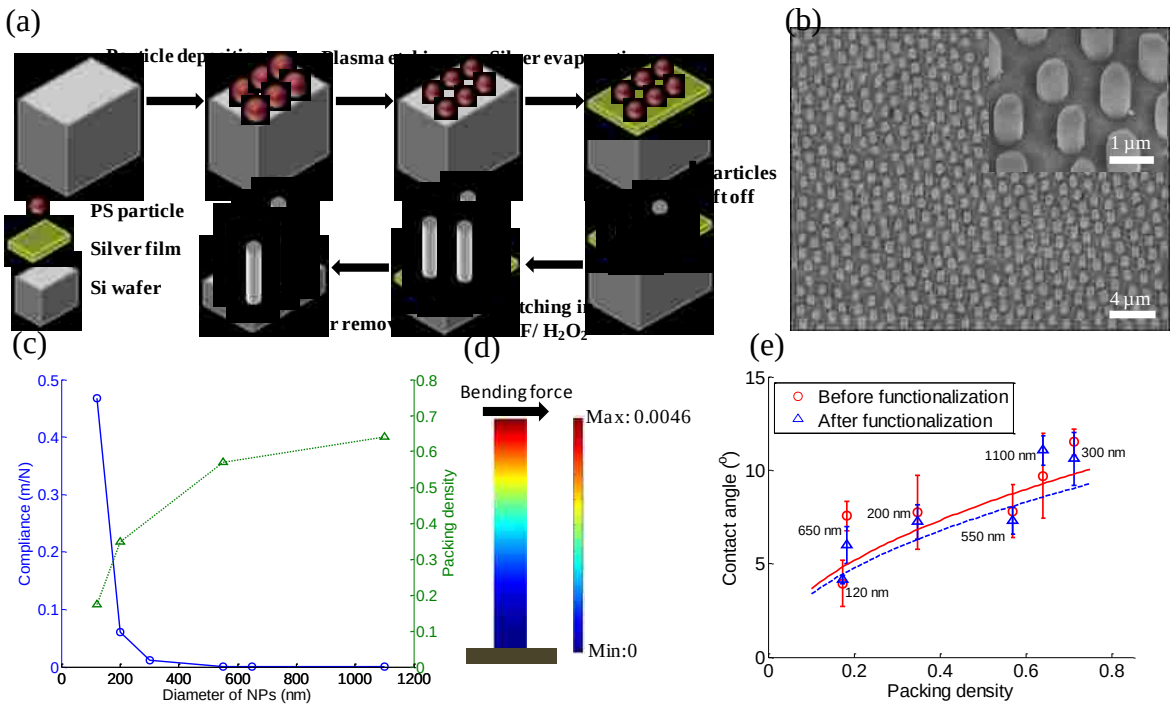

Figure 4-1 (a) Fabrication process of NP arrays by metal assisted chemical etching method. (b) A typical SEM image of NP arrays with average diameter of 650 nm from tilted view. The inset in (b) shows the magnification of NPs from tilted view. (c) Mechanical and geometrical properties of NP substrates: compliance and packing density. (d) A finite element method (FEM) analysis of a single bending NP showing the displacement of an NP with diameter of 120 nm. The unit of the color bar is nanometer. (e) Wettability of different NP substrates before and after functionalization. The solid line and dashed line stand for fitted curves using Cassie's law for non-functionalized and functionalized NP substrates, respectively. Error bars in (e) stand for standard derivation from three independent experiments.

4.3.2 Selection Criteria for Incubation Time and Shaking Speeds

As shown in Figure 4-2(a), incubation time ranging from 5 mins to 2 hrs was applied with 10 mins' shaking in 60 rpm. It was observed that, for bare wafers with anti-EpCAM coated, capture yield increased with incubation time, reaching a plateau of 22.9% in 1 hour. No significant difference of capture yield was observed after 1 hour, with 23.1% and 24.4% for 90 minutes and 120 minutes, respectively. Rare capture for bare wafer with 1% BSA coated verified that capture of PC3 cells in anti-EpCAM group was

induced by specific bonds between PC3 cells and anti-EpCAM. Moreover, aim of this work is to study cell capture other than cell adhesion/migration, so that focal adhesions fully established in around 1 hr [143] was not considered in our case. Timescale of 1 hour was also widely adopted in other relative work [125]. With these, 1 hour of incubation was applied for all the following studies. As shown in Figure 4-2(b), shaking speeds ranging from 60 rpm to 400 rpm were applied after 1 hour's incubation. The relationship between maximum orbit shear stress and shaking speed was expressed as: $\tau_{o\max} = a\sqrt{\eta\rho(2\pi f)^3}$, where, a and f are orbit radius (0.95 cm) and frequency (rotation/sec depending on shaking speeds) of the rotation of the shaker, respectively; η (0.90 mPa·s) and ρ (0.995 g/mL) are dynamic viscosity and density of the medium, respectively [148]. As such, shaking speed between 60 rpm and 400 rpm corresponds to orbit shear rate between 157.3/s and 2708/s, which covered the majority range reported in literature: 267/s-1067/s [121] and 83/s-1166/s [149]. As expected, due to increased shear stress, capture yield decreased with increasing shaking speed and the biggest capture yield was obtained in the shaking speed of 60 rpm. The calculating shear stress of 0.24 dyn•cm^{-2} in 60 rpm was also observed to achieve more than 95% capture yield in a previous study [149]. Rare capture for bare wafer with 1% BSA coated again verified that capture force was generated by the specific bond between PC3 cells and anti-EpCAM. It also indicated that 60 rpm was enough to elute suspended cells. As a result, the optimal shaking speed of 60 rpm was adopted for all the following studies.

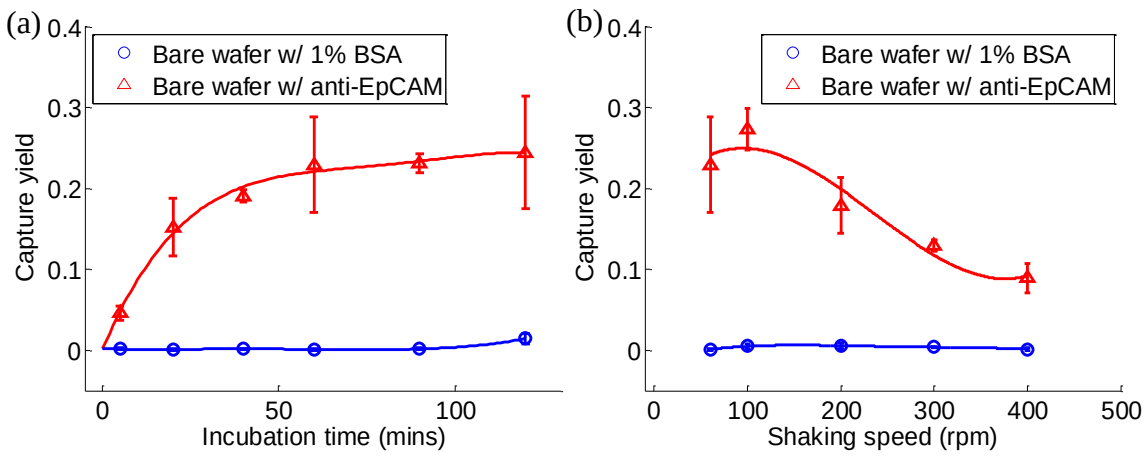

Figure 4-2 Quantitative evaluation of capture yield for cases with 1% BSA coated and with anti-EpCAM coated (a) at different incubation times followed by 10 minutes of shaking in 60 rpm and (b) after 1 hour of incubation followed by 10 minutes of shaking under various shaking speeds. Each error bar represents a standard derivation and is obtained from three independent experiments.

4.3.3 Spacing and Diameter Effects of NPs on Cell Capture Yield and Cell Behaviors

The cell-NPs incubation time and orbit shear stress for eluting were optimized on planar wafers first (see Supporting Information S3 for more details), and the selected conditions were applied throughout the study in all NPs groups. The capture yield reached plateau after one hour (Figure 4-2(a)). Shaking at 60 rpm for 10 minutes effectively detached nonspecifically attached PC3 cells while maintaining the maximal capture yield (Figure 4-2(b)).

With the proper experimental conditions determined, we next examined spacing effects on capture yield and cell behaviors. Figure. 4-3(a) shows the average diameter of a microvillus was 105.8 ±14.8 nm measured from zoomed-in SEM images of a single cell sitting on a bare wafer, which is in agreement with previous reports [150]. 6 NPs groups were thus divided into 3 different categories: NP300 with extremely small spacing (~40

nm), NP650 with extremely large spacing (~800 nm), and the remaining 4 groups with approximately similar spacing (140-190 nm). Low capture yield of 24.3%±6.3% was found in NP300 group, which was close to 22.9% obtained on a planar wafer (Figure 4-4(a)). We speculate that such low capture yield is likely due to the small spacing that prevents microvilli or pseudopodia from penetrating through the gap and contacting with the lateral surface of NP300. Thus cells were unable to gain sufficient adhesion force to resist the following eluting shear stress. As cells only contacted with the top surface of NP300 (Figure. 4-3(b)), cells on NP300 showed a globular shape which was unlike the flat cell morphology in other groups. On the contrary, cells showed a very flat shape on NP650, where microvillus or pseudopodia easily filled into the 797 nm spacing (Figure. 4-3(c)). Compared to cells on NP300 these cells had larger contact area and gained bigger adhesion force. Hence, relatively higher capture yield of 46.95%±18.7% was obtained on NP650; however, due to its sparse packing pattern (Figure 4-1(c)) and relatively smaller effective contact area (discussed later), capture yield on NP650 was still low (Figure 4-4(a)) in comparison to NP120 and NP200. The significantly higher SD on NP650 was also likely to be caused by larger spacing in which cells can physically situate in various ways. Thus, the nonspecific settlement may contribute to the large capture yield fluctuation. In the remaining 4 groups with 140-190 nm spacing, cells spread moderately and effectively interacted with NPs' lateral walls (Figure. 4-3(d)); the capture yield ranged from 28.0% to 80.8% along with the increased effective contact area of each group (discussed later). The above results indicated that spacing is an important factor that is directly related to capture yield. Dense NPs with very small spacing (~ 50 nm) adversely impairs cell capture yield. In one previous study, dense silica bead (diameter

ranges from 100 to1150 nm) were deposited closely onto a glass slide without any spacing, cell capture yield was only 1.2-1.6 times higher than that on a planar surface [151]. This result also indicates the spacing plays an important role in capture yield. On the contrary, increased nonspecific settlement may appear on sparse NP surface when the spacing is larger than 500 nm, i.e., diameter of filopodia. Considering the spacing of NP120 and its over 80% capture yield (Figure 4-4(a)), 140-200 nm spacing probably well suits the needs of efficient and specific capture.

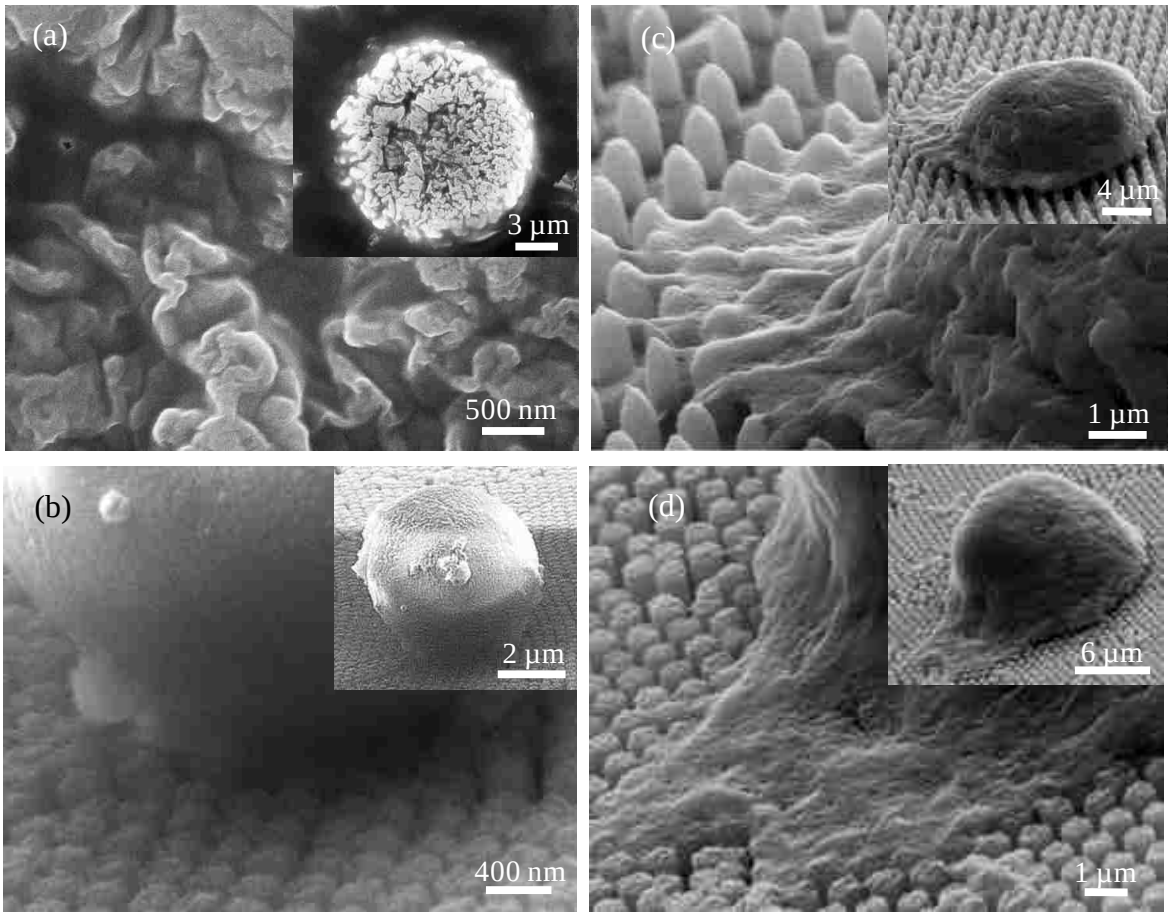

Figure. 4-3 (a) Zoomed-in and zoomed-out SEM images reveal details of microvilli on the cell membrane. (b)-(d) Cell behaviors in NP substrates with a spacing of 38 nm for NP300 in (b), 790 nm for NP650 in (c), 140 nm for NP550 in (d). All cells were incubated for 1 hr followed by 10 mins of shaking in 60 rpm.

We then examined the effects of diameter of NPs on capture yield and cell behaviors. In the remaining 4 groups, diameter of NPs was considered as the major varying factor. The spacing ranged from 144.0 nm to 189.2 nm with the maximal difference 45.2 nm was smaller than the diameter of a single microvillus, thus was treated as a minor factor here. The average spacing of 160.6 nm (SD: 19.7 nm) of the 4 groups was generally adopted for the following studies and discussion. Figure 4-4(a) shows that capture yield decreased with increasing diameter of NPs, reaching 28.0%±3.9% in NP1100 group which was almost the same as that in planar wafer case (22.9%). We explained this trend by adhesion strength induced by NP-cell interaction and thus introduced two parameters: apparent contact area A_a and effective contact area A_e. A_a was defined as the projection area of a captured cell from top view; A_e was defined as the area of the NP substrate with chances to touch the captured cell. It was calculated as the whole surface area of the NP substrate consisting of top, lateral and bottom surfaces beneath the captured cell as shown in Figure 4-4(b). This is because microvilli (diameter: 100-120 nm; length: 2-4 μm) and filopodia (diameter of 100-500 nm; length from few microns to >50 μm) can fit into the spacing of NPs, and can even reach the bottom of the substrate. Through SEM images of the captured cells, we measured apparent contact area A_a (Figure. 4-3(a)) and cell height (Figure 4-4(b)) from top and tilted view, respectively, and summarized in Figure 4-4(c); all data points were well fitted by a rectangular hyperbola, indicating that estimating the average volume of cells as a simplified cylinder-like shape was consistent in each group. According to the definition of effective contact area, A_e was further calculated as:

$$A_e = A_a\left(1+\eta\frac{4h}{D}\right) \tag{4-3}$$

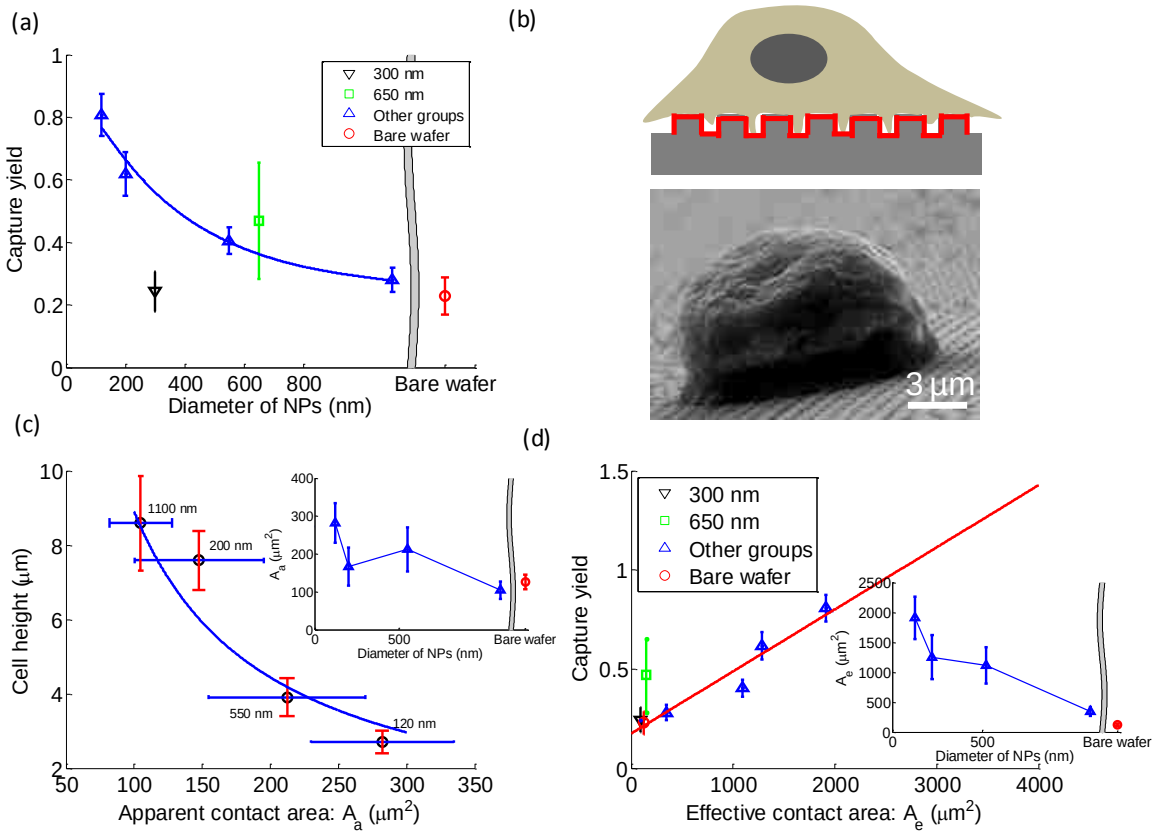

Figure 4-4 (a) Cell capture yield measured on substrates with different diameters of NPs after 1 hour of incubation and 10 minutes of shaking in 60 rpm. (b) Schematics (not in scale) of a captured cell on an NP substrate with red bold line marked as the effective contact area, and a typical SEM image of a captured cell on NP1100 from tilted view. (c) Cell morphology consisting of cell height and apparent contact area for different NP substrates. The inset of (c) shows apparent contact areas for NP substrates with various diameters and planar wafer. (d) Cell capture yield measured on NP substrates with various diameters and planar wafer. The inset in (d) shows effective contact areas for NP substrates with various diameters and planar wafer. The solid line in (d) stands for a linear fit. Error bars for capture yield in (a) and (d) stand for standard derivation from three independent experiments. Error bars in (c) stand for standard derivation from 20 arbitrary cells' measurements.

Figure 4-4(e) showed A_e decreased with increasing diameter as expected, indicating NPs with smaller diameter have larger surface area. Figure 4-4(d) revealed that capture yield decreased linearly with decreasing A_e. Furthermore, the linear function also applied to planar wafer and NP300 cases, where A_e is exactly or approximately equal to A_a. However, the linear function did not apply for NP650, mainly due to cells' nonspecific settlement as discussed above. Contrarily, we did not observe an apparent relationship between capture yield and A_a (Figure 4-5). It was concluded that nanostructured surfaces can provide larger surface area for enhanced antibody immobilization; larger antibody functionalized area can significantly increase the odds of antibody-receptor binding and thus the cell capture yield [123]. Another previous report also validated that cell capture yield can be improved by increasing the total area of gold clusters on SiNWs for antibody immobilization [128]. Nevertheless, we clearly showed for the first time that capture yield was linearly associated with A_e instead of A_a on substrates with nano-patterns. Therefore, with suitable spacing of 140-200 nm, higher capture yield can be obtained with smaller NPs of larger surface area for more antibody immobilization.

In addition to the effects of diameter of NPs on capture yield, we also observed different cell morphologies and spreading effects on antibody-coated NPs with different diameters. First of all, cells had relatively flat shape on the remaining 4 NPs groups (Figure 4-6). As shown in Figure 4-4(c), we observed an overall decreasing of A_a and increasing of cell height with increased NPs diameter. As a result, captured cells were able to endure higher shear force on smaller NPs, thus leading to higher capture yield.

Our previous work has also verified that decreased cell height further prevented captured cells from being washed away under high flow velocity [106]. Additionally, the inset of Figure 4-4(c) shows that antibody-coated NPs did not necessarily inhibit the cell spreading compared to planar wafers, which is different from a previous study [139]. In our previous report, epidermal growth factor receptor (EGFR) overexpressed cancer cells became flatter and reshaped to cover as large of an anti-EGFR aptamer functionalized area as possible [30]. On the contrary, cells on mutant aptamer substrates (control group) maintained a globular shape. Such spreading and flatness of cancer cells on aptamer surfaces have been proven to be a potential modality for discrimination of cancer cells from healthy cells [152]. Similarly, on anti-EpCAM functionalized surfaces in our case, PC3 cells also spread well due to the intense interactions between antibodies and receptors; cells gradually spread onto the substrate which was facilitated by the newly generated affinity bonds at the contact edge of cell-substrate. In the other scenario of planar wafers, cells have to develop micron-scale focal adhesions independently; NPs with high aspect ratio might fail to provide sufficient areas for development of focal adhesion and thus cell spreading was inhibited on bare NPs. It was also noted that cells on NP550 showed larger A_a with smaller height compared to that on NP200. We speculated that it might be due to the complementary size match between the diameter of NPs (550 nm) and focal complex (generally with size around 500 nm), although the exact mechanism behind this phenomenon is still unknown.

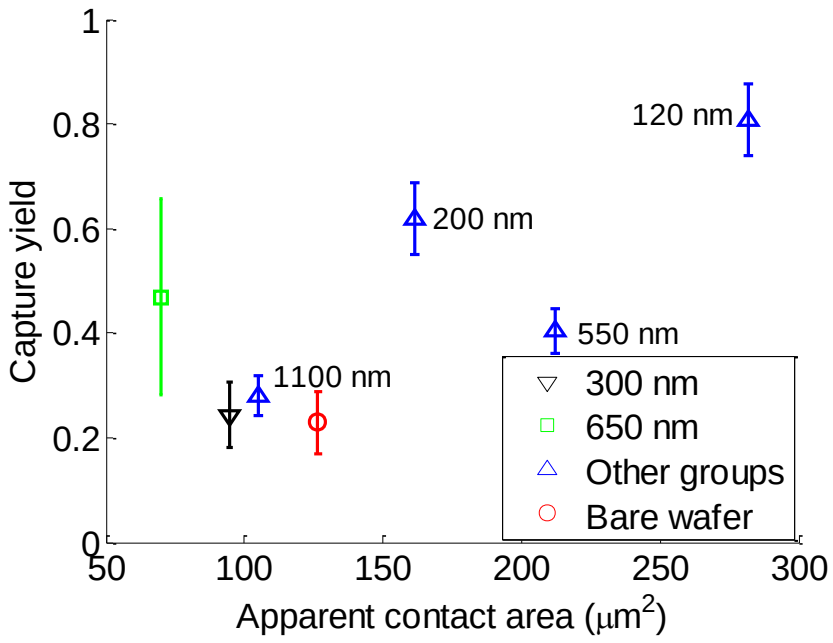

Figure 4-5 Capture yield in terms of different apparent contact area.

Finally, we studied the formation of subcellular adhesion structures under shear flow. It was observed that the formation of pseudopodia under shear is closely correlated with cellular adhesion status, shear force and shear direction. Figure 4-6(a) and (b) show a schematic of the experimental setup and locations of each wafer substrate corresponding to (c)-(i). We first examined cell behaviors on anti-EpCAM functionalized planar wafers at shaking speeds of 0, 60 and 400 rpm for 10 minutes after one hour of incubation. When shear force increases, a continuous transition of cell behaviors is observed, from being intact, dominant expression of lamellipodia to significant formation of filopodia (Figure 4-6(c)-(e)). Next, we examined cell behaviors on NP substrates by exertion of the same shear force (60 rpm for 10 min) on captured cells. Lamellipodia were more frequently observed in NP120 and NP200 cases (Figure 4-6(f) and (g)) where the total adhesion force between the substrate and cell is relatively large, while filopodia

were dominant in NP500 and NP1100 cases (Figure 4-6(h) and (i)) where adhesion force is relatively small. Based on these results, we speculated that the final formation of either lamellipodia or filopodia depends on the relative strength of cell adhesion force and applied shear force. Under shear force, cells were inclined to roll on the substrate; the larger the shear force, the greater the effect until final detachment. In our case, during the eluting process these unwashed cells are inclined to form new adhesive bonds at the leading edge and dissociate old ones at the trailing edge [153]. If the adhesive force generated between the cell and substrate is much larger than the applied shear force (cells on NP120 and NP200 substrates; cells on planar surface washed by 60rpm), the flowing fluid just gently aligns cells in the flow direction, and cells have sufficient time to form lamellipodia. In comparison, attached cells with less adhesion force in NP500 and NP1100 cases or suffering large shear force on planar surface are more susceptible and easier to roll on the surface. These cells develop filopodia during such dynamics, which is in agreement with a previous study showing that filopodia primarily acted as the traction force during spreading on a microstructured pattern [141]. It was also observed that the direction of the formation of lamellipodia and filopodia matched with the flow direction induced by shaking in Figure 4-6(b), indicating that lamellipodia and filopodia formed initially in the leading edge, which is in agreement with a previous study [154]. These findings indicate the possibility to control the formation of pseudopodia type and direction by applying shear force on attached cells.

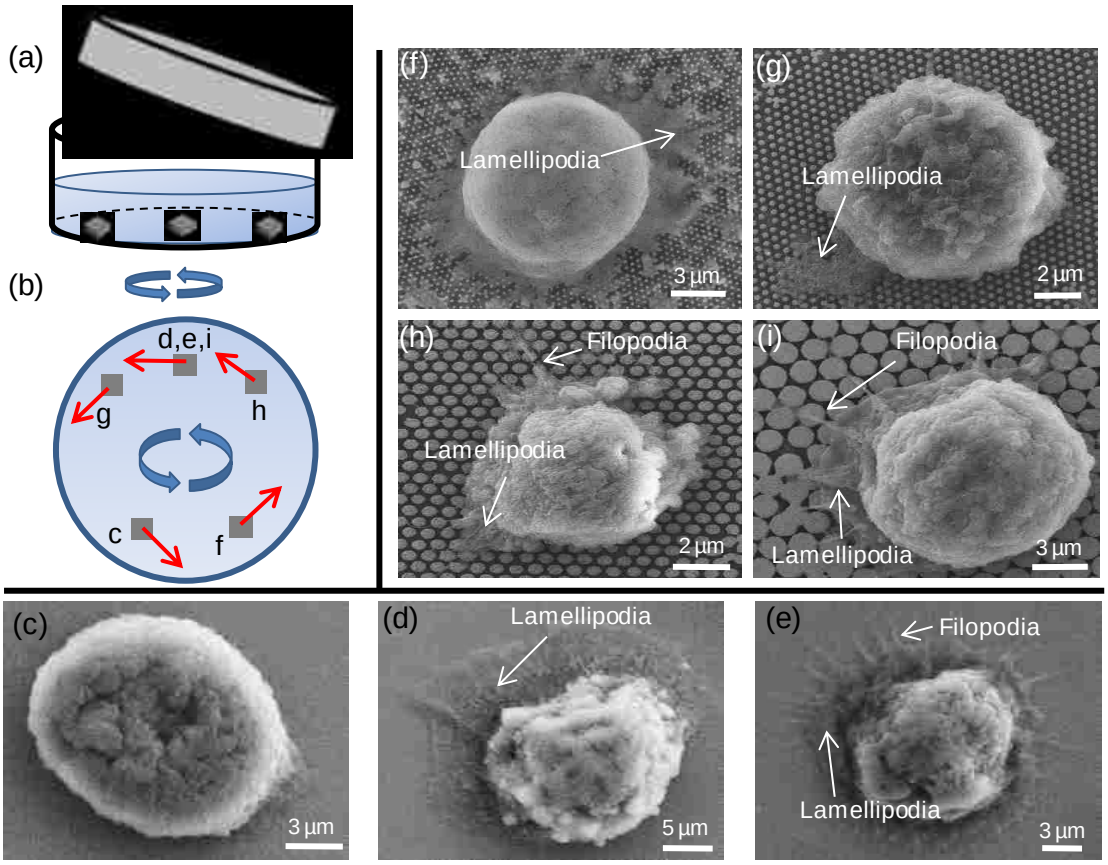

Figure 4-6 Schematics of experimental setup and SEM images showing the cell-NP interactions (lamellipodia and filopodia) for different NP substrates. (a) A schematic of the experimental setup during shaking. (b) shows the corresponding locations on wafer substrates for (c)-(i), with corresponding flow directions marked in red arrows. (c)-(e) show cell behaviors on planar wafers with shaking speeds of 0, 60 rpm and 400 rpm, respectively. (f)-(i) show cell behaviors in NP120, NP200, NP 550 and NP1100 with an average spacing of 140 nm, respectively. Typical lamellipodia and filopodia are annotated in each figure. Orientations of (c)-(i) have been adjusted to be the same as that in (b).

4.4 Conclusion

In summary, we found a linear relationship between capture yield and effective contact area of NP substrate with diameter ranging from 120 to 1100 nm. NPs with smaller diameter are preferred to achieve higher capture yield due to their large effective contact area. On the other hand, very small spacing below 100 nm (typically size of

microvilli) significantly impairs the capture yield. The effect of shear force on cell behaviors on an NP substrate was also studied for the first time. We found that the formation of filopodia or lamellipodia depends on the adhesion status of the captured cell, eluting strength and its direction. These findings provide guidance on the design of NP geometry for efficient CTC isolation, and possibilities to tune cytomorphology by manipulating shear forces.

Chapter 5: Hierarchical Micro-/Nanostructured CTC Chip

5.1 Introduction

Tumor is among the leading causes of deaths over the world. Tumor detection especially in the early stage is of great interest to both researchers and clinicians. Traditionally imaging techniques like MRI were mainly used to guide doctors to suspect a cancer occurrence while the cancer confirmation was still in need of an invasive biopsy [155]. However, the discomfort and a higher risk of infections brought by most invasive biopsies lays a hurdle for a general acceptance. Recently, liquid biopsy due to its intrinsic property of non-invasive attracts lots of attention and emerges as an appealing approach to diagnose cancers. A few biomarkers in blood have been recognized to detect cancers [156-159] such as circulating tumor cells (CTCs), which are the tumor cells originated from the primary tumor and circulating in the blood vessel during metastasis. Recent studies have revealed its clinical relevance in regards of both early cancer detection [47] and cancer prognosis [160-161], which directly correlates to the amount of CTCs per mL blood. However, the challenge to detect CTCs lies in its rarity, i.e. 1-100 per 1 mL blood vs. millions or billions of other normal blood cells. Various techniques have been developed to overcome the challenge. Currently, the detection techniques can be divided into two categories: physical property (e.g. size [162-163], dielectricity [37, 164] and deformability [165-166]) based and immunoaffinity (i.e. various antigen-antibody bonds [34-35, 86]) based approaches. Among the immunoaffinity based approaches, there exist

two categories based on the targeting cells, i.e. positive isolation [34-35] which targets at CTCs and negative isolation which depletes [167-168] white blood cells (WBCs). Although promising results with high capture efficiency have been achieved in various platforms [34-35, 55], it is still in need of a platform which can achieve both high capture efficiency and purity, which reflects the specificity among the isolated cell pool.

The emerging techniques of microfabrication and nanofabrication allow for a possibility to design various smart structures to enhance these device performance. A hallmark microfluidic device with grooved herringbone (HB) structures, initially proposed by Stroock *et al.* [56], was developed to efficiency isolate CTCs with a capture efficiency up to 93% and a purity of 14%. This HB design was mainly designed in use of stretched and disturbed flow streamlines which thus increase cell-surface interactions. Various derivatives of the HB chip [55, 78] were also developed but with similar grooved-HB structures. However, one main limitation on the grooved-HB chip lies in the extremely low shear rate regions in the groove troughs where WBCs are also readily trapped, thus might sacrificing the purity performance. To overcome this challenge, our group has recently developed a wavy-HB chip which smoothes the sharp groove structures thus eliminating the extremely low shear rate regions. The wavy-HB chips showed a capture efficiency up to 85% and a purity up to 39.4%. To further improve the device performance, various strategies have been proposed in literature by integrating nanostructures, which enhance the cell-surface interactions by increasing overall surface areas. For example, Tseng's group developed a few microfluidic chips which combine the herringbone microstructures with various nanostructures including nanopillars [54] and nanovelcro structures [59]. These hierarchical micro/nanostructures presented a better

capture efficiency of ~ 87% and their clinical utilities were also demonstrated on patients of various cancer phenotypes [59-60, 95]. Furthermore, the integration of nanopillars can be optimized following a design guide unraveled in our previous work [68], which suggested nanopillars with a diameter of 100 nm were preferred for enhanced CTC capture due to their large effective surface contact area.

In this study, a CTC chip with micro wavy-HB structures coated with nanoparticles (NPs) was developed with a high capture efficiency up to ~98% and a low non-specific capture of WBCs of ~680/mL blood. This hierarchical structures reflect combinative advantages from both microscale and nanoscale: by constructing the micro wavy-HB structures, the chip preserves a high purity by eliminating the extremely low-shear regions; by integrating NP nanostructures, the chip presents a high capture efficiency due to both HB induced vortex effect and NP induced enhanced cell-surface interactions. As follows, the working mechanism of the microfluidic chip was first described. Then, the fabrication approach was introduced to integrate micro wavy-HB structures and NPs followed by an SEM characterization. Finally, the tumor cell capture test was performed on the developed CTC chip and results were compared with other designs in literature.

5.2 Method and Materials

5.2.1 Fabrication and Surface Functionalization of the Hierarchical CTC Chip

The hierarchical micro/nanostructured microfluidic chip was fabricated in two steps. First, a PMDS slab with micron wavy-HB structures was made by using the

previously developed reflow process [54]. Briefly, an SU8 master with traditional grooved-HB was first fabricated, followed by a replication of PDMS molds. A second SU8 master was then replicated by pressing the PDMS mold on an uncured photoresist layer. After removing the PDMS mold, the sharp grooved-HB structures were melted into wavy-HB structures by increasing the temperature. The fabricated SU8 master was then silane treated and used for PDMS replications. Another PDMS cover layer was also made through the traditional photolithography method, followed by punching holes for the inlet and outlet.

To deposit NPs on the wavy-HB structures, a layer-by-layer deposition approach was developed which utilized the electrostatic interaction between oppositely charged polymers[169], as shown in Figure 5-1. First, negative charges were introduced to the surface of the above-mentioned PDMS slab with wavy-HB structures by a plasma treatment. The PDMS slab was then immersed in a 0.01 mol/L Polyarylamine hydrochloride (PAH) solution for 5 mins to form a layer of positively charged polymers followed by a rinse with DI water. Negatively charged silica NPs with a diameter of 100 nm were deposited by immersing the PDMS slab in 1% NP solution in ethanol for 5 s. To control the deposition consistency for each deposition, an automated manipulator was used to fix the pulling velocity at 5 mm/min [170]. The deposited PDMS slab was dried overnight under an enclosed environment of ethanol to reduce the evaporation induced convection effect, which could lead to a non-uniform particle coating [171-172]. The micro/nanostructures were then characterized by SEM scanning. Lastly, the hierarchical micro/nanostructured PDMS slab was assembled with the PDMS cover layer to make a microfluidic chip.

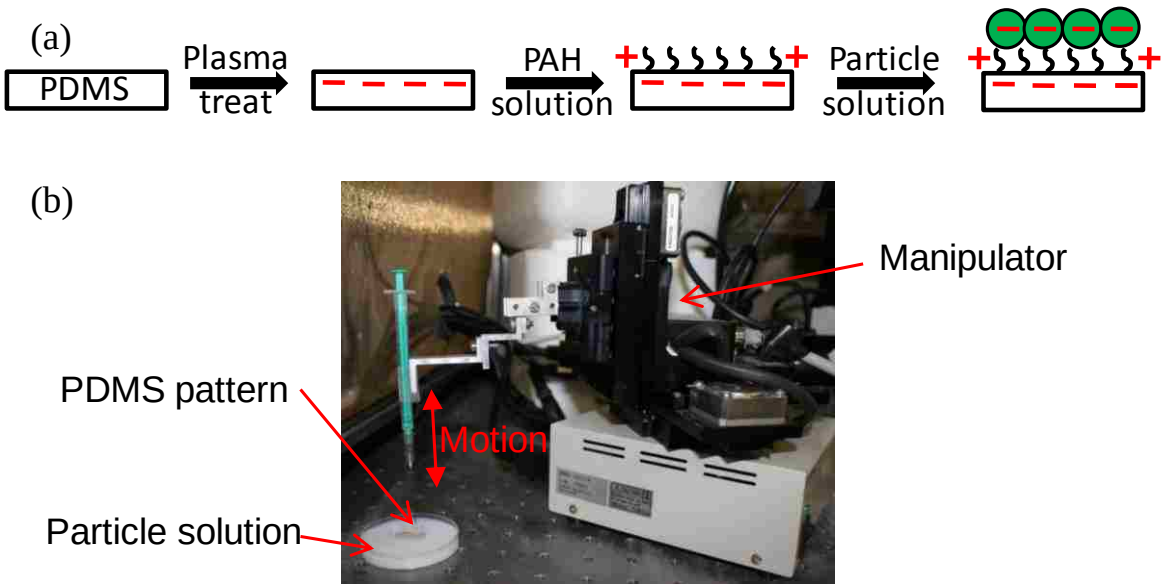

Figure 5-1 (a) The flow chart of NP deposition on the wavy-HB PDMS device. (b) The experimental setting for NP deposition. The PDMS device moves up and down following the needle which is controlled by the manipulator.

For cancer cell capture test, microfludic chips were chemically functionalized with anti-EpCAM following a standard protocol [54]. Briefly, 3-mercaptopropyl trimethoxysilane (MPTS) was covalently linked with the hydroxyl group on the PDMS surface induced by plasma treatment. N-y-maleimidobutyryloxysuccinimide ester (GMBS) was then connected with MPTS, followed by a coating of NeutrAvidin. Within 4 hrs of cell capture test, biotinylated anti-EpCAM was introduced to the microfluidic device. Regions uncovered with anti-EpCAM were blocked with BSA molecules which resist non-specific cell captures.

5.2.2 Cell Sample Preparation and Capture Test

In this study, HCT-116 cells were used to model CTC performances for patients with colon cancer. Cells were cultured following a standard protocol by routinely

changing fresh cell medium comprised of Dulbecco's Modified Eagle's Medium, 1% penicillin/streptomycin antibiotics and 10% fetal bovine serum. Upon their confluency of 70-80%, cells were diluted 10^3-10^5 /mL in either 4 mg/mL alginated PBS buffer solution or healthy whole blood purchased from Innovative Research.

Cell solution was injected into microfluidic chips at prescribed flow rates ranging from 580 μL/hr to 3600 μL/hr, which covers the widely used range in literature [35, 76]. PBS buffer solution was injected right after cell capture test to remove all suspended cells, followed by a fixation process by 4% paraformaldehyde. To further fluorescently identify captured cells, cells were treated with 0.2% Triton X-100 and further stained with a cocktail solution of DAPI, anti-cytokeratin FITC and CD45 PE. Cells which were DPAI positive, cytokeratin positive and CD45 negative were treated as tumor cells, while cells which were DAPI positive, cytokeratin negative and CD45 positive were treated as WBCs. Meanwhile, only cells with morphology integrity were counted.

To identify cell viability, a cocktail solution containing calcein-AM and ethidium homodimer (EthD-1) was used to perform a LIVE/DEAD assay. Cells were treated as viable if they were calcein-AM positive and EthD-1 negative, while all others were treated as dead.

5.3 Results and Discussions

5.3.1 Working Mechanism

Deriving from the wavy-HB chip developed earlier by our group [54], the hierarchical CTC chip mainly improves the device performance by depositing NPs on the wavy-HB pattern, as shown in Figure 5-2(a). As a proof-of-concept study, the geometry

of the wavy-HB pattern was designed as the same in the previous work [35], where wavelength is 160 μm, wave amplitude is 22.5 μm, short/long arms are 100 μm/200 μm, intersection angle of short/long arm is 90° and channel height is 50 μm. Based on the geometry guide of nanostructures to optimize cancer cell capture [68], NPs with a diameter of 100 nm were used.

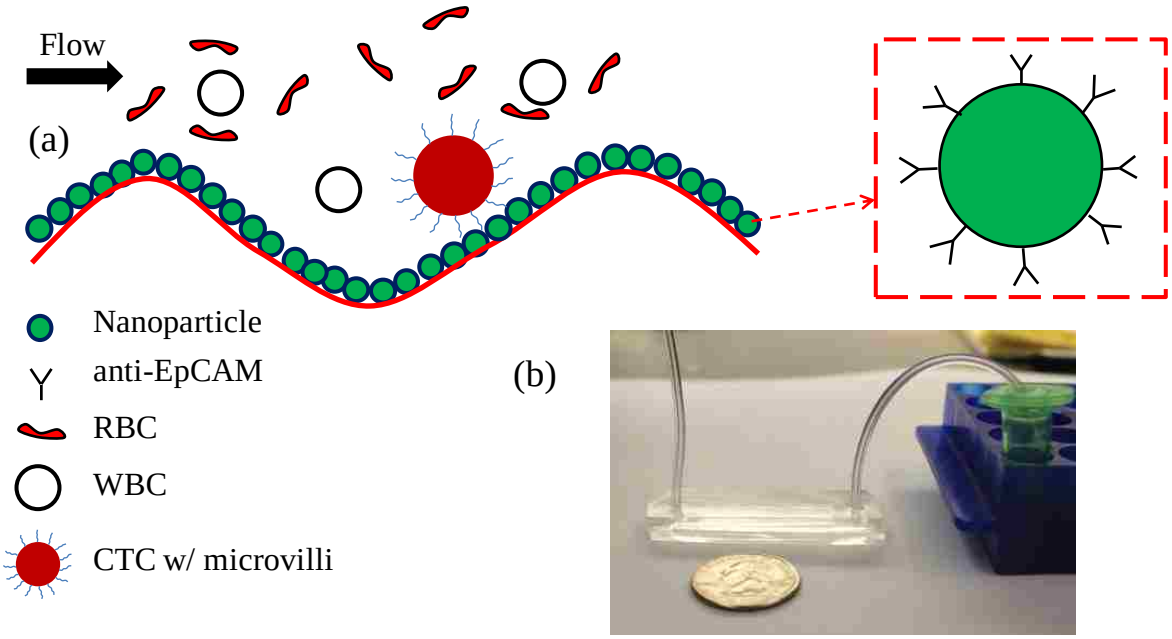

Figure 5-2 (a) Concept illustration of cancer cell capture in a microfluid chip with hierarchical micro/nanostructures. NPs coated with anti-EpCAM are deposited on the wavy-HB pattern. (b) Photographic image of the test setting for the hierarchical CTC capture chip.

From both numerical and experimental point of view, high capture efficiency can be achieved based on the wavy-HB pattern, which was demonstrated to induce significant vortex effect and own enlarged cell-surface contact area. Since the NPs have a diameter of 100 nm which is around 1/500 of the micropattern, the NP existence rarely influences the flow domain. Furthermore, the integration of NPs allows for an increase of cell-surface interaction area due to the large surface-to-volume ratio for NPs. Assuming a

monolayer of NPs of 100 nm diameter are formed over the wavy-HB pattern, a 2-fold increase of surface area is achieved on the nanostructured surface. The increased surface area thus enhances cell-surface interactions and cell capture. On the other aspect, high purity can be achieved based on the smooth wavy pattern, which was demonstrated to eliminate the extremely low shear rate regions. The increased surface area rarely leads to an increased amount of WBCs as the non-specific areas are blocked by BSA buffer solution.

5.3.2 Characterization of Hierarchical Micro/nanostructures

As shown in Figure 5-2(a), the PDMS slab needs to be dried after withdrawing it from the particle solution. It was noticed that if directly exposed in air and dried overnight, NPs were always distributed non-uniformly with more in the top ridge and less in the bottom trough as shown in Figure 5-3(a) and (b). This was explained by the fact that the thin fluid film underwent a convection flow induced by evaporation which brought NPs from the trough to the ridge [171-172]. In other words, the ethanol film evaporated fast in the ridge as it was thin compared to that in the bottom. As a result, it triggered a convection flow with NPs from the trough to the ridge. To reduce this effect, the PDMS slab was dried in a petri dish containing a small amount of ethanol solution, as shown in Figure 5-4(a-b). Although it increased the time for the drying process, the vapors from the ethanol pool sustained a humidity which reduced the above-mentioned evaporation induced convection effect. It thus formed a relatively more uniform coating of NPs over the whole wavy-HB pattern, as shown in Figure 5-4(c-d).

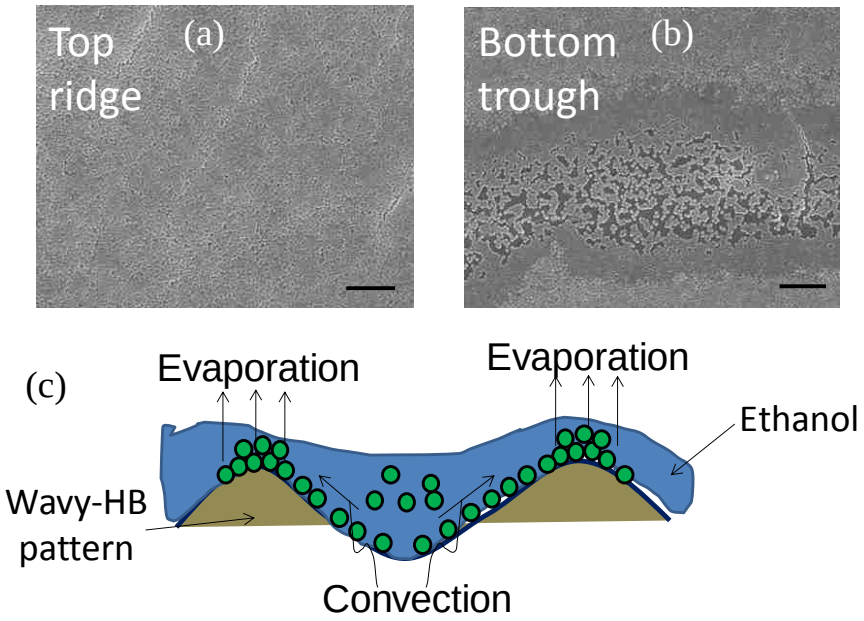

Figure 5-3 SEM images of deposited NPs on (a) top ridge and (b) bottom trough after the deposition process. (c) Illustrative image of the NP convection induced by ethanol evaporation if exposed directly to air. More particles are thus deposited on the top ridge and less particles on bottom trough. Scale bar: 2 μm.

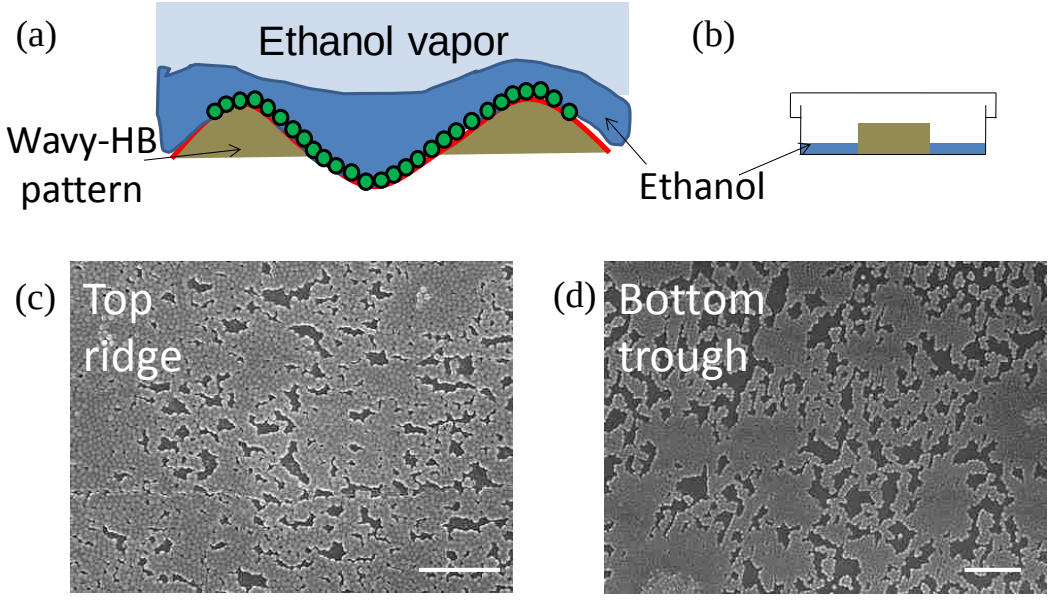

Figure 5-4 (a) Illustrative image of the NP deposition under the (b) improved evaporation setting. SEM images of deposited NPs on (c) top ridge and (d) bottom trough after the deposition process.

5.3.3 Cancer Cell Capture Test

To evaluate the device performance, HCT-116 cancer cells were spiked into both PBS buffer solution and healthy whole blood. After the cell capture test, a standard fluorescent staining protocol was used to differentiate captured cancer cells and WBCs, which were then counted to calculate the capture efficiency and purity. Typical fluorescent images of captured cancer cells and WBCs are shown in Figure 5-5(a-d). Furthermore, it was also noticed that the hierarchical wavy-HB chip was able to capture both single cancer cells and cell-cell clusters, which were shown to be more correlated to cancer prognostics [161]. More cell-cell clusters were observed to be captured in the hierarchical wavy-HB chip compared to the pure wavy-HB chip (data not shown).

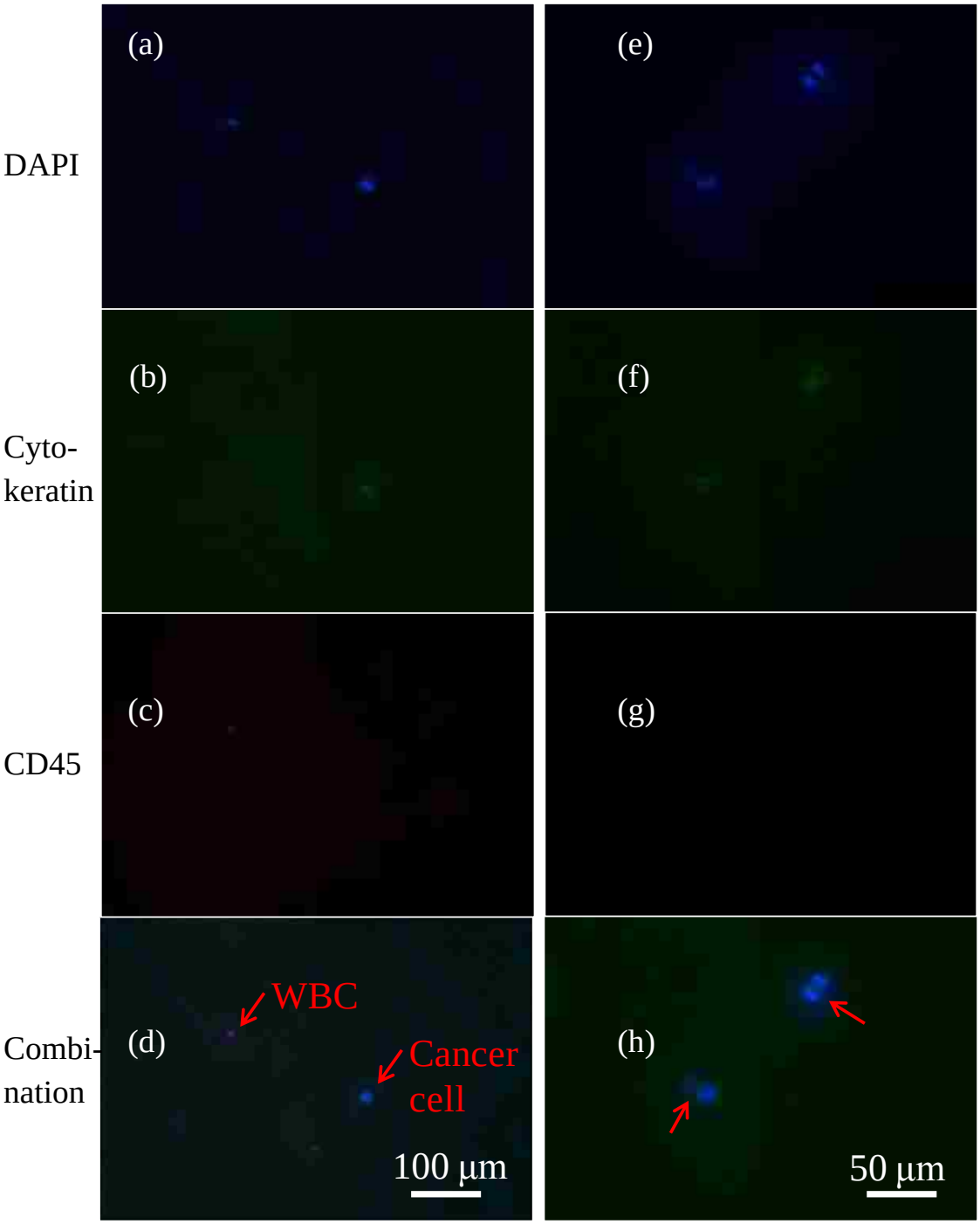

Figure 5-5 (a)-(d) Fluorescent images of a single cancer cell and a single WBC by using a cocktail solution containing DAPI, Cytokeratin-FITC and CD45-PE. (e)-(h) Fluorescent images of a single cancer cell and a two-cancer cell cluster by using the same cocktail solution.

Capture efficiency of cancer cells in the hierarchical wavy-HB chip was compared to that in the pure wavy-HB chip, the grooved-HB chip and the flat chip, as shown in Figure 5-6(a). The overall trend of capture efficiency over shear rate in the hierarchical wavy-HB chip agrees well with that for both grooved-HB chip and pure wavy-HB chip, which is mainly due to the increased shear detachment force at high shear rate. However, it was noticed that the hierarchical wavy-HB chip outweighs other two kinds of microfluidic chips in capture efficiency. Especially at higher shear rate, i.e. 400/s, the enhancement reaches up to around 2 times (77.18% vs. ~30%). This enhancement was speculated from the increased total surface area brought by the integration of NPs, which agrees well with the findings in other works in literature [90, 173]. Interestingly, Figure 5-6(b) shows that the amount of non-specifically captured WBCs was similar between the pure wavy-HB chip and the hierarchical wavy-HB chip, which suggests that the integration of NPs does not lead to more non-specific WBC capture. Although the exact mechanism was not known yet, this consistent purity performance was speculated due to the fact that the non-specific bond force was smaller than the flow detachment force over the whole flow domain in both chips which eventually yielded a similar performance on WBC capture. Based on results shown in Figure 5-6(a-b), the hierarchical wavy-HB chip can lead to best capture efficiency among these chips. Meanwhile, if post-analysis like DNA analysis is needed where both high capture efficiency and high purity are required, the hierarchical wavy-HB chip can serve as a suitable candidate to be tested at high shear rates like 200/s and 400/s.

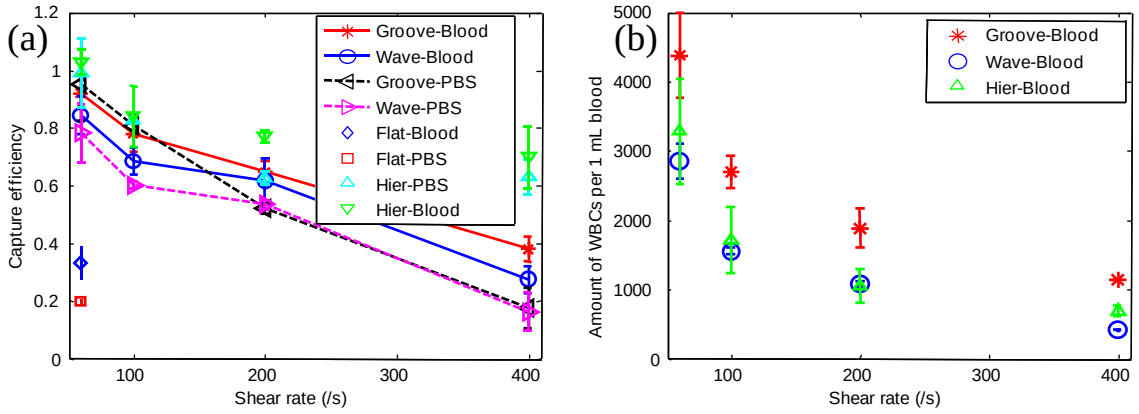

Figure 5-6 (a) Capture efficiency vs. shear rate in different devices in both PBS buffer solution and blood. (b) Amount of non-specifically captured WBCs in 1 mL blood in different devices at different shear rates.

Figure 5-7(a) shows a typical microscopic image of captured cancer cells in the hierarchical wavy-HB chip. Furthermore, SEM images were taken to reveal the details including cell morphologies and cell-surface interactions, as shown in Figure 5-7(b-c). These images again confirm that NPs sustained on the wavy-HB pattern after cell capture test. The apparent contact area was calculated to be around 101.7 μm^2. By comparing it to that in our previous study [68] where cells were incubated for one hour, it is similar to the value (~110 μm^2) where cancer cells spread on the bare wafer surface and smaller than that (~280 μm^2) on the 120 nm NP arrays. But it is with expectation since the one-hour incubation allows cancer cells to spread over the substrate while in this study, cancer cells were fixed right after the cancer cell flow test. With the increased effective contact area due to the NPs, cancer cells were able to be captured more effectively compared to the bare wavy-HB surface.

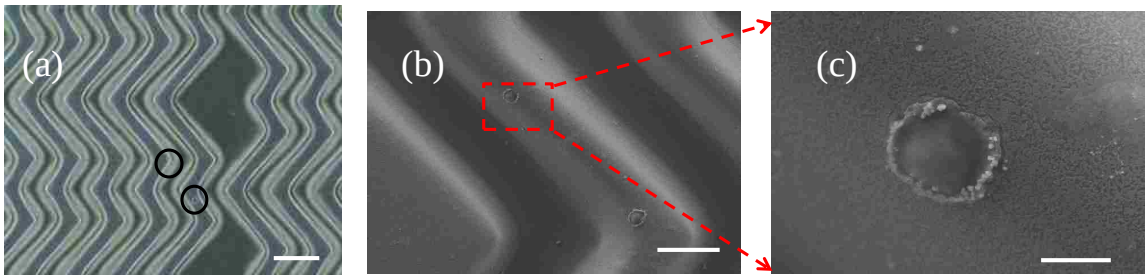

Figure 5-7 (a) Microscopic image of captured cancer cells on the hierarchical wavy-HB pattern. Scale bar: 160 μm. (b) SEM image of captured cancer cells on the pattern. Scale bar: 50 μm. (c) The zoom-in image reveals details of the interaction between a cancer cell and the NPs covered wavy pattern. Scale bar: 8 μm.

Another facile approach to fabricate hierarchical micro/nanostructures was also developed and tested in both flat channel and wavy-HB chip. The working mechanism was based on hydrophobic forces between two hydrophobic molecule groups. In detail, the PDMS surface after plasma treatment could recover to the hydrophobic condition if exposed to air for 24 hours. Meanwhile, the streptavidin coated magnetic microparticles used in this work are also hydrophobic due to the hydrophobic streptavidin molecules. As a result, after the injection of these microparticles through microfluidic chips, microparticles were subjected to adhesion over the whole PDMS surface due to the hydrophobic forces. As a proof-of-concept study, the particle coating performances were examined in both flat channel and wavy-HB chip in Figure 5-8(a) and (b), respectively. After PBS buffer flushing at 400/s, all particles were preserved which suggests that this is a facile and robust approach to deposit particles to form hierarchical micro/nanostructures. Furthermore, particle concentration could be adjusted to tune the coating density (data not shown here).

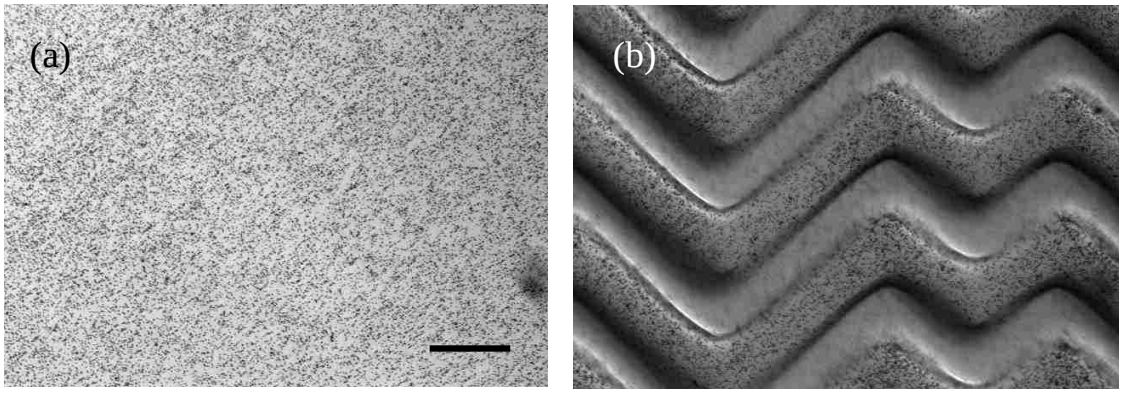

Figure 5-8 Particle deposition after a single flush of streptavidin coated magnetic microparticles in (a) a flat channel and (b) a wavy-HB chip to form a hierarchical micro/nanostructures. Scale bar: 100 μm.

5.4 Conclusion

A microfluidic CTC isolation chip with hierarchical micro/nanostructures were developed. By extending the concept of previously developed wavy-HB chip, the integration of nanoparticles enhanced CTC capture due to the increased overall surface area. A previously developed particle deposition approach was used to fabricate the hierarchical patterns. In comparison to the pure wavy-HB chip and the hallmark grooved-HB chip, the wavy-HB chip with hierarchical micro/nanostructures demonstrated a capture efficiency up to almost 100% at low shear rate (i.e. 60/s) and a high purity performance (only ~680 WBCs per 1 mL blood). SEM images were also used to further characterize the interaction between captured cancer cells and micro/nanostructures. Lastly, a facile approach was introduced to deposit micro/nanoparticles on the wavy-HB pattern and the feasibility was validated through a SEM characterization.

Chapter 6: Cancer Cell Capture and Release Assisted by Magnetic Particles in Hierarchical Wavy-HB Microfluidic Devices

6.1 Introduction

Circulating tumor cells (CTCs) are originated from the primary tumor site and circulate over the course of metastasis. CTCs were among the several general cancer biomarkers which could be used for cancer detections [47] and cancer prognostics [160-161]. Various techniques were thus developed to isolate CTCs in recent decades, which were categorized into either positive CTC isolation [35, 54, 59] or negative leukocytes depletion [167-168]. In other words, these techniques were either based on physical property differences or immunoaffinity differences between CTCs and normal blood cells including both red blood cells (RBCs) and white blood cells (WBCs). For example, based on the fact that CTCs uniquely express epithelial cell adhesion molecules (EpCAM), Toner's group developed a few microfluidic chips coated with corresponding antibody, i.e. anti-EpCAM, to capture CTCs [34-35]. The device performance was examined on various cancer types and demonstrated with a high capture efficiency of ~85%, which was essential for further clinical utility [174-175]. In these approaches, CTCs captured in the microfluidic chip were subjected to fluorescent staining and then imaged/counted through microscopic analysis. Besides the in-situ CTC analysis, there was a need for isolated CTCs to be collected and re-cultured which allows for further drug screening and

treatment guidance [55, 92, 176]. This in turn required isolated CTCs to be released from the capture bed. A few attempts were made by implementing stimulated subjects such as aptamers [86, 177] and thermo/PH-responsive materials [178-179]. An alternative which was currently widely studied was to use magnetophoresis to isolate either CTCs or WBCs labeled with corresponding immunomagnetic particles [180-183].

Toner's group developed a CTC-iChip which first depleted RBCs based on deterministic lateral displacement and then negatively extracted all WBCs labeled with immunomagnetic particles by applying a magnetic field [181]. Similarly, Liu *et al.* [184] developed a microfluidic chip embedded with nickel micropillars, which positively isolated CTCs labeled with anti-EpCAM coated magnetic particles under a magnetic field. Although these techniques advanced CTC post-analysis, further improvements mainly lie in a development of a platform with high capture efficiency, high release efficiency and easy fabrication/operation modality. Our group previously developed a microfluidic chip with hierarchical micro/nanostructures for CTC capture with high capture efficiency and high purity [54, 68]: high capture efficiency was mainly attributed from the HB structures induced vortex effect and further enhanced by the nanostructures; high purity was achieved by smoothing the sharp grooved patterns into wavy patterns, thus eliminating the low-shear regions where WBCs were subjected to non-specific capture. Here, by extending this platform, instead of permanently depositing particles through immunoaffinity, anti-EpCAM coated magnetic particles were trapped over the untreated PDMS surface by external magnetic field and were then released by readily removing the magnet for CTC collection.

In the following content, the working mechanism of the magnetic particle assisted cancer cell capture and release was first introduced. Various magnets settings were examined to find out the optimized condition. As a proof-of-concept, flow cytometer analysis was used in this work to evaluate the device performance. Finally, captured cancer cells labeled with magnetic particles were collected and re-cultured in regular petri-dishes to demonstrate the capability for further drug screening.

6.2 Experimental Details

6.2.1 Working Mechanism

The whole process was divided into three steps: magnetic particle trapping, cancer cell capture and subsequent cell release. First, 5 μL Stock solution of super-paramagnetic particles coated with streptavidin with a diameter of 1 μm was mixed with 95 μL 10 μg/mL anti-EpCAM in BSA/PBS solution, followed by an incubation at RT for 2 hrs. This particle solution was then injected into the microfluidic chip at a flow rate of 3 mL/hr for 2 mins. After stand-by for 5 minutes, the microfluidic chip was incubated under the magnetic field for 2 minutes, which allows all magnetic particles to reach their stable conditions. With the magnetic sustained, a cancer cell capture flow test was performed, where all cancer cells were subjected to being captured on the anti-EpCAM coated magnetic particles and normal blood cells were flushed away, as shown in Figure 6-1(a). Wavy-HB microstructures were integrated into the microfluidic chip instead of a flat surface, which were demonstrated to ensure high capture efficiency and high purity in our earlier work [54]. Finally, to release captured cancer cells, the magnets were removed and a PBS flush at a flow rate of 3 mL/hr was applied to collect both individual magnetic particles and cancer cells labeled with magnetic particles, as shown in Figure 6-1(b).

Collected cancer cells were characterized either through a standard fluorescent imaging approach or flow cytometer analysis. Further post-analysis such as cell re-culture for drug screening could also be done. A typical experimental setting was also shown in Figure 6-1(c). The two spacers were used to fix the magnet-magnet distance for consistent experimental analysis, as well as to protect the microfluidic chip from deformation due to the strong magnet-magnet attraction force.

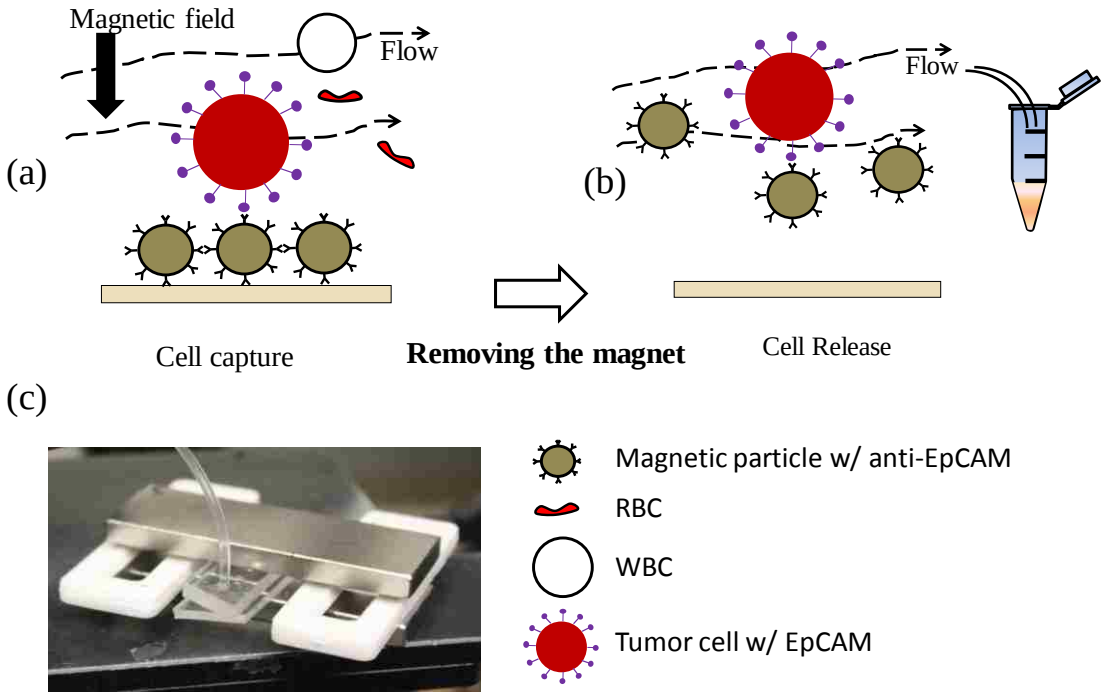

Figure 6-1 Illustration of working principles of magnetic particle assisted cancer cell capture and release. (a) Capture of cancer cells on the anti-EpCAM coated magnetic particles deposited on the surface under the magnetic field. (b) Release and collection of captured cancer cells and magnetic particles after the removal of the magnet. (c) Photographic image of a typical experimental setting of cancer cell capture under the magnetic field.

6.2.2 Microfluidic Chip Fabrication and Magnet Settings

The wavy-HB chip was fabricated and assembled following the reflow process introduced in our previous study [54]. Briefly, a PDMS slab with grooved-HB pattern

was first replicated from a corresponding silicon wafer. This PDMS slab was then used as a mold to replicate a SU8 master mold on another silicon wafer. Before curing the SU8, the SU8 groove patterns were melted to wavy patterns at a median high temperature, i.e. 65^{o}C. With this mold, PDMS slabs with wavy-HB patterns were replicated and assembled with another cover pattern. To avoid the non-specific binding of streptavidin coated magnetic particles on the PDMS surface, 3% BSA/PBS solution was injected and incubated for 30 mins to block the non-specific sites. Then anti-EpCAM modified magnetic particles were injected through the microfluidic chip and incubated under certain magnetic fields. To investigate magnetic particles' response on various magnetic fields, three magnet settings were considered: two parallel magnets crossing with the microfluidic chip, two parallel magnets parallel to the microfluidic chip and two magnets sandwiching the microfluidic chip, as illustrated in Figure 6-2(a-c). To be noted, the cubic magnets had the polar in the large area planes rather than the two thin ends, as marked in Figure 6-2(a-c).

6.2.3 Cancer Cell Culture, Flow Test and Re-culture

HCT-116 colorectal cancer cells were used in this study as model CTCs. HCT-116 cells were cultured in Dulbecco's Modified Eagle's Medium supplemented with 1% penicillin/streptomycin and 10% fetal bovine serum. Within one hour of cancer cell flow tests, HCT-116 cells were prepared upon their 70-80% confluency and its initial cell concentration was calculated by hemocytometer, followed by a dilution in either 4mg/mL alginated PBS solution or whole blood.

Cell solution was injected through the microfluidic chip at various shear rates ranging from 60 /s to 400 /s controlled by a syringe pump. After cell capture process,

magnets were removed and cancer cells were collected in a centrifuge tube by flushing PBS buffer solution at a flow rate of 3 mL/hr. To perform cell re-culture, collected cancer cells labeled with magnetic particle and individual magnetic particles were added to a cell culture flask. Meanwhile, cell culture medium was added to supply necessary nutrients. After 24 hrs' culture in the incubator, suspensions were removed, the flask was washed with PBS solution and refreshed with new cell culture medium. Then cancer cells were cultured following the regular protocol and monitored routinely.

A proof-of-concept flow cytometer analysis was performed on the collected cell samples. In this scenario, after cell capture process, cell membranes were permeabilized by 0.2% Trion X-100 and cytokeratin-FITC was used to specifically stain the cancer cells. Then all cells and magnetic particles were collected in a centrifuge tube and analyzed by BD FACSCanto II flow cytometer.

6.3 Results and Discussions

Magnetic particles' response under various magnetic fields were examined, as shown in Figure 6-2. It was found that different magnet settings lead to vastly different magnetic particle distributions over the microfluidic chip. Magnetic particles tended to form tails along the magnetic field. Specifically, under the magnetic setting as shown in Figure 6-2(a), magnetic particles formed tails parallel to the flow direction which is almost the same direction of the local magnetic field. Same phenomenon also happens to the magnetic setting in Figure 6-2(b). Under the magnet setting in Figure 6-2(c), magnetic particles were sparsely distributed and the magnetic field was vertical across the microfluidic chip. Furthermore, although most particles were able to sustain in the

microfluidic chip under PBS flushing at various shear rates up to 200/s, particles tails were subjected to being shifted towards specific focused regions, which were determined by the flow domain, as shown in Figure 6-2(j).

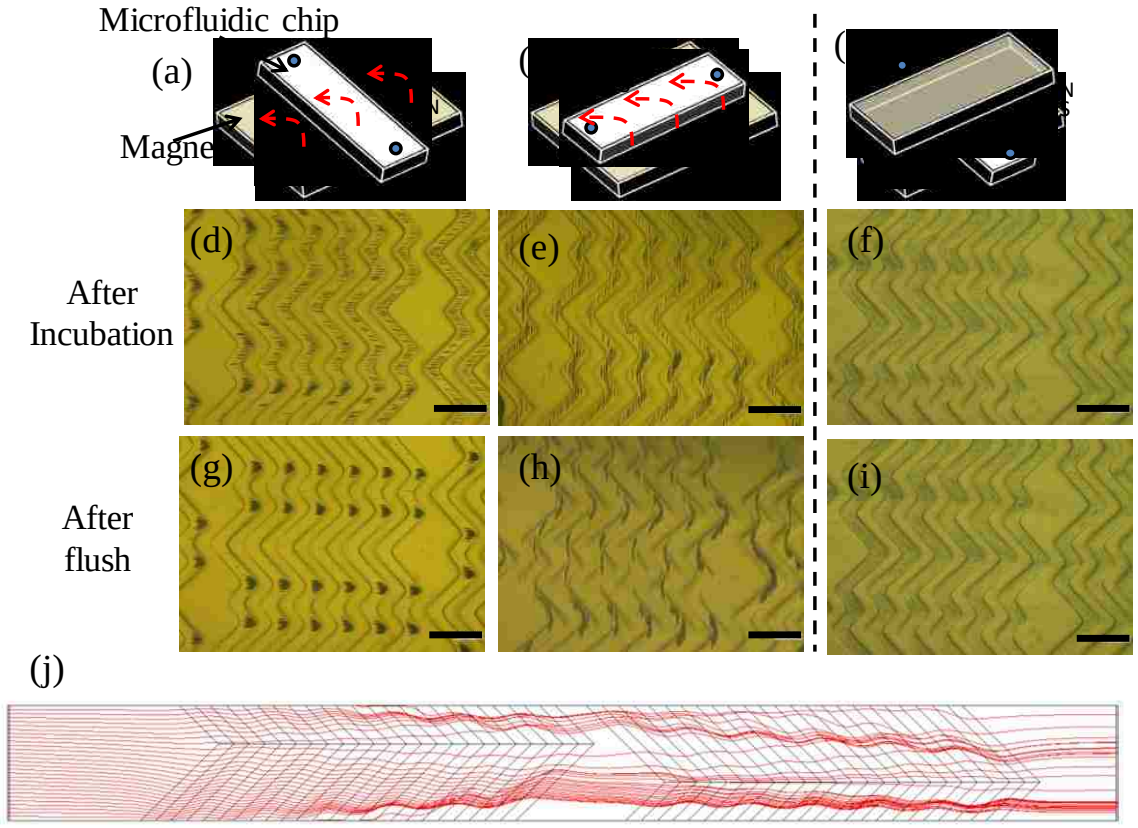

Figure 6-2 Various magnet settings and their corresponding magnetic particle response. (a)-(c) Three different magnet settings. (d-f) Response of magnetic particles under the magnetic field of (a-c) in 2 minutes, respectively. (g-i) Response of magnetic particles after PBS buffer flushing of 200/s under the magnetic field of (a-c), respectively. Scale bar: 250 μm. (j) Streamlines in a unit of wavy-HB patterns. Flow direction is from left to right.

Furthermore, the formation of tails was explained from the theoretical perspective which fundamentally lies in the dipole-dipole force induced by a pair of magnetic particles under the magnetic field. As shown in Figure 6-3(a), two magnetic particles were exposed to the magnetic field and each particle experienced a dipole-dipole force

exerted by the other particle. To the reactive magnetic particle as depicted in Figure 6-3(a), components of the magnetic force in the radial direction and tangential direction were calculated as follows [185],

$$F_r \approx -\frac{2\pi\chi^2 B^2 a^6}{3\mu_0 R^4}\left(1+3cos2\theta\right) \tag{6-1}$$

$$F_\theta \approx -\frac{4\pi\chi^2 B^2 a^6}{3\mu_0 R^4} sin2\theta \tag{6-2}$$

where χ is the magnetic susceptibility of the particle, B is the magnetic flux density, a is the radius of the particle, μ_0 is the permeability of space, R is the distance between two particles and θ is the intersection angle between the magnetic field and the particle-particle radial direction. Since in this study θ was the main factor to be examined, a simple normalization could be performed as follows,

$$\tilde{F}_r = \frac{3F_r\mu_0 R^4}{2\pi\chi^2 B^2 a^6} \approx -\left(1+3cos2\theta\right) \tag{6-3}$$

$$\tilde{F}_\theta = \frac{3F_\theta\mu_0 R^4}{4\pi\chi^2 B^2 a^6} \approx -sin2\theta \tag{6-4}$$

As shown in Figure 6-3(b), if θ is smaller than 45°, the reactive particle experiences an attractive magnetic force and a tail is thus formed; if θ is larger than 45°, the reactive particle experiences a repelling magnetic force and these two particles thus keep apart. On the other aspect, the reactive particle always experience a negative tangential magnetic force, which tries to pull the reactive particle to align in the magnetic field direction. The magnitude of this pulling force reaches a maximized value when θ is equal to 45°.

This magnetic dipole theory was able to explain the magnetic particle distribution in Figure 6-2(d-f) under different magnetic fields. Take magnetic setting in Figure 6-2(a) as an example. Before applying the magnetic field, all magnetic particles were uniformly distributed over the microfluidic chip. Under the magnetic field, following the theory explained above, each pairs of particles with a θ smaller than 45°, they were subjected to forming tails along the magnetic field direction; whereas each pairs of particles with a θ larger than 45°, they were kept apart. Upon their stable condition, tails were formed parallel to the magnetic particles, as shown in Figure 6-2(d). Figure 6-2(e) could be explained in the similar way. Slightly different from these two magnet settings, magnetic field direction approximately always were vertical to the plane of magnetic particles, i.e. θ was equal to 90°. In this condition, all particles experienced a repelling force which kept them apart.

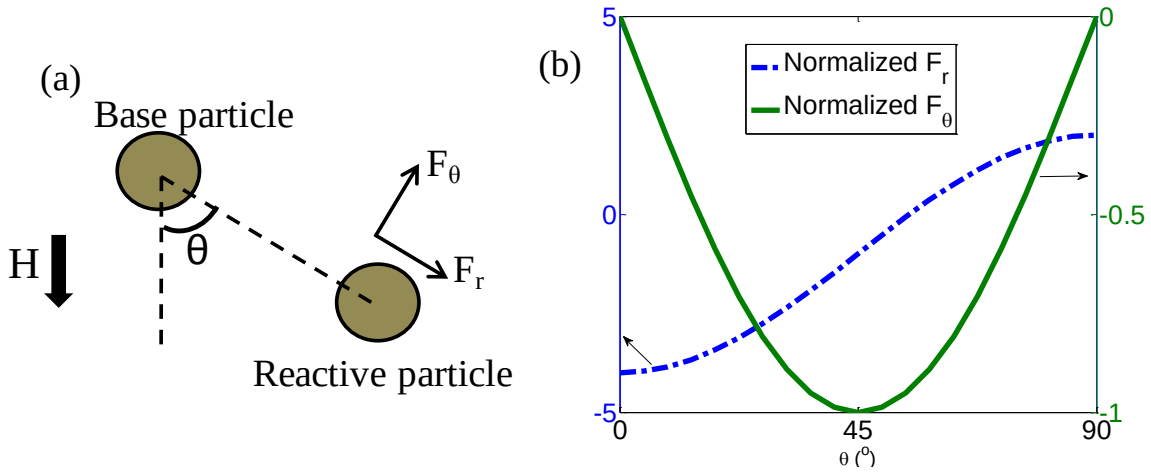

Figure 6-3 Theoretical analysis of dipole-dipole induced magnetic forces. (a) Illustrative image of two magnetic particles to form a dipole-dipole pair under the magnetic field. (b) Normalized magnetic forces in the radial and tangential directions in term of intersection angles.

To reach a uniform particle coating thus reaching maximized cell-surface interaction, the magnet setting in Figure 6-2(c) was used for the proof-of-concept study. Magnetic particles' response to the flow under the magnetic field was further investigated.

As shown in Figure 6-4(a-c), at the flow rate of 3600 mL/hr, magnetic particles exhibited different responses in different locations, with more particles sustained close to the edge of the magnets while less particles in the center section, as marked in Figure 6-4(e). This was mainly attributed to a competition between the external magnetic force (F_m) and the flow detachment force. The flow detachment force was similar in these three sections due to the similar flow field. However, F_m varied by following the governing equation as follows [71],

$$F_m = (\boldsymbol{m} \cdot \nabla)\boldsymbol{B} = \mu_0(\boldsymbol{m} \cdot \nabla)\boldsymbol{H} \tag{6-5}$$

where $\boldsymbol{m} = \frac{\chi_p}{1 + D_p \chi_p} V\boldsymbol{H}$ and $\boldsymbol{H}$ is the total magnetic field strength applied on the center of the magnetic particle, V is the volume of the magnetic particle, D_p is the demagnetization coefficient (D_p is equal to 1/3 for a sphere), χ_p is the susceptibility of magnetic particle.

The magnetic field contour was then studied through a COMSOL simulation as shown in Figure 6-4(f). The magnetic force on a magnetic particle along point A to point B, which mimics the location of the microfluidic chip, was then calculated following eqn. (*6-5*), as shown in Figure 6-4(d). It was found that components of magnetic force in both x and y directions reached the maximum close to the magnet edges, where most particles were sustained. Meanwhile, the magnetic force was extremely small even close to zero in the center section, where most particles were flushed away.

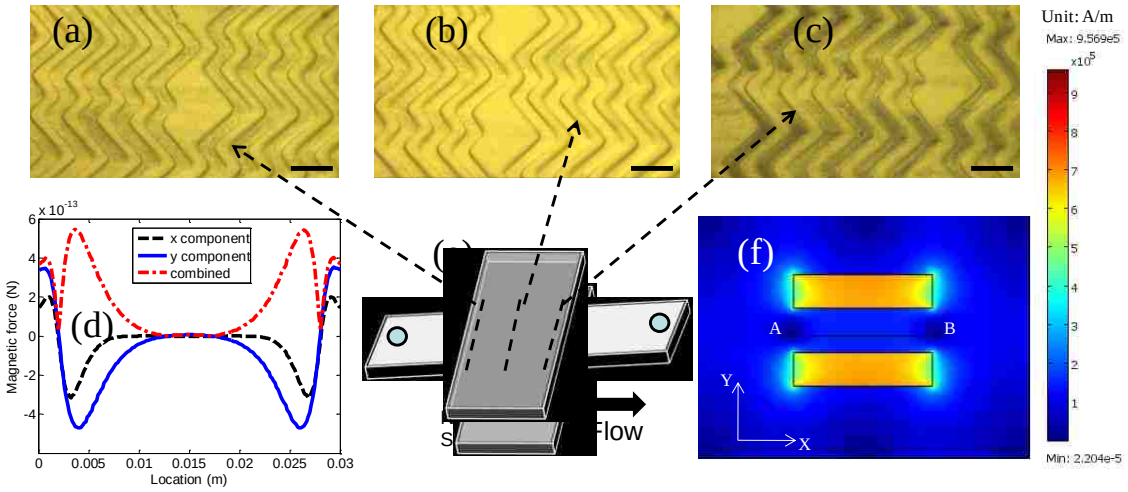

Figure 6-4 (a)-(c) Typical magnetic particle distributions under flushing of PBS buffer solution in three relative locations to the magnets in the setting of (e). Scale bar: 200 μm. (d) Magnetic forces from point A to point B in (f) which mimics the location of the microfluidic chip. (f) Contour of the magnetic field in the setting of (e).

Although a uniform particle coating was not achieved yet, a proof-of-concept work to demonstrate the concept of cancer cell capture and release was performed. A flow cytometer analysis was adopted to quantitatively characterize the collected samples. As shown in Figure 6-5(a-b), a control study was firstly performed to identify beads, cancer cells and other blood cells, which were determined by both size difference and fluorescence labeling. A cancer cell capture test was then performed. Since this was still a preliminary capture test work where the exact capture efficiency and purity was not studied yet, the feasibility of this approach was the focus of this work. From the results shown in Figure 6-5(c), cancer cells and beads were able to be counted through the flow cytometer analysis. Further study was planned to quantitatively investigate the performance of this approach.

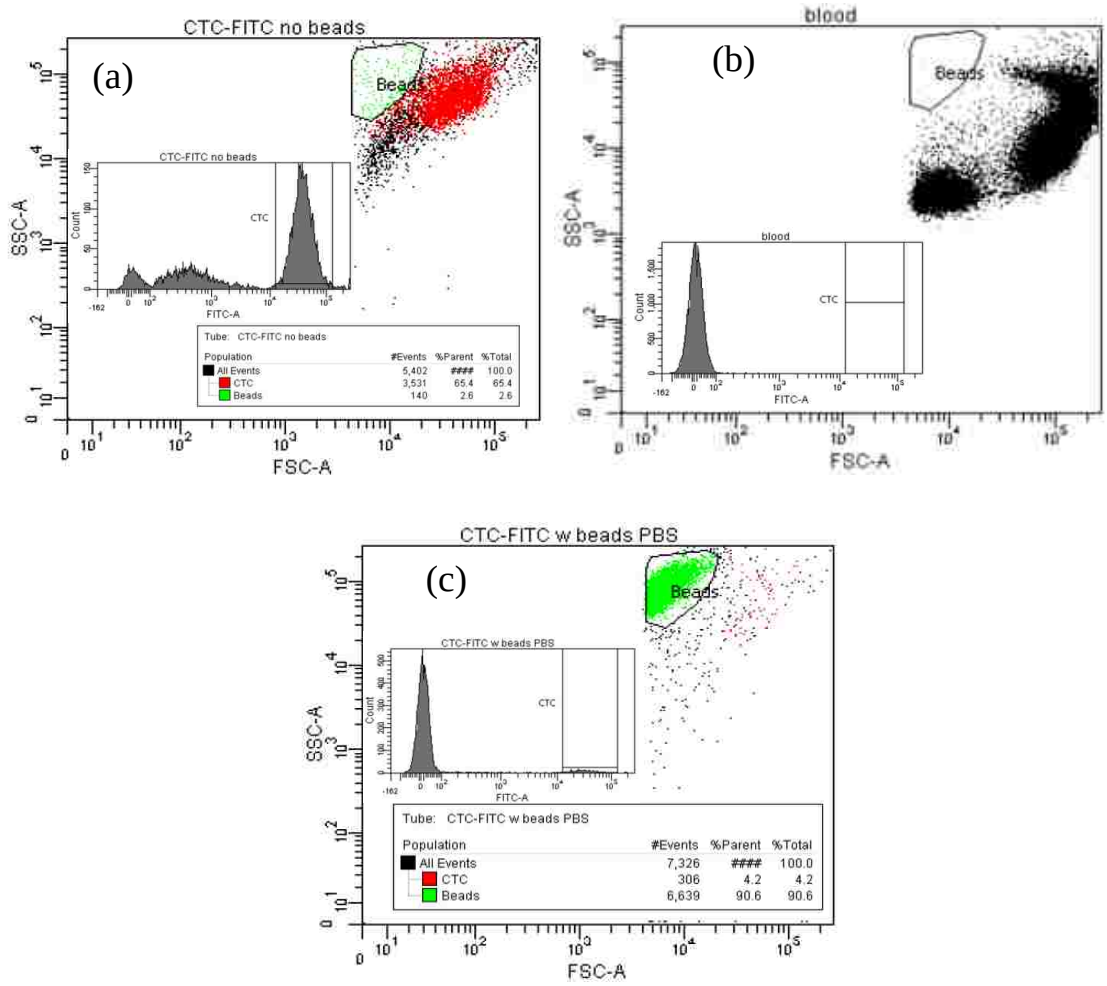

Figure 6-5 Flow cytometer analysis of collected samples: (a) Cancer cells stained with cytokeratin-FITC in PBS buffer solution; (b) Whole blood and (c) Cancer cells stained with cytokeratin-FITC mixed with anti-EpCAM coated magnetic particles. Here, (a) and (b) serve as control group to identify cancer cells. Data in (c) is the experimental result from capture and release of cancer cells assisted by coated magnetic particles.

The feasibility of re-culture of collected cancer cells was also investigated. The biofluidic sample containing both collected cancer cells and magnetic particles were cultured in a regular petri-dish. One day after the initial sample loading, both cancer cells and magnetic particles were settled down on the petri dish, as shown in Figure 6-6(a). Clearly, it was observed that cancer cells were labeled with multiple magnetic particles

even particle clusters. To observe the particle change over the course of cell proliferation, a series of microscopic images continuously recorded, from day 1 to day 4, and then from passage 0 to passage 2, as shown in Figure 6-6(b-d). Interestingly, it was found that magnetic particles gradually disappeared during cell proliferation. The exact mechanism was not unclear yet, and further study was still needed to reveal this mechanism.

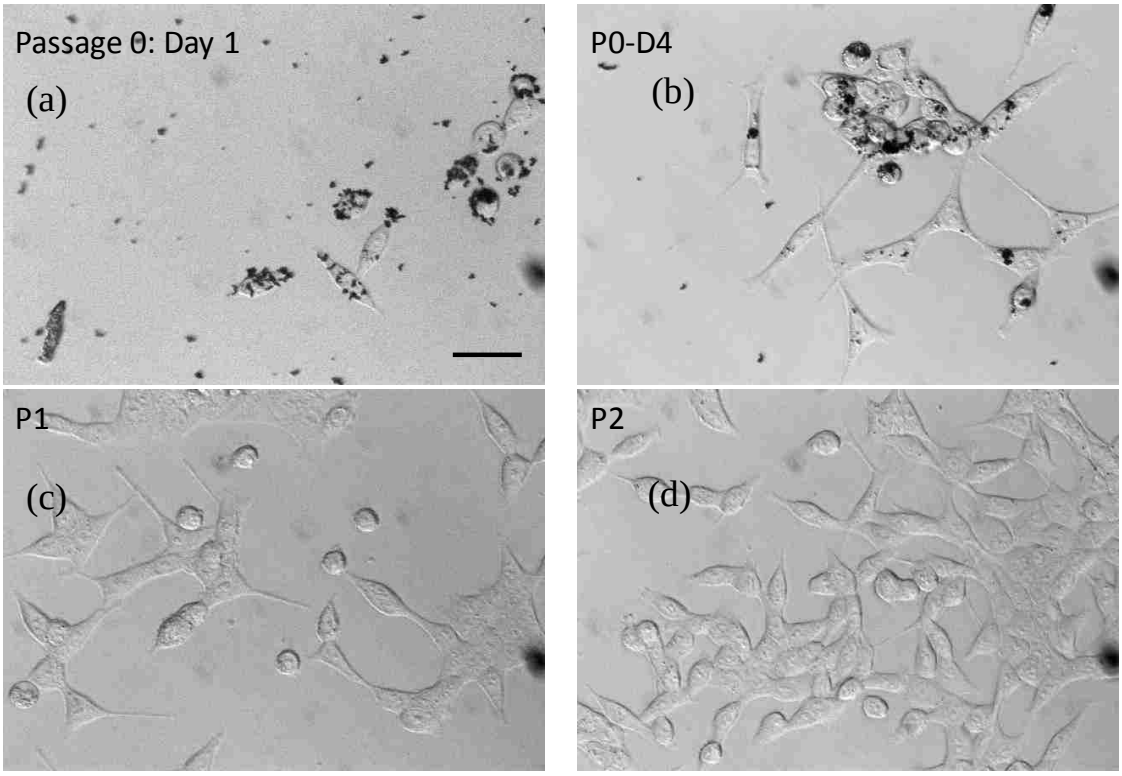

Figure 6-6 Re-culture of collected cancer cells linked with magnetic particles and individual magnetic particles. (a)-(b) Cell re-culture on Day 1 and Day 4 for Passage 0, respectively. (c)-(d) Cell re-culture for Passage 1 and Passage 2, respectively. Scale bar: 40 μm.

6.4 Conclusion

A microfluidic platform was developed to efficiently capture and release cancer cells by integrating a previously developed wavy-HB pattern and anti-EpCAM coated magnetic particles. In addition to the concept of magnetic particle assisted cancer cell

capture and release which were achieved by other platforms [180, 186], this platform was designed for achieving high capture efficiency and high purity which was brought by the wavy-HB pattern. A proof-of-concept study was performed to demonstrate its feasibility. Furthermore, to my knowledge, this was the first time to directly indicate magnetic particles were able to be self-removed during cell proliferation, which was very crucial for cancer cell post-analysis where any dirt should be eliminated. Further efforts will be put in a more comprehensive investigation of the performance of this approach, such as recovery rate and purity.

Chapter 7: Isolation of Rare Tumor Cells Using Adhesion Rolling in a Microfluidic Chip with Inclined Wavy Surfaces

7.1 Introduction

Circulating tumor cells (CTCs) were recognized as the origin of metastasis in many cancers. These cells are rare in the bloodstream, and, if isolated, can provide details on the diagnosis of non-hematologic and epithelial cancers, along with furthering research on metastatic cancers and their origins. The ultimate goal in this field is to isolate CTCs from normal blood cells with a high efficiency, high purity and high viability [187]. Various technologies were developed which fell into two main categories: Physical property based [37, 162, 165] and immuno-affinity based approaches [34, 54, 181]. Due to the complexity of cell biology, currently there is no definite method to achieve the above-mentioned goal yet. Most of the methods on the separation of CTCs from whole blood required complex blood processing [188] and usually require complex approaches to detach captured CTCs [55, 86], thus yielding a low viability [189]. As a result, there is an urgent need to develop a technique to isolate CTCs from blood samples in a convenient and reliable manner.

In literature, it was found that E-selectin was present on endothelial cells when chemotaxis of leukocytes (leukocyte migration) is needed [190]. The ligand-receptor attraction allows for the rolling of the leukocytes. This same interaction was noted with

tumor cells. The binding allows for metastasis of cancers. In a previous study, CTC rolling on E-selectin was compared to white blood cells (WBCs) [191]. The WBCs exhibited a stronger interaction with stable, more numerous bonds. Conversely, CTCs maintained a weak bond. By taking advantage of this adhesion force difference, I aimed to develop a novel microfluidic chip coated with E-selectin to isolate CTCs from normal blood cells. A smart geometry was designed with an inclined wavy pattern which first focused all cells towards one channel side due to the hydrophoretic flow effect [57, 192], and then guided CTCs and WBCs to different pathways due to different adhesion forces.

In the following contents, the working mechanism of the device was first discussed. Then our preliminary experimental results are used to support the proposed idea.

7.2 Methods

7.2.1 Working Mechanism

The overall strategy to isolate tumor cell from normal blood cells was described below: by designing a microfluidic chip with inclined wavy patterns coated with E-selectin, tumor cell spiked blood samples were injected through the chip and different cells either flow or roll along different pathways, as sketched in Figure 7-1(a) and explained in the following paragraphs. The experimental test system was shown in Figure 7-1(b). As a proof-of-concept work, RBCs were lysed so that isolation of only WBCs and CTCs were tested.

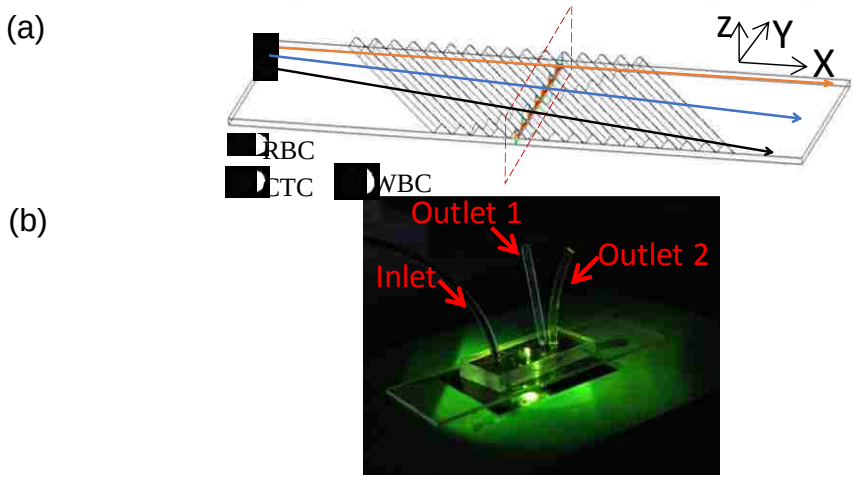

Figure 7-1 (a) Experimental setup for the tumor cell isolation. (b) The proposed concept of different cells flowing or rolling along different pathways.

To achieve the cell adhesive rolling based cell isolation mentioned above, the device performance was evaluated from two aspects. First, with the inclined wavy pattern, the flow presents velocity components in the cross-section as shown in Figure 7-2 (a). Due to the fluid mass conservation and the inclined wavy direction, a large looped flow pattern with a clockwise direction is formulated as shown in Figure 7-2(b). Regarding the forces exerted on flowing cells, cells experience same gravity force and buoyant force everywhere while drag forces exhibit different directions in different locations. With the fact that the density of both CTCs and WBCs is larger than that of the fluid medium, cells undergo an instable force balance and shift following the flow loop pattern, finally focusing at the interfaces where buoyant force and drag force balance with the gravity [57].

After cell focusing to one side of the channel, the subsequent cell isolation is achieve based on different adhesive force for CTCs and normal blood cells. As shown in Figure 7-2(c), it was found that RBCs have no interaction with the E-selectin coated

surface, thus following the straight flow stream. Both CTCs and WBCs perform adhesive rolling on E-selectin while stronger adhesion force exists for WBCs. In combination of the inclined wavy pattern which provides a guiding direction, it is expected that CTCs and WBCs will roll on E-selectin coated surface following different pathways.

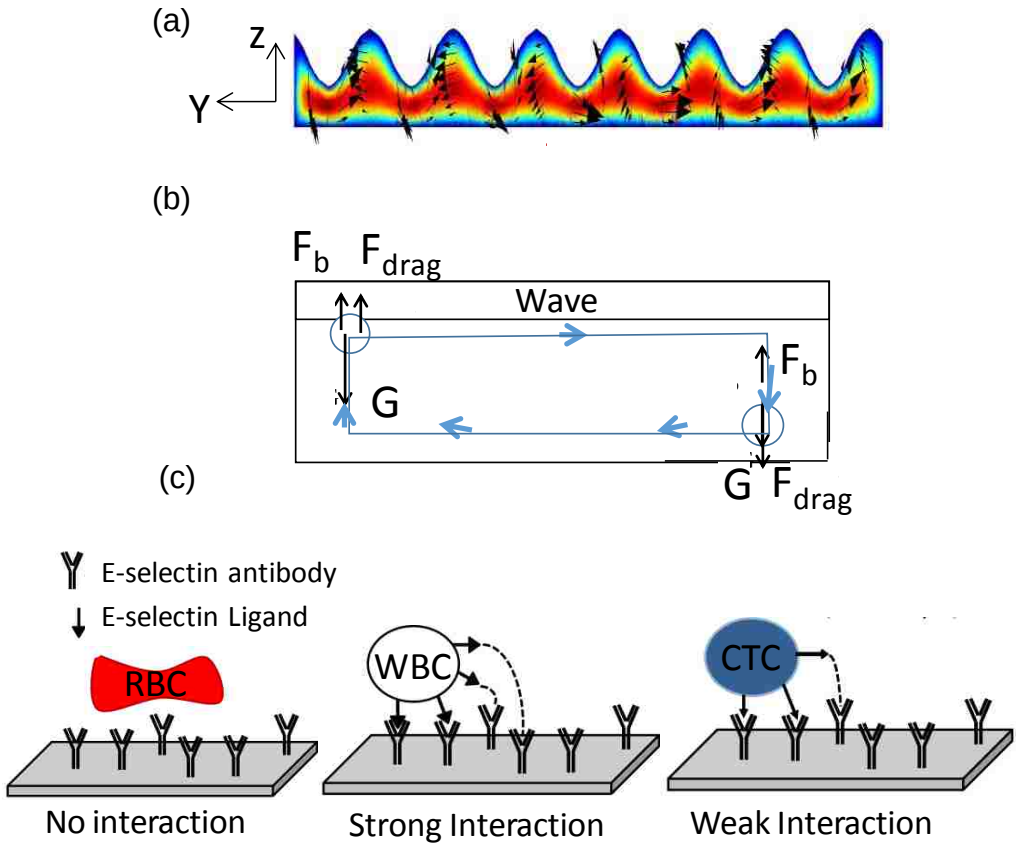

Figure 7-2 (a) The velocity contour in the cross-section of the Fig. 1(b). (b) A schematic image of the looped flow pattern and the forces on a flowing cell. (c) A schematic image indicates the interaction between cells and E-selectin coated surfaces.

7.2.2 Microfluidic Chip Fabrication and Surface Functionalization

A reflow approach was used to fabricate the inclined wavy pattern [54]. Briefly speaking, traditional grooved pattern was firstly fabricated as a master. After replicating

an uncured photoresist mold by the nano-imprint approach, the photoresist was melt to form waves at 65 ^{o}C. PDMS devices were then replicated based on this SU8 mold and assembled into a microfluidic chip.

A protocol was developed to coat E-selectin on the microfluidic chip referring to similar approaches [193-194]. Right after the assembly of the microfluidic chip, the device was incubated with 1% v/v APTES in ethanol for 30 minutes, followed by an enhancement in 100 degrees for 10 minutes. Then the device was modified with 10 μg/mL of recombinant protein G in PBS, which was then linked with E selectin by an incubation of 20 μg/mL of recombinant human E-selectin/Fc-chimera for 2 hrs. Lastly, the device was blocked with 1% BSA for 60 minutes to avoid any non-specific bindings.

7.2.3 Cell Culture and Isolation Test

PC3 prostate cancer cells were cultured and used as a model CTC cell line. Cells were cultured with F-12K growth medium supplemented with 10% FBS and 1% Penicillin/Streptomycin. The medium was regularly refreshed during cell proliferation and PC3 cells were used upon their confluency reaching 70-80%. Before cell isolation test, PC3 cells were pre-stained with cell-tracker and then spiked into human whole blood or RBC lysed blood. Cell solution was then injected into the E-selectin coated microfluidic chip. Regular and fluorescent microscopes were used to observe the cell rolling and isolation process. To quantify the cell rolling velocities, cell rolling process was recorded and then analyzed by ImageJ.

7.3 Results

To demonstrate the focusing effect brought by the inclined wavy pattern, a cell flowing test in a microfluidic chip with no E-selectin coating was performed, as shown in Figure 7-3. It was clearly observed that all cells were focused to the side channel with a narrow focusing band, which was explained in Figure 7-2(b). This observation assures all cells to be first focused to one side and then to be isolated based on the adhesion force difference mentioned above.

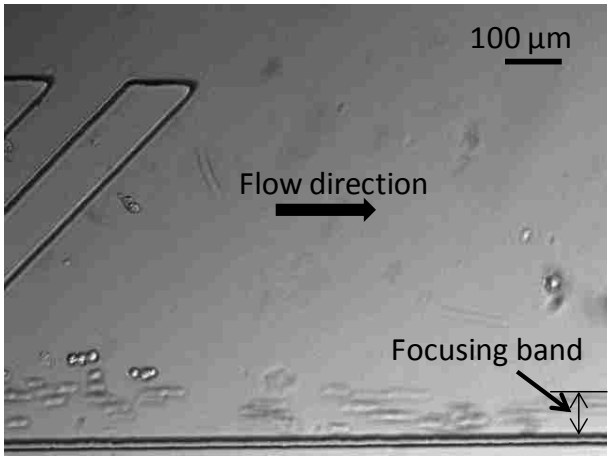

Figure 7-3 Optical image indicates cell focusing effect in a microfluidic chip with inclined patterns.

To demonstrate the adhesion difference for PC3 cells and WBCs, a time series of cell rolling on an E-selectin coated flat surface for these two cells were recorded, as shown in Figure 7-4(a) and (b), respectively. Clearly, it indicates that PC3 cells roll faster than WBCs. A further quantitative analysis of cell rolling velocities for CTCs and WBCs under different shear rates and different coating densities was performed, as shown in Figure 7-4(c). In comparison to WBCs, the larger rolling velocity for PC3 cells suggests a smaller adhesion force between PC3 cells and E-selectin. This supports our hypothesis

that PC3 cells and WBCs would be geared towards different pathways, as sketched Figure 7-1(a).

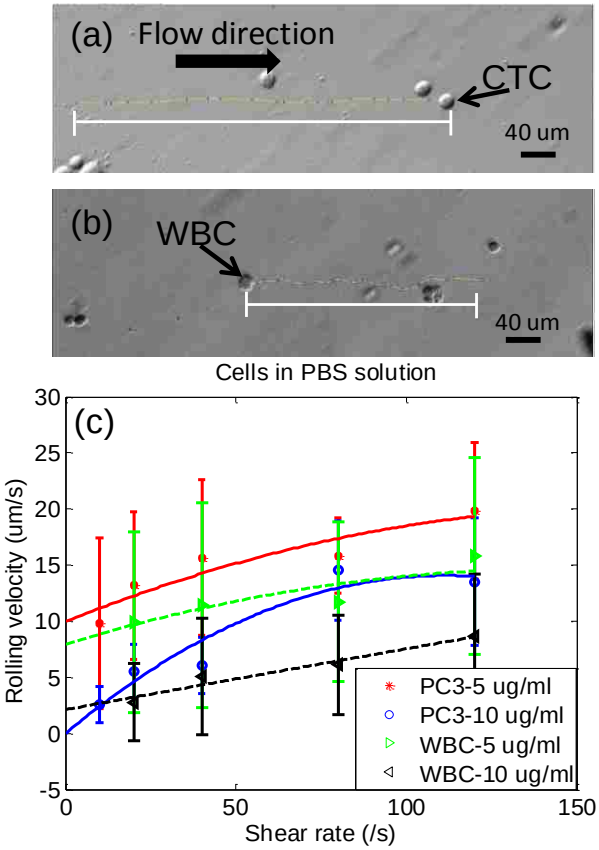

Figure 7-4 Transient cell rolling image for (a) CTC and (b) WBC. (c) Rolling velocity for PC3 cells and WBCs under different shear rates and different E-selectin coating density.

7.4 Conclusion

Our preliminary results demonstrated the cell focusing effect and adhesive force difference in the proposed microfluidic chip coated with E-selectin, which suggests that the proposed cell adhesive rolling based approach for tumor cell isolation was feasible. This approach provides a convenient strategy to isolate tumor cells from whole blood without any blood processing and cell detachment operation, thus providing a convenient

platform which is essential for tumor cell profiling and genomic analysis. Future work will be performed to validate the full functionality of this device.

Chapter 8: Summary and Outlook

This dissertation describes several techniques and platforms to advance the isolation of circulating tumor cells (CTCs), which were demonstrated to own significant clinical relevance in cancer early detection and cancer prognosis. Although various techniques were developed in literature to isolate CTCs, further improvements were still needed for device performances (such as capture efficiency, purity and viability) which were essential in producing an accurate and precise result towards precision medicine. Meanwhile, the advance of micro-/nano-techniques especially micro/nanofluidics brought lots of new approaches to solve the problems in biomedical field. Due to the nature of micro/nanofluidics such as low volume cost and fast reaction, traditional lab scale tests were scaled down to micro/nanoscale which was more fast and accurate. We were thus motivated to develop novel techniques based on micro-/nano-techniques to tackle the challenge of isolation of CTCs. Due to the heterogeneity of CTCs in size and deformability, it was noticed that CTCs of epithelial origin uniquely expressed EpCAM which allows for a specific CTC isolation based on an immunoaffinity approach. By realizing the fundamental difference between CTCs and other blood cells, we developed a microfluidic CTC isolation chip with wavy-HB patterns and optimized the design through a numerical geometric study. We then explored the effect of nanostructures in enhancing CTC isolation and developed another microfluidic chip with hierarchical micro/nanostructures by extending the previous design. Lastly, we made a few attempts to develop microfluidic platforms which allow for a direct collection of CTCs in free suspension, which was essential for off-chip CTC post-analysis. All these six projects

laid the ground for further integration of micro-/nano-techniques to tackle clinical practice. With the demonstrated results, we envision that the patient care especially cancer patient care would be advanced with the emerging liquid biopsy.

We first developed a microfluidic CTC isolation chip with wavy-HB patterns. By extending the hallmark grooved-HB chip proposed in Toner's group, we smoothed the sharp groove transitions into wavy patterns. This change eliminated extremely low shear rate regions in the groove troughs where WBCs were subjected to non-specific capture. Through a side-by-side comparison with state of the art grooved-HB chip, the wavy-HB patterns were demonstrated to present a better purity and viability performance, while preserve a high capture efficiency performance which was originally the main advantage of the grooved-HB chip. The wavy-HB chip was thus able to serve as a potential platform for clinical practice. Furthermore, this study does not only yield one single microfluidic chip, but also initiates a new strategy to improve the device performance by replacing the sharp groove patterns with smooth wavy patterns. This could be adopted to further improve many existed microfluidic platforms in literature. With the proof-of-concept work being established, a further optimization on HB structures for CTC capture was performed through a numerical study. By realizing the complex nature of ligand-receptor bond formation, we utilized a lumped parameter model to determine the adhesion probability through a few simple experimental tests. Then the modified CTC transport and capture model was used to optimize the HB structures in terms of various geometric parameters. We found that short arm ratio of 0.5 was optimized for tumor cell capture which is against 1/3 obtained from most studies in literature. This was mainly attributed to the bias of pure mixing effect on determining cell capture in most studies, while the

particulate cell transport was missing which was significantly important in CTC capture work.

By building on the foundation of the wavy-HB chip, we then explored the possibilities to integrate nanostructures to further enhance the CTC capture performance. To gain a better understanding of nanostructures on CTC capture, we investigated the geometric effects of nanopillars on capture efficiency with a focus on nanopillar diameter and spacing. It was found that CTC capture was optimized when nanopillars were smaller in diameter due to its larger overall effective contact area. Moreover, a linear correlation between capture efficiency and nanopillar diameter was unraveled which serves a guide for other researches to optimize their nanostructure platforms.

A microfluidic CTC isolation chip integrated with micro wavy-HB patterns and nanoparticles was then developed to aim at high capture efficiency and high purity performance. By combining the advantages brought by both wavy-HB patterns and nanostructures, the hierarchical micro/nanostructures were hypothesized to own a better device performance. We fabricated and assembled the device through a newly developed approach and then performed cancer cell isolation work by comparing the results with the state of the art. Significantly, the microfluidic CTC chip with hierarchical micro/nanostructures were demonstrated a higher capture efficiency and a similar purity. By pushing the device performance to another higher extreme, this platform indicates its capability to serve as a more effective platform for CTC isolation toward more demanding clinical practice.

One main limitation in anti-EpCAM based CTC isolation approaches is that captured CTCs are firmly trapped on the capture bed which brings the difficulty to collect them for off-chip analysis. By noticing this limitation, several techniques were developed to collect CTCs through stimulated release [55, 86, 88, 184]. In this dissertation, we also made two attempts to collect CTCs in free suspensions: magnetic particle assisted CTC capture and release, and cell adhesion rolling based CTC isolation. For the first idea, the fundamental working mechanism was based on the fact that magnetic particles were subjected to trapping and releasing by tuning the external magnetic field. We extend our previously developed wavy-HB chip by integrating anti-EpCAM coated magnetic particles. As a result, the advantages of the hierarchical micro/nanostructures were again adopted, while CTCs were able to be collected due to the controllable magnetic particles. A proof-of-concept work was performed and the flow cytometer analysis revealed its feasibility of CTC capture and release. Furthermore, this platform also allowed for a re-culture of collected CTCs and for the first time, we showed that the labeled immuno-magnetic particles could be removed through a continuous cell proliferation.

By realizing the complex handling process of magnetic particle assisted CTC capture and release, the second idea allows the platform to be handled with only one-step biofluid injection. The working mechanism was explained which fundamentally relies on the adhesion rolling difference between CTCs, WBCs and RBCs on the E-selection coated surface. A microfluidic chip with inclined wavy pattern was designed and a proof-of-concept work was performed to demonstrate its feasibility on CTC isolation in free suspension.

These developed microfluidic chips offer an effective approach to isolate CTCs. However, it was also noticed that no such a platform was suitable for all applications based on a few factors. First, CTCs are highly heterogeneous in immuno-expression. Specifically, CTCs undergoing epithelial to mesenchymal transition were demonstrated to have a down-regulation of EpCAM, which suggests that the anti-EpCAM based approach might not be effective any more. Another heterogeneity is attributed to various phenotypes of cancer cells. As such, currently there was not a generic antibody which could form ligand-receptor bonds with all cancer cells. Second, it was noticed for most platforms, there was always a trade-off between capture efficiency and purity. Although various techniques were developed to boost these two factors together, there still existed drawbacks such as complex fabrication process and high cost, which impedes its application in a few conditions, especially in economy poor countries. With these limitations to be mentioned, a few approaches were proposed recently and could serve as a potential solution. For example, since CTCs were found to have a down-regulated EpCAM expression, a cocktail antibody solution containing anti-EpCAM and other well-known biomarkers was used to enhance the CTC isolation [195-196]. Another alternative approach recently proposed by Toner's group is to isolate CTCs from a negative perspective. This approach was developed by realizing that CTCs were always heterogeneous while other blood cells were relatively well recognized. As a result, they developed a CTC-iChip which was negatively isolate RBCs and WBCs, thus only collecting CTCs [181].

So far, various microfluidic platforms have been developed in different research groups and companies. Although more and more clinical samples were directly tested on

a few microfluidic chips, a significant amount of clinical trials are still needed to demonstrate their clinical feasibility. Moreover, from the clinical perspective of view, although a few clinical studies showed a strong clinical relevance between cancer metastasis and CTCs, more clinical studies are still needed to support this statement. Another topic which draws lots of attention in the CTC field is that since so many platforms for CTC isolation have been established with demonstrated good performance, what exactly can patients and doctors gain out of there? Debates and exploration are always going and being engineers we look forward to more clinical insights.

References:

[1] Mathers, C.; Fat, D. M.; Boerma, J. T., The global burden of disease: 2004 update. World Health Organization: 2008.
[2] Chaffer, C. L.; Weinberg, R. A., A perspective on cancer cell metastasis. Science **2011,** 331 (6024), 1559-1564.
[3] Henschke, C. I.; McCauley, D. I.; Yankelevitz, D. F.; Naidich, D. P.; McGuinness, G.; Miettinen, O. S.; Libby, D. M.; Pasmantier, M. W.; Koizumi, J.; Altorki, N. K., Early Lung Cancer Action Project: overall design and findings from baseline screening. The Lancet **1999,** 354 (9173), 99-105.
[4] Diehl, F.; Schmidt, K.; Choti, M. A.; Romans, K.; Goodman, S.; Li, M.; Thornton, K.; Agrawal, N.; Sokoll, L.; Szabo, S. A., Circulating mutant DNA to assess tumor dynamics. Nature medicine **2008,** 14 (9), 985-990.
[5] Mitchell, P. S.; Parkin, R. K.; Kroh, E. M.; Fritz, B. R.; Wyman, S. K.; Pogosova-Agadjanyan, E. L.; Peterson, A.; Noteboom, J.; O'Briant, K. C.; Allen, A., Circulating microRNAs as stable blood-based markers for cancer detection. Proceedings of the National Academy of Sciences **2008,** 105 (30), 10513-10518.
[6] Kohn, E. C.; Liotta, L. A., Molecular insights into cancer invasion: strategies for prevention and intervention. Cancer Research **1995,** 55 (9), 1856-1862.
[7] Paterlini-Brechot, P.; Benali, N. L., Circulating tumor cells (CTC) detection: clinical impact and future directions. Cancer letters **2007,** 253 (2), 180-204.
[8] de Bono, J. S.; Scher, H. I.; Montgomery, R. B.; Parker, C.; Miller, M. C.; Tissing, H.; Doyle, G. V.; Terstappen, L. W.; Pienta, K. J.; Raghavan, D., Circulating tumor cells predict survival benefit from treatment in metastatic castration-resistant prostate cancer. Clinical Cancer Research **2008,** 14 (19), 6302-6309.
[9] Nagrath, S.; Sequist, L. V.; Maheswaran, S.; Bell, D. W.; Irimia, D.; Ulkus, L.; Smith, M. R.; Kwak, E. L.; Digumarthy, S.; Muzikansky, A., Isolation of rare circulating tumour cells in cancer patients by microchip technology. Nature **2007,** 450 (7173), 1235-1239.
[10] Sieuwerts, A. M.; Kraan, J.; Bolt, J.; van der Spoel, P.; Elstrodt, F.; Schutte, M.; Martens, J. W. M.; Gratama, J. W.; Sleijfer, S.; Foekens, J. A., Anti-Epithelial Cell Adhesion Molecule Antibodies and the Detection of Circulating Normal-Like Breast Tumor Cells. J Natl Cancer I **2009,** 101 (1), 61-66.
[11] Gascoyne, P. R. C.; Shim, S.; Noshari, J.; Becker, F. F.; Stemke-Hale, K., Correlations between the dielectric properties and exterior morphology of cells revealed by dielectrophoretic field-flow fractionation. Electrophoresis **2013,** 34 (7), 1042-1050.
[12] Ruban, G. I.; Kosmacheva, S. M.; Goncharova, N. V.; Van Bockstaele, D.; Loiko, V. A., Investigation of morphometric parameters for granulocytes and lymphocytes as applied to a solution of direct and inverse light-scattering problems. J Biomed Opt **2007,** 12 (4).
[13] Shapiro, H. M.; Schildkraut, E. R.; Curbelo, R.; Laird, C. W.; Turner, R. B.; Hirschfeld, T., Combined Blood-Cell Counting and Classification with Fluorochrome Stains and Flow Instrumentation. J Histochem Cytochem **1976,** 24 (1), 396-411.
[14] Paulus, J. M., Platelet Size in Man. Blood **1975,** 46 (3), 321-336.
[15] Bagge, U.; Gustav, V.; Gaehtgens, P., White Blood Cells: Morphology and Rheology as Related to Function. Springer Science & Business Media: 2013; Vol. 1.

[16] Diez-Silva, M.; Dao, M.; Han, J. Y.; Lim, C. T.; Suresh, S., Shape and Biomechanical Characteristics of Human Red Blood Cells in Health and Disease. Mrs Bull **2010,** 35 (5), 382-388.
[17] Li, Q. S.; Lee, G. Y. H.; Ong, C. N.; Lim, C. T., AFM indentation study of breast cancer cells. Biochem Bioph Res Co **2008,** 374 (4), 609-613.
[18] Rosenbluth, M. J.; Lam, W. A.; Fletcher, D. A., Force microscopy of nonadherent cells: A comparison of leukemia cell deformability. Biophys J **2006,** 90 (8), 2994-3003.
[19] Byler, R., Microfluidic Stiffness-Dependent Separation of Red Blood Cells for Early Malaria Diagnosis and Surveillance. **2013**.
[20] Radmacher, M.; Fritz, M.; Kacher, C. M.; Cleveland, J. P.; Hansma, P. K., Measuring the viscoelastic properties of human platelets with the atomic force microscope. Biophys J **1996,** 70 (1), 556-567.
[21] Punnoose, E. A.; Atwal, S. K.; Spoerke, J. M.; Savage, H.; Pandita, A.; Yeh, R. F.; Pirzkall, A.; Fine, B. M.; Amler, L. C.; Chen, D. S.; Lackner, M. R., Molecular Biomarker Analyses Using Circulating Tumor Cells. Plos One **2010,** 5 (9).
[22] Trowbridge, I. S.; Ostergaard, H. L.; Johnson, P., Cd45 - a Leukocyte-Specific Member of the Protein Tyrosine Phosphatase Family. Biochim Biophys Acta **1991,** 1095 (1), 46-56.
[23] Liu, X.; Wang, S., Three-dimensional nano-biointerface as a new platform for guiding cell fate. Chemical Society Reviews **2014,** 43 (8), 2385-2401.
[24] Peng, F.; Su, Y.; Zhong, Y.; Fan, C.; Lee, S.-T.; He, Y., Silicon Nanomaterials Platform for Bioimaging, Biosensing, and Cancer Therapy. Accounts of chemical research **2014,** 47 (2), 612-623.
[25] Chen, C. S.; Mrksich, M.; Huang, S.; Whitesides, G. M.; Ingber, D. E., Geometric control of cell life and death. Science **1997,** 276 (5317), 1425-1428.
[26] Whitesides, G. M.; Ostuni, E.; Takayama, S.; Jiang, X.; Ingber, D. E., Soft lithography in biology and biochemistry. Annual review of biomedical engineering **2001,** 3 (1), 335-373.
[27] Vona, G.; Sabile, A.; Louha, M.; Sitruk, V.; Romana, S.; Schütze, K.; Capron, F.; Franco, D.; Pazzagli, M.; Vekemans, M., Isolation by size of epithelial tumor cells: a new method for the immunomorphological and molecular characterization of circulating tumor cells. The American journal of pathology **2000,** 156 (1), 57-63.
[28] Gertler, R.; Rosenberg, R.; Fuehrer, K.; Dahm, M.; Nekarda, H.; Siewert, J. R., Detection of circulating tumor cells in blood using an optimized density gradient centrifugation. In Molecular Staging of Cancer, Springer: 2003; pp 149-155.
[29] Wang, G.; Mao, W.; Byler, R.; Patel, K.; Henegar, C.; Alexeev, A.; Sulchek, T., Stiffness dependent separation of cells in a microfluidic device. PloS one **2013,** 8 (10), e75901.
[30] Wan, Y.; Kim, Y.-t.; Li, N.; Cho, S. K.; Bachoo, R.; Ellington, A. D.; Iqbal, S. M., Surface-immobilized aptamers for cancer cell isolation and microscopic cytology. Cancer Res. **2010,** 70 (22), 9371-9380.
[31] Stott, S. L.; Hsu, C.-H.; Tsukrov, D. I.; Yu, M.; Miyamoto, D. T.; Waltman, B. A.; Rothenberg, S. M.; Shah, A. M.; Smas, M. E.; Korir, G. K., Isolation of circulating tumor cells using a microvortex-generating herringbone-chip. Proceedings of the National Academy of Sciences **2010,** 107 (43), 18392-18397.

[32] Chen, J.; Li, J.; Sun, Y., Microfluidic approaches for cancer cell detection, characterization, and separation. Lab on a Chip **2012,** 12 (10), 1753-1767.
[33] Jin, C.; McFaul, S. M.; Duffy, S. P.; Deng, X.; Tavassoli, P.; Black, P. C.; Ma, H., Technologies for label-free separation of circulating tumor cells: from historical foundations to recent developments. Lab on a Chip **2014,** 14 (1), 32-44.
[34] Nagrath, S.; Sequist, L. V.; Maheswaran, S.; Bell, D. W.; Irimia, D.; Ulkus, L.; Smith, M. R.; Kwak, E. L.; Digumarthy, S.; Muzikansky, A.; Ryan, P.; Balis, U. J.; Tompkins, R. G.; Haber, D. A.; Toner, M., Isolation of rare circulating tumour cells in cancer patients by microchip technology. Nature **2007,** 450 (7173), 1235-U10.
[35] Stott, S. L.; Hsu, C. H.; Tsukrov, D. I.; Yu, M.; Miyamoto, D. T.; Waltman, B. A.; Rothenberg, S. M.; Shah, A. M.; Smas, M. E.; Korir, G. K.; Floyd, F. P.; Gilman, A. J.; Lord, J. B.; Winokur, D.; Springer, S.; Irimia, D.; Nagrath, S.; Sequist, L. V.; Lee, R. J.; Isselbacher, K. J.; Maheswaran, S.; Haber, D. A.; Toner, M., Isolation of circulating tumor cells using a microvortex-generating herringbone-chip. P Natl Acad Sci USA **2010,** 107 (43), 18392-18397.
[36] Warkiani, M. E.; Guan, G. F.; Luan, K. B.; Lee, W. C.; Bhagat, A. A. S.; Chaudhuri, P. K.; Tan, D. S. W.; Lim, W. T.; Lee, S. C.; Chen, P. C. Y.; Lim, C. T.; Han, J., Slanted spiral microfluidics for the ultra-fast, label-free isolation of circulating tumor cells. Lab Chip **2014,** 14 (1), 128-137.
[37] Moon, H. S.; Kwon, K.; Kim, S. I.; Han, H.; Sohn, J.; Lee, S.; Jung, H. I., Continuous separation of breast cancer cells from blood samples using multi-orifice flow fractionation (MOFF) and dielectrophoresis (DEP). Lab Chip **2011,** 11 (6), 1118-1125.
[38] Stroock, A. D.; Dertinger, S. K.; Ajdari, A.; Mezić, I.; Stone, H. A.; Whitesides, G. M., Chaotic mixer for microchannels. Science **2002,** 295 (5555), 647-651.
[39] Wang, S.; Liu, K.; Liu, J.; Yu, Z. T. F.; Xu, X.; Zhao, L.; Lee, T.; Lee, E. K.; Reiss, J.; Lee, Y. K., Highly efficient capture of circulating tumor cells by using nanostructured silicon substrates with integrated chaotic micromixers. Angewandte Chemie International Edition **2011,** 50 (13), 3084-3088.
[40] Martin, R. S.; Root, P. D.; Spence, D. M., Microfluidic technologies as platforms for performing quantitative cellular analyses in an in vitro environment. Analyst **2006,** 131 (11), 1197-1206.
[41] Beebe, D. J.; Mensing, G. A.; Walker, G. M., Physics and applications of microfluidics in biology. Annu Rev Biomed Eng **2002,** 4, 261-286.
[42] Jokerst, J. C.; Emory, J. M.; Henry, C. S., Advances in microfluidics for environmental analysis. Analyst **2012,** 137 (1), 24-34.
[43] Liu, Y.; Wang, S.; Song, Y.; Yang, J., Biospecies Capture and Detection at Low Concentration. Micro and Nanosystems **2012,** 4 (4), 254-272.
[44] Chen, J. H.; Zhou, Y. L.; Wang, D. H.; He, F.; Rotello, V. M.; Carter, K. R.; Watkins, J. J.; Nugen, S. R., UV-nanoimprint lithography as a tool to develop flexible microfluidic devices for electrochemical detection. Lab Chip **2015,** 15 (14), 3086-3094.
[45] Qin, Z. P.; Chan, W. C. W.; Boulware, D. R.; Akkin, T.; Butler, E. K.; Bischof, J. C., Significantly Improved Analytical Sensitivity of Lateral Flow Immunoassays by Using Thermal Contrast. Angew Chem Int Edit **2012,** 51 (18), 4358-4361.
[46] Warkiani, M. E.; Khoo, B. L.; Tan, D. S. W.; Bhagat, A. A. S.; Lim, W. T.; Yap, Y. S.; Lee, S. C.; Soo, R. A.; Han, J.; Lim, C. T., An ultra-high-throughput spiral

microfluidic biochip for the enrichment of circulating tumor cells. Analyst **2014,** 139 (13), 3245-3255.
[47] Ilie, M.; Hofman, V.; Long-Mira, E.; Selva, E.; Vignaud, J. M.; Padovani, B.; Mouroux, J.; Marquette, C. H.; Hofman, P., "Sentinel" Circulating Tumor Cells Allow Early Diagnosis of Lung Cancer in Patients with Chronic Obstructive Pulmonary Disease. Plos One **2014,** 9 (10).
[48] Marx, V., Tracking Metastasis and Tricking Cancer. Nature **2013,** 494 (7435), 131-+.
[49] Miyamoto, D. T.; Sequist, L. V.; Lee, R. J., Circulating tumour cells-monitoring treatment response in prostate cancer. Nat Rev Clin Oncol **2014,** 11 (7), 401-12.
[50] de Bono, J. S.; Scher, H. I.; Montgomery, R. B.; Parker, C.; Miller, M. C.; Tissing, H.; Doyle, G. V.; Terstappen, L. W.; Pienta, K. J.; Raghavan, D., Circulating tumor cells predict survival benefit from treatment in metastatic castration-resistant prostate cancer. Clin Cancer Res **2008,** 14 (19), 6302-9.
[51] Murlidhar, V.; Zeinali, M.; Grabauskiene, S.; Ghannad-Rezaie, M.; Wicha, M. S.; Simeone, D. M.; Ramnath, N.; Reddy, R. M.; Nagrath, S., A Radial Flow Microfluidic Device for Ultra-High-Throughput Affinity-Based Isolation of Circulating Tumor Cells. Small **2014,** 10 (23), 4895-4904.
[52] Chen, Y. C.; Li, P.; Huang, P. H.; Xie, Y. L.; Mai, J. D.; Wang, L.; Nguyen, N. T.; Huang, T. J., Rare cell isolation and analysis in microfluidics. Lab Chip **2014,** 14 (4), 626-645.
[53] Asghar, W.; Wan, Y.; Ilyas, A.; Bachoo, R.; Kim, Y. T.; Iqbal, S. M., Electrical fingerprinting, 3D profiling and detection of tumor cells with solid-state micropores. Lab Chip **2012,** 12 (13), 2345-2352.
[54] Wang, S. T.; Liu, K.; Liu, J. A.; Yu, Z. T. F.; Xu, X. W.; Zhao, L. B.; Lee, T.; Lee, E. K.; Reiss, J.; Lee, Y. K.; Chung, L. W. K.; Huang, J. T.; Rettig, M.; Seligson, D.; Duraiswamy, K. N.; Shen, C. K. F.; Tseng, H. R., Highly Efficient Capture of Circulating Tumor Cells by Using Nanostructured Silicon Substrates with Integrated Chaotic Micromixers. Angew Chem Int Edit **2011,** 50 (13), 3084-3088.
[55] Sheng, W. A.; Ogunwobi, O. O.; Chen, T.; Zhang, J. L.; George, T. J.; Liu, C.; Fan, Z. H., Capture, release and culture of circulating tumor cells from pancreatic cancer patients using an enhanced mixing chip. Lab Chip **2014,** 14 (1), 89-98.
[56] Stroock, A. D.; Dertinger, S. K. W.; Ajdari, A.; Mezic, I.; Stone, H. A.; Whitesides, G. M., Chaotic mixer for microchannels. Science **2002,** 295 (5555), 647-651.
[57] Hsu, C. H.; Di Carlo, D.; Chen, C. C.; Irimia, D.; Toner, M., Microvortex for focusing, guiding and sorting of particles. Lab Chip **2008,** 8 (12), 2128-2134.
[58] Forbes, T. P.; Kralj, J. G., Engineering and analysis of surface interactions in a microfluidic herringbone micromixer. Lab Chip **2012,** 12 (15), 2634-2637.
[59] Lu, Y. T.; Zhao, L. B.; Shen, Q. L.; Garcia, M. A.; Wu, D. X.; Hou, S.; Song, M.; Xu, X. C.; OuYang, W. H.; OuYang, W. W. L.; Lichterman, J.; Luo, Z.; Xuan, X.; Huang, J. T.; Chung, L. W. K.; Rettig, M.; Tseng, H. R.; Shao, C.; Posadas, E. M., NanoVelcro Chip for CTC enumeration in prostate cancer patients. Methods **2013,** 64 (2), 144-152.
[60] Hou, S.; Zhao, L. B.; Shen, Q. L.; Yu, J. H.; Ng, C.; Kong, X. J.; Wu, D. X.; Song, M.; Shi, X. H.; Xu, X. C.; OuYang, W. H.; He, R. X.; Zhao, X. Z.; Lee, T.; Brunicardi, F. C.; Garcia, M. A.; Ribas, A.; Lo, R. S.; Tseng, H. R., Polymer Nanofiber-Embedded Microchips for Detection, Isolation, and Molecular Analysis of Single Circulating Melanoma Cells. Angew Chem Int Edit **2013,** 52 (12), 3379-3383.

[61] Sheng, W. A.; Chen, T.; Tan, W. H.; Fan, Z. H., Multivalent DNA Nanospheres for Enhanced Capture of Cancer Cells in Microfluidic Devices. Acs Nano **2013,** 7 (8), 7067-7076.
[62] Decuzzi, P.; Ferrari, M., The adhesive strength of non-spherical particles mediated by specific interactions. Biomaterials **2006,** 27 (30), 5307-5314.
[63] Zhang, X.; Huk, D. J.; Wang, Q.; Lincoln, J.; Zhao, Y., A microfluidic shear device that accommodates parallel high and low stress zones within the same culturing chamber. Biomicrofluidics **2014,** 8 (5).
[64] Xia, Y. N.; Whitesides, G. M., Soft lithography. Annu Rev Mater Sci **1998,** 28, 153-184.
[65] Bu, I. Y. Y.; Oei, S. P., Hydrophobic vertically aligned carbon nanotubes on Corning glass for self cleaning applications. Appl Surf Sci **2010,** 256 (22), 6699-6704.
[66] O'Neill, F. T.; Sheridan, J. T., Photoresist reflow method of microlens production Part I: Background and experiments. Optik **2002,** 113 (9), 391-404.
[67] Roy, E.; Voisin, B.; Gravel, J. F.; Peytavi, R.; Boudreau, D.; Veres, T., Microlens array fabrication by enhanced thermal reflow process: Towards efficient collection of fluorescence light from microarrays. Microelectron Eng **2009,** 86 (11), 2255-2261.
[68] Wang, S. Q.; Wan, Y.; Liu, Y. L., Effects of nanopillar array diameter and spacing on cancer cell capture and cell behaviors. Nanoscale **2014,** 6 (21), 12482-12489.
[69] Hong, W. Y.; Jeon, S. H.; Lee, E. S.; Cho, Y., An integrated multifunctional platform based on biotin-doped conducting polymer nanowires for cell capture, release, and electrochemical sensing. Biomaterials **2014,** 35 (36), 9573-9580.
[70] Launiere, C. A.; Czaplewski, G. J.; Myung, J. H.; Hong, S.; Eddington, D. T., Rheologically biomimetic cell suspensions for decreased cell settling in microfluidic devices. Biomed Microdevices **2011,** 13 (3), 549-557.
[71] Wang, S. Q.; Zhou, Y. H.; Tan, J. F.; Xu, J.; Yang, J.; Liu, Y. L., Computational modeling of magnetic nanoparticle targeting to stent surface under high gradient field. Comput Mech **2014,** 53 (3), 403-412.
[72] Tan, J. F.; Wang, S. Q.; Yang, J.; Liu, Y. L., Coupled particulate and continuum model for nanoparticle targeted delivery. Comput Struct **2013,** 122, 128-134.
[73] Aubin, J.; Fletcher, D. F.; Xuereb, C., Design of micromixers using CFD modelling. Chem Eng Sci **2005,** 60 (8-9), 2503-2516.
[74] Lynn, N. S.; Dandy, D. S., Geometrical optimization of helical flow in grooved micromixers. Lab Chip **2007,** 7 (5), 580-587.
[75] Williams, M. S.; Longmuir, K. J.; Yager, P., A practical guide to the staggered herringbone mixer. Lab Chip **2008,** 8 (7), 1121-1129.
[76] Wan, Y.; Tan, J. F.; Asghar, W.; Kim, Y. T.; Liu, Y. L.; Iqbal, S. M., Velocity Effect on Aptamer-Based Circulating Tumor Cell Isolation in Microfluidic Devices. J Phys Chem B **2011,** 115 (47), 13891-13896.
[77] Mitchell, M. J.; Wayne, E.; Rana, K.; Schaffer, C. B.; King, M. R., TRAIL-coated leukocytes that kill cancer cells in the circulation. P Natl Acad Sci USA **2014,** 111 (3), 930-935.
[78] Xue, P.; Ye, K.; Gao, J.; Wu, Y. F.; Guo, J. H.; Hui, K. M.; Kang, Y. J., Isolation and elution of Hep3B circulating tumor cells using a dual-functional herringbone chip. Microfluid Nanofluid **2014,** 16 (3), 605-612.

[79] Hyun, K. A.; Lee, T. Y.; Lee, S. H.; Jung, H. I., Two-stage microfluidic chip for selective isolation of circulating tumor cells (CTCs). Biosens Bioelectron **2015,** 67, 86-92.
[80] Talasaz, A. H.; Powell, A. A.; Huber, D. E.; Berbee, J. G.; Roh, K. H.; Yu, W.; Xiao, W. Z.; Davis, M. M.; Pease, R. F.; Mindrinos, M. N.; Jeffrey, S. S.; Davis, R. W., Isolating highly enriched populations of circulating epithelial cells and other rare cells from blood using a magnetic sweeper device. P Natl Acad Sci USA **2009,** 106 (10), 3970-3975.
[81] Hosic, S. J.; Murthy, S. K.; Koppes, A. N., Microfluidic Sample Preparation for Single Cell Analysis. Anal Chem **2016,** 88 (1), 354-380.
[82] de Ridder, D.; van der Linden, C.; Schonewille, T.; Dik, W. A.; Reinders, M. J. T.; van Dongen, J. J. M.; Staal, F. J. T., Purity for clarity: the need for purification of tumor cells in DNA microarray studies. Leukemia **2005,** 19 (4), 618-627.
[83] Mego, M.; De Giorgi, U.; Dawood, S.; Wang, X. M.; Valero, V.; Andreopoulou, E.; Handy, B.; Ueno, N. T.; Reuben, J. M.; Cristofanilli, M., Characterization of metastatic breast cancer patients with nondetectable circulating tumor cells. Int J Cancer **2011,** 129 (2), 417-423.
[84] Wicha, M. S.; Hayes, D. F., Circulating Tumor Cells: Not All Detected Cells Are Bad and Not All Bad Cells Are Detected. Journal of Clinical Oncology **2011,** 29 (12), 1508-1511.
[85] Chen, L.; Hu, C. S.; Chen, X. Z.; Hu, G. Q.; Cheng, Z. B.; Sun, Y.; Li, W. X.; Chen, Y. Y.; Xie, F. Y.; Liang, S. B.; Chen, Y.; Xu, T. T.; Li, B.; Long, G. X.; Wang, S. Y.; Zheng, B. M.; Guo, Y.; Sun, Y.; Mao, Y. P.; Tang, L. L.; Chen, Y. M.; Liu, M. Z.; Ma, J., Concurrent chemoradiotherapy plus adjuvant chemotherapy versus concurrent chemoradiotherapy alone in patients with locoregionally advanced nasopharyngeal carcinoma: a phase 3 multicentre randomised controlled trial. Lancet Oncol **2012,** 13 (2), 163-171.
[86] Xu, Y.; Phillips, J. A.; Yan, J. L.; Li, Q. G.; Fan, Z. H.; Tan, W. H., Aptamer-Based Microfluidic Device for Enrichment, Sorting, and Detection of Multiple Cancer Cells. Anal Chem **2009,** 81 (17), 7436-7442.
[87] Sheng, W. A.; Chen, T.; Katnath, R.; Xiong, X. L.; Tan, W. H.; Fan, Z. H., Aptamer-Enabled Efficient Isolation of Cancer Cells from Whole Blood Using a Microfluidic Device. Anal Chem **2012,** 84 (9), 4199-4206.
[88] Hou, S.; Zhao, H. C.; Zhao, L. B.; Shen, Q. L.; Wei, K. S.; Suh, D. Y.; Nakao, A.; Garcia, M. A.; Song, M.; Lee, T.; Xiong, B.; Luo, S. C.; Tseng, H. R.; Yu, H. H., Capture and Stimulated Release of Circulating Tumor Cells on Polymer-Grafted Silicon Nanostructures. Adv Mater **2013,** 25 (11), 1547-1551.
[89] Wang, L. X.; Asghar, W.; Demirci, U.; Wan, Y., Nanostructured substrates for isolation of circulating tumor cells. Nano Today **2013,** 8 (4), 374-387.
[90] Chen, W. Q.; Weng, S. N.; Zhang, F.; Allen, S.; Li, X.; Bao, L. W.; Lam, R. H. W.; Macoska, J. A.; Merajver, S. D.; Fu, J. P., Nanoroughened Surfaces for Efficient Capture of Circulating Tumor Cells without Using Capture Antibodies. Acs Nano **2013,** 7 (1), 566-575.
[91] Gao, Y.; Li, W. J.; Pappas, D., Recent advances in microfluidic cell separations. Analyst **2013,** 138 (17), 4714-4721.
[92] Pappas, D., Microfluidics and cancer analysis: cell separation, cell/tissue culture, cell mechanics, and integrated analysis systems. Analyst **2016,** 141 (2), 525-535.

[93] Shields, C. W.; Reyes, C. D.; Lopez, G. P., Microfluidic cell sorting: a review of the advances in the separation of cells from debulking to rare cell isolation. Lab Chip **2015,** 15 (5), 1230-1249.
[94] Myung, J. H.; Hong, S., Microfluidic devices to enrich and isolate circulating tumor cells. Lab Chip **2015,** 15 (24), 4500-4511.
[95] Ke, Z.; Lin, M.; Chen, J. F.; Choi, J. S.; Zhang, Y.; Fong, A.; Liang, A. J.; Chen, S. F.; Li, Q.; Fang, W.; Zhang, P.; Garcia, M. A.; Lee, T.; Song, M.; Lin, H. A.; Zhao, H.; Luo, S. C.; Hou, S.; Yu, H. H.; Tseng, H. R., Programming thermoresponsiveness of NanoVelcro substrates enables effective purification of circulating tumor cells in lung cancer patients. Acs Nano **2015,** 9 (1), 62-70.
[96] Fourcade, E.; Wadley, R.; Hoefsloot, H. C. J.; Green, A.; Iedema, P. D., CFD calculation of laminar striation thinning in static mixer reactors. Chem Eng Sci **2001,** 56 (23), 6729-6741.
[97] Nauman, E. B.; Kothari, D.; Nigam, K. D. P., Static mixers to promote axial mixing. Chem Eng Res Des **2002,** 80 (A6), 681-685.
[98] Hobbs, D. M.; Muzzio, F. J., The Kenics static mixer: a three-dimensional chaotic flow. Chem Eng J **1997,** 67 (3), 153-166.
[99] Wang, H. Z.; Iovenitti, P.; Harvey, E.; Masood, S., Numerical investigation of mixing in microchannels with patterned grooves. J Micromech Microeng **2003,** 13 (6), 801-808.
[100] Smith, J. P.; Lannin, T. B.; Syed, Y. A.; Santana, S. M.; Kirby, B. J., Parametric control of collision rates and capture rates in geometrically enhanced differential immunocapture (GEDI) microfluidic devices for rare cell capture. Biomed Microdevices **2014,** 16 (1), 143-151.
[101] Huang, C.; Smith, J. P.; Saha, T. N.; Rhim, A. D.; Kirby, B. J., Characterization of microfluidic shear-dependent epithelial cell adhesion molecule immunocapture and enrichment of pancreatic cancer cells from blood cells with dielectrophoresis. Biomicrofluidics **2014,** 8 (4).
[102] Chen, X.; Liu, J. Q.; Zhu, J.; Sun, Y. F.; Fan, J., Optimization of Microfluidic Immunomagnetic Chip for Circulating Tumor Cell Capture. Sensor Mater **2013,** 25 (9), 667-671.
[103] Li, Y.; Xu, F.; Liu, C.; Xu, Y. Z.; Feng, X. J.; Liu, B. F., A novel microfluidic mixer based on dual-hydrodynamic focusing for interrogating the kinetics of DNA-protein interaction. Analyst **2013,** 138 (16), 4475-4482.
[104] Tan, J. F.; Keller, W.; Sohrabi, S.; Yang, J.; Liu, Y. L., Characterization of Nanoparticle Dispersion in Red Blood Cell Suspension by the Lattice Boltzmann-Immersed Boundary Method. Nanomaterials-Basel **2016,** 6 (2).
[105] Tan, J. F.; Thomas, A.; Liu, Y. L., Influence of red blood cells on nanoparticle targeted delivery in microcirculation. Soft Matter **2012,** 8 (6), 1934-1946.
[106] Wan, Y.; Tan, J.; Asghar, W.; Kim, Y.-t.; Liu, Y.; Iqbal, S. M., Velocity effect on aptamer-based circulating tumor cell isolation in microfluidic devices. The Journal of Physical Chemistry B **2011,** 115 (47), 13891-13896.
[107] Usami, S.; Chen, H. H.; Zhao, Y. H.; Chien, S.; Skalak, R., Design and Construction of a Linear Shear-Stress Flow Chamber. Ann Biomed Eng **1993,** 21 (1), 77-83.

[108] Jemal, A.; Siegel, R.; Ward, E.; Hao, Y. P.; Xu, J. Q.; Murray, T.; Thun, M. J., Cancer statistics, 2008. Ca-Cancer J Clin **2008,** 58 (2), 71-96.
[109] Liu, Y. Z.; Kim, B. J.; Sung, H. J., Two-fluid mixing in a microchannel. Int J Heat Fluid Fl **2004,** 25 (6), 986-995.
[110] Murthy, S. K.; Sin, A.; Tompkins, R. G.; Toner, M., Effect of flow and surface conditions on human lymphocyte isolation using microfluidic chambers. Langmuir **2004,** 20 (26), 11649-11655.
[111] Cho, Y.; Shim, T. S.; Yang, S., Spatially Selective Nucleation and Growth of Water Droplets on Hierarchically Patterned Polymer Surfaces. Adv Mater **2016,** 28 (7), 1433-1439.
[112] Stroock, A. D.; McGraw, G. J., Investigation of the staggered herringbone mixer with a simple analytical model. Philos T Roy Soc A **2004,** 362 (1818), 971-986.
[113] Du, Y.; Zhang, Z. Y.; Yim, C.; Lin, M.; Cao, X. D., A simplified design of the staggered herringbone micromixer for practical applications. Biomicrofluidics **2010,** 4 (2).
[114] Hassell, D. G.; Zimmerman, W. B., Investigation of the convective motion through a staggered herringbone micromixer at low Reynolds number flow. Chem Eng Sci **2006,** 61 (9), 2977-2985.
[115] Pantel, K.; Brakenhoff, R. H.; Brandt, B., Detection, clinical relevance and specific biological properties of disseminating tumour cells. Nat Rev Cancer **2008,** 8 (5), 329-40.
[116] Pratt, E. D.; Huang, C.; Hawkins, B. G.; Gleghorn, J. P.; Kirby, B. J., Rare cell capture in microfluidic devices. Chemical engineering science **2011,** 66 (7), 1508-1522.
[117] Gertler, R.; Rosenberg, R.; Fuehrer, K.; Dahm, M.; Nekarda, H.; Siewert, J., Detection of Circulating Tumor Cells in Blood Using an Optimized Density Gradient Centrifugation. In Molecular Staging of Cancer, Allgayer, H.; Heiss, M.; Schildberg, F., Eds. Springer Berlin Heidelberg: 2003; Vol. 162, pp 149-155.
[118] Vona, G.; Sabile, A.; Louha, M.; Sitruk, V.; Romana, S.; Schutze, K.; Capron, F.; Franco, D.; Pazzagli, M.; Vekemans, M.; Lacour, B.; Brechot, C.; Paterlini-Brechot, P., Isolation by size of epithelial tumor cells : a new method for the immunomorphological and molecular characterization of circulatingtumor cells. Am J Pathol **2000,** 156 (1), 57-63.
[119] Tan, S. J.; Lakshmi, R. L.; Chen, P.; Lim, W. T.; Yobas, L.; Lim, C. T., Versatile label free biochip for the detection of circulating tumor cells from peripheral blood in cancer patients. Biosens Bioelectron **2010,** 26 (4), 1701-5.
[120] Stott, S. L.; Hsu, C.-H.; Tsukrov, D. I.; Yu, M.; Miyamoto, D. T.; Waltman, B. A.; Rothenberg, S. M.; Shah, A. M.; Smas, M. E.; Korir, G. K.; Floyd, F. P.; Gilman, A. J.; Lord, J. B.; Winokur, D.; Springer, S.; Irimia, D.; Nagrath, S.; Sequist, L. V.; Lee, R. J.; Isselbacher, K. J.; Maheswaran, S.; Haber, D. A.; Toner, M., Isolation of circulating tumor cells using a microvortex-generating herringbone-chip. Proceedings of the National Academy of Sciences **2010**.
[121] Nagrath, S.; Sequist, L. V.; Maheswaran, S.; Bell, D. W.; Irimia, D.; Ulkus, L.; Smith, M. R.; Kwak, E. L.; Digumarthy, S.; Muzikansky, A.; Ryan, P.; Balis, U. J.; Tompkins, R. G.; Haber, D. A.; Toner, M., Isolation of rare circulating tumour cells in cancer patients by microchip technology. Nature **2007,** 450 (7173), 1235-9.
[122] Zhao, W.; Cui, C. H.; Bose, S.; Guo, D.; Shen, C.; Wong, W. P.; Halvorsen, K.; Farokhzad, O. C.; Teo, G. S. L.; Phillips, J. A., Bioinspired multivalent DNA network for

capture and release of cells. Proceedings of the National Academy of Sciences **2012,** 109 (48), 19626-19631.
[123] Wang, L.; Asghar, W.; Demirci, U.; Wan, Y., Nanostructured substrates for isolation of circulating tumor cells. Nano Today **2013,** 8 (4), 374-387.
[124] Chen, W.; Weng, S.; Zhang, F.; Allen, S.; Li, X.; Bao, L.; Lam, R. H.; Macoska, J. A.; Merajver, S. D.; Fu, J., Nanoroughened surfaces for efficient capture of circulating tumor cells without using capture antibodies. ACS nano **2012,** 7 (1), 566-575.
[125] Wang, S.; Wang, H.; Jiao, J.; Chen, K. J.; Owens, G. E.; Kamei, K. i.; Sun, J.; Sherman, D. J.; Behrenbruch, C. P.; Wu, H., Three- Dimensional Nanostructured Substrates toward Efficient Capture of Circulating Tumor Cells. Angewandte Chemie **2009,** 121 (47), 9132-9135.
[126] Myung, J. H.; Gajjar, K. A.; Saric, J.; Eddington, D. T.; Hong, S., Dendrimer- Mediated Multivalent Binding for the Enhanced Capture of Tumor Cells. Angewandte Chemie **2011,** 123 (49), 11973-11976.
[127] Yin, S.; Wu, Y. L.; Hu, B.; Wang, Y.; Cai, P.; Tan, C. K.; Qi, D.; Zheng, L.; Leow, W. R.; Tan, N. S., Three- Dimensional Graphene Composite Macroscopic Structures for Capture of Cancer Cells. Advanced Materials Interfaces **2014,** 1 (1).
[128] Park, G.-S.; Kwon, H.; Kwak, D. W.; Park, S. Y.; Kim, M.; Lee, J.-H.; Han, H.; Heo, S.; Li, X. S.; Lee, J. H., Full surface embedding of gold clusters on silicon nanowires for efficient capture and photothermal therapy of circulating tumor cells. Nano letters **2012,** 12 (3), 1638-1642.
[129] Sekine, J.; Luo, S. C.; Wang, S.; Zhu, B.; Tseng, H. R.; Yu, H. H., Functionalized conducting polymer nanodots for enhanced cell capturing: the synergistic effect of capture agents and nanostructures. Adv Mater **2011,** 23 (41), 4788-92.
[130] Mitchell, M. J.; Castellanos, C. A.; King, M. R., Nanostructured surfaces to target and kill circulating tumor cells while repelling leukocytes. Journal of Nanomaterials **2012,** 2012, 5.
[131] Yoon, H. J.; Kim, T. H.; Zhang, Z.; Azizi, E.; Pham, T. M.; Paoletti, C.; Lin, J.; Ramnath, N.; Wicha, M. S.; Hayes, D. F., Sensitive capture of circulating tumour cells by functionalized graphene oxide nanosheets. Nature nanotechnology **2013,** 8 (10), 735-741.
[132] Liu, X.; Chen, L.; Liu, H.; Yang, G.; Zhang, P.; Han, D.; Wang, S.; Jiang, L., Bio-inspired soft polystyrene nanotube substrate for rapid and highly efficient breast cancer-cell capture. NPG Asia Materials **2013,** 5 (9), e63.
[133] Yang, G.; Liu, H.; Liu, X.; Zhang, P.; Huang, C.; Xu, T.; Jiang, L.; Wang, S., Cancer Cells: Underwater- Transparent Nanodendritic Coatings for Directly Monitoring Cancer Cells. Advanced healthcare materials **2014,** 3 (3), 460-460.
[134] den Toonder, J., Circulating tumor cells: the Grand Challenge. Lab on a chip **2011,** 11 (3), 375-377.
[135] Liu, H.; Liu, X.; Meng, J.; Zhang, P.; Yang, G.; Su, B.; Sun, K.; Chen, L.; Han, D.; Wang, S., Hydrophobic Interaction- Mediated Capture and Release of Cancer Cells on Thermoresponsive Nanostructured Surfaces. Advanced Materials **2013,** 25 (6), 922-927.
[136] Zhang, P.; Chen, L.; Xu, T.; Liu, H.; Liu, X.; Meng, J.; Yang, G.; Jiang, L.; Wang, S., Programmable fractal nanostructured interfaces for specific recognition and electrochemical release of cancer cells. Advanced Materials **2013,** 25 (26), 3566-3570.

[137] Wan, Y.; Mahmood, M.; Li, N.; Allen, P. B.; Kim, Y. t.; Bachoo, R.; Ellington, A. D.; Iqbal, S. M., Nanotextured substrates with immobilized aptamers for cancer cell isolation and cytology. Cancer **2012,** 118 (4), 1145-1154.
[138] Qi, S.; Yi, C.; Ji, S.; Fong, C.-C.; Yang, M., Cell adhesion and spreading behavior on vertically aligned silicon nanowire arrays. ACS applied materials & interfaces **2008,** 1 (1), 30-34.
[139] Hu, W.; Crouch, A. S.; Miller, D.; Aryal, M.; Luebke, K. J., Inhibited cell spreading on polystyrene nanopillars fabricated by nanoimprinting and in situ elongation. Nanotechnology **2010,** 21 (38), 385301.
[140] Kim, D.-J.; Seol, J.-K.; Lee, G.; Kim, G.-S.; Lee, S.-K., Cell adhesion and migration on nanopatterned substrates and their effects on cell-capture yield. Nanotechnology **2012,** 23 (39), 395102.
[141] Guillou, H.; Depraz-Depland, A.; Planus, E.; Vianay, B.; Chaussy, J.; Grichine, A.; Albigès-Rizo, C.; Block, M. R., Lamellipodia nucleation by filopodia depends on integrin occupancy and downstream Rac1 signaling. Experimental cell research **2008,** 314 (3), 478-488.
[142] Geyer, N.; Fuhrmann, B.; Huang, Z. P.; de Boor, J.; Leipner, H. S.; Werner, P., Model for the Mass Transport during Metal-Assisted Chemical Etching with Contiguous Metal Films As Catalysts. Journal of Physical Chemistry C **2012,** 116 (24), 13446-13451.
[143] Galbraith, C. G.; Yamada, K. M.; Sheetz, M. P., The relationship between force and focal complex development. The Journal of cell biology **2002,** 159 (4), 695-705.
[144] Feng, J.; Soper, S. A.; McCarley, R. L.; Murphy, M. C. In Separation of breast cancer cells from peripherally circulating blood using antibodies fixed in microchannels, Biomedical Optics 2004, International Society for Optics and Photonics: 2004; pp 278-293.
[145] Kim, D.-J.; Lee, G.; Kim, G.-S.; Lee, S.-K., Statistical analysis of immuno-functionalized tumor-cell behaviors on nanopatterned substrates. Nanoscale research letters **2012,** 7 (1), 1-8.
[146] Jaccodine, R.; Schlegel, W., Measurement of Strains at Si-SiO2 Interface. Journal of applied physics **2004,** 37 (6), 2429-2434.
[147] Cha, T.-G.; Yi, J. W.; Moon, M.-W.; Lee, K.-R.; Kim, H.-Y., Nanoscale patterning of microtextured surfaces to control superhydrophobic robustness. Langmuir **2010,** 26 (11), 8319-8326.
[148] Ley, K.; Lundgren, E.; Berger, E.; Arfors, K.-E., Shear-dependent inhibition of granulocyte adhesion to cultured endothelium by dextran sulfate. Blood **1989,** 73 (5), 1324-1330.
[149] Wang, S.; Liu, K.; Liu, J.; Yu, Z. T. F.; Xu, X.; Zhao, L.; Lee, T.; Lee, E. K.; Reiss, J.; Lee, Y.-K.; Chung, L. W. K.; Huang, J.; Rettig, M.; Seligson, D.; Duraiswamy, K. N.; Shen, C. K. F.; Tseng, H.-R., Highly Efficient Capture of Circulating Tumor Cells by Using Nanostructured Silicon Substrates with Integrated Chaotic Micromixers. Angewandte Chemie International Edition **2011,** 50 (13), 3084-3088.
[150] Mooseker, M. S.; Tilney, L. G., Organization of an actin filament-membrane complex. Filament polarity and membrane attachment in the microvilli of intestinal epithelial cells. The Journal of cell biology **1975,** 67 (3), 725-743.

[151] Wang, B.; L. Weldon, A.; Kumnorkaew, P.; Xu, B.; Gilchrist, J. F.; Cheng, X., Effect of Surface Nanotopography on Immunoaffinity Cell Capture in Microfluidic Devices. Langmuir **2011,** 27 (17), 11229-11237.
[152] Mahmood, M. A.; Arafat, C.; Kim, Y.-t.; Iqbal, S. M. In Quantitative classification of tumor cell morphological changes on selectively functionalized biochips, Engineering in Medicine and Biology Society (EMBC), 2013 35th Annual International Conference of the IEEE, IEEE: 2013; pp 4164-4166.
[153] Krasik, E. F.; Hammer, D. A., A semianalytic model of leukocyte rolling. Biophysical journal **2004,** 87 (5), 2919-2930.
[154] Abercrombie, M., The Croonian lecture, 1978: the crawling movement of metazoan cells. Proceedings of the Royal Society of London. Series B, Biological Sciences **1980**, 129-147.
[155] Albertini, J. J.; Lyman, G. H.; Cox, C.; Yeatman, T.; Balducci, L.; Ku, N. N.; Shivers, S.; Berman, C.; Wells, K.; Rapaport, D.; Shons, A.; Horton, J.; Greenberg, H.; Nicosia, S.; Clark, R.; Cantor, A.; Reintgen, D. S., Lymphatic mapping and sentinel node biopsy in the patient with breast cancer. Jama-J Am Med Assoc **1996,** 276 (22), 1818-1822.
[156] Scher, H. I.; Jia, X. Y.; de Bono, J. S.; Fleisher, M.; Pienta, K. J.; Raghavan, D.; Heller, G., Circulating tumour cells as prognostic markers in progressive, castration-resistant prostate cancer: a reanalysis of IMMC38 trial data. Lancet Oncol **2009,** 10 (3), 233-239.
[157] Heneghan, H. M.; Miller, N.; Lowery, A. J.; Sweeney, K. J.; Newell, J.; Kerin, M. J., Circulating microRNAs as Novel Minimally Invasive Biomarkers for Breast Cancer. Ann Surg **2010,** 251 (3), 499-505.
[158] Nilsson, J.; Skog, J.; Nordstrand, A.; Baranov, V.; Mincheva-Nilsson, L.; Breakefield, X. O.; Widmark, A., Prostate cancer-derived urine exosomes: a novel approach to biomarkers for prostate cancer. Brit J Cancer **2009,** 100 (10), 1603-1607.
[159] Diamandis, E. P.; Yousef, G. M., Human tissue kallikreins: A family of new cancer biomarkers. Clin Chem **2002,** 48 (8), 1198-1205.
[160] de Bono, J. S.; Scher, H. I.; Montgomery, R. B.; Parker, C.; Miller, M. C.; Tissing, H.; Doyle, G. V.; Terstappen, L. W. W. M.; Pienta, K. J.; Raghavan, D., Circulating Tumor Cells Predict Survival Benefit from Treatment in Metastatic Castration-Resistant Prostate Cancer. Clinical Cancer Research **2008,** 14 (19), 6302-6309.
[161] Aceto, N.; Bardia, A.; Miyamoto, D. T.; Donaldson, M. C.; Wittner, B. S.; Spencer, J. A.; Yu, M.; Pely, A.; Engstrom, A.; Zhu, H. L.; Brannigan, B. W.; Kapur, R.; Stott, S. L.; Shioda, T.; Ramaswamy, S.; Ting, D. T.; Lin, C. P.; Toner, M.; Haber, D. A.; Maheswaran, S., Circulating Tumor Cell Clusters Are Oligoclonal Precursors of Breast Cancer Metastasis. Cell **2014,** 158 (5), 1110-1122.
[162] Bhagat, A. A. S.; Hou, H. W.; Li, L. D.; Lim, C. T.; Han, J. Y., Pinched flow coupled shear-modulated inertial microfluidics for high-throughput rare blood cell separation. Lab Chip **2011,** 11 (11), 1870-1878.
[163] Sollier, E.; Go, D. E.; Che, J.; Gossett, D. R.; O'Byrne, S.; Weaver, W. M.; Kummer, N.; Rettig, M.; Goldman, J.; Nickols, N.; McCloskey, S.; Kulkarni, R. P.; Di Carlo, D., Size-selective collection of circulating tumor cells using Vortex technology. Lab Chip **2014,** 14 (1), 63-77.

[164] Pethig, R.; Menachery, A.; Pells, S.; De Sousa, P., Dielectrophoresis: A Review of Applications for Stem Cell Research. J Biomed Biotechnol **2010**.
[165] Wang, G. H.; Mao, W. B.; Byler, R.; Patel, K.; Henegar, C.; Alexeev, A.; Sulchek, T., Stiffness Dependent Separation of Cells in a Microfluidic Device. Plos One **2013,** 8 (10).
[166] Wang, G. H.; Crawford, K.; Turbyfield, C.; Lam, W.; Alexeev, A.; Sulchek, T., Microfluidic cellular enrichment and separation through differences in viscoelastic deformation. Lab Chip **2015,** 15 (2), 532-540.
[167] Hyun, K. A.; Lee, T. Y.; Jung, H. I., Negative Enrichment of Circulating Tumor Cells Using a Geometrically Activated Surface Interaction Chip. Anal Chem **2013,** 85 (9), 4439-4445.
[168] Casavant, B. P.; Mosher, R.; Warrick, J. W.; Maccoux, L. J.; Berry, S. M. F.; Becker, J. T.; Chen, V.; Lang, J. M.; McNeel, D. G.; Beebe, D. J., A negative selection methodology using a microfluidic platform for the isolation and enumeration of circulating tumor cells. Methods **2013,** 64 (2), 137-143.
[169] Decher, G., Fuzzy nanoassemblies: Toward layered polymeric multicomposites. Science **1997,** 277 (5330), 1232-1237.
[170] Lin, P. C.; Yang, S., Mechanically switchable wetting on wrinkled elastomers with dual-scale roughness. Soft Matter **2009,** 5 (5), 1011-1018.
[171] Kumnorkaew, P.; Gilchrist, J. F., Effect of Nanoparticle Concentration on the Convective Deposition of Binary Suspensions. Langmuir **2009,** 25 (11), 6070-6075.
[172] Fischer, B. J., Particle convection in an evaporating colloidal droplet. Langmuir **2002,** 18 (1), 60-67.
[173] Chen, L.; Liu, X. L.; Su, B.; Li, J.; Jiang, L.; Han, D.; Wang, S. T., Aptamer-Mediated Efficient Capture and Release of T Lymphocytes on Nanostructured Surfaces. Adv Mater **2011,** 23 (38), 4376-+.
[174] Lianidou, E. S.; Markou, A., Circulating Tumor Cells in Breast Cancer: Detection Systems, Molecular Characterization, and Future Challenges. Clin Chem **2011,** 57 (9), 1242-1255.
[175] Sequist, L. V.; Nagrath, S.; Toner, M.; Haber, D. A.; Lynch, T. J., The CTC-Chip An Exciting New Tool to Detect Circulating Tumor Cells in Lung Cancer Patients. J Thorac Oncol **2009,** 4 (3), 281-283.
[176] Assef, Y. A.; Cavarra, S. M.; Damiano, A. E.; Ibarra, C.; Kotsias, B. A., Ionic currents in multidrug resistant K562 human leukemic cells. Leukemia Res **2005,** 29 (9), 1039-1047.
[177] Sun, H. G.; Tan, W. H.; Zu, Y. L., Aptamers: versatile molecular recognition probes for cancer detection. Analyst **2016,** 141 (2), 403-415.
[178] Liu, H. L.; Li, Y. Y.; Sun, K.; Fan, J. B.; Zhang, P. C.; Meng, J. X.; Wang, S. T.; Jiang, L., Dual-Responsive Surfaces Modified with Phenylboronic Acid-Containing Polymer Brush To Reversibly Capture and Release Cancer Cells. J Am Chem Soc **2013,** 135 (20), 7603-7609.
[179] Yoon, H. J.; Shanker, A.; Wang, Y.; Kozminsky, M.; Fouladdel, S.; Burness, M. L.; Azizi, E.; Wicha, M. S.; Kim, J.; Nagrath, S., Capture and release of circulating tumor cells by temperature-sensitive graphene oxide-polymer composite. Cancer Res **2015,** 75.

[180] Tang, M.; Wen, C. Y.; Wu, L. L.; Hong, S. L.; Hu, J.; Xu, C. M.; Pang, D. W.; Zhang, Z. L., A chip assisted immunomagnetic separation system for the efficient capture and in situ identification of circulating tumor cells. Lab Chip **2016,** 16 (7), 1214-23.
[181] Ozkumur, E.; Shah, A. M.; Ciciliano, J. C.; Emmink, B. L.; Miyamoto, D. T.; Brachtel, E.; Yu, M.; Chen, P. I.; Morgan, B.; Trautwein, J.; Kimura, A.; Sengupta, S.; Stott, S. L.; Karabacak, N. M.; Barber, T. A.; Walsh, J. R.; Smith, K.; Spuhler, P. S.; Sullivan, J. P.; Lee, R. J.; Ting, D. T.; Luo, X.; Shaw, A. T.; Bardia, A.; Sequist, L. V.; Louis, D. N.; Maheswaran, S.; Kapur, R.; Haber, D. A.; Toner, M., Inertial Focusing for Tumor Antigen-Dependent and -Independent Sorting of Rare Circulating Tumor Cells. Sci Transl Med **2013,** 5 (179).
[182] Sivagnanam, V.; Song, B.; Vandevyver, C.; Bunzli, J. C. G.; Gijs, M. A. M., Selective Breast Cancer Cell Capture, Culture, and Immunocytochemical Analysis Using Self-Assembled Magnetic Bead Patterns in a Microfluidic Chip. Langmuir **2010,** 26 (9), 6091-6096.
[183] Hoshino, K.; Huang, Y. Y.; Lane, N.; Huebschman, M.; Uhr, J. W.; Frenkel, E. P.; Zhang, X. J., Microchip-based immunomagnetic detection of circulating tumor cells. Lab Chip **2011,** 11 (20), 3449-3457.
[184] Liu, Y. J.; Guo, S. S.; Zhang, Z. L.; Huang, W. H.; Baigl, D.; Xie, M.; Chen, Y.; Pang, D. W., A micropillar-integrated smart microfluidic device for specific capture and sorting of cells. Electrophoresis **2007,** 28 (24), 4713-22.
[185] Lu, S.; Pugh, R. J.; Forssberg, E., Interfacial separation of particles. Elsevier: 2005; Vol. 20.
[186] Liu, Y. J.; Guo, S. S.; Zhang, Z. L.; Huang, W. H.; Baigl, D.; Xie, M.; Chen, Y.; Pang, D. W., A micropillar-integrated smart microfluidic device for specific capture and sorting of cells. Electrophoresis **2007,** 28 (24), 4713-4722.
[187] Yu, M.; Stott, S.; Toner, M.; Maheswaran, S.; Haber, D. A., Circulating tumor cells: approaches to isolation and characterization. J Cell Biol **2011,** 192 (3), 373-382.
[188] Sorger, P. K., Microfluidics closes in on point-of-care assays. Nat Biotechnol **2008,** 26 (12), 1345-1346.
[189] Barnes, J. M.; Nauseef, J. T.; Henry, M. D., Resistance to Fluid Shear Stress Is a Conserved Biophysical Property of Malignant Cells. Plos One **2012,** 7 (12).
[190] Springer, T. A., Traffic Signals for Lymphocyte Recirculation and Leukocyte Emigration - the Multistep Paradigm. Cell **1994,** 76 (2), 301-314.
[191] Myung, J. H.; Launiere, C. A.; Eddington, D. T.; Hong, S., Enhanced Tumor Cell Isolation by a Biomimetic Combination of E-selectin and anti-EpCAM: Implications for the Effective Separation of Circulating Tumor Cells (CTCs). Langmuir **2010,** 26 (11), 8589-8596.
[192] Choi, S.; Levy, O.; Coelho, M. B.; Cabral, J. M. S.; Karp, J. M.; Karnik, R., A cell rolling cytometer reveals the correlation between mesenchymal stem cell dynamic adhesion and differentiation state. Lab Chip **2014,** 14 (1), 161-166.
[193] Sunkara, V.; Park, D. K.; Hwang, H.; Chantiwas, R.; Soper, S. A.; Cho, Y. K., Simple room temperature bonding of thermoplastics and poly(dimethylsiloxane). Lab Chip **2011,** 11 (5), 962-965.
[194] Chandrasekaran, S.; Geng, Y.; DeLouise, L. A.; King, M. R., Effect of homotypic and heterotypic interaction in 3D on the E-selectin mediated adhesive properties of breast cancer cell lines. Biomaterials **2012,** 33 (35), 9037-9048.

[195] Yu, M.; Bardia, A.; Wittner, B.; Stott, S. L.; Smas, M. E.; Ting, D. T.; Isakoff, S. J.; Ciciliano, J. C.; Wells, M. N.; Shah, A. M.; Concannon, K. F.; Donaldson, M. C.; Sequist, L. V.; Brachtel, E.; Sgroi, D.; Baselga, J.; Ramaswamy, S.; Toner, M.; Haber, D. A.; Maheswaran, S., Circulating Breast Tumor Cells Exhibit Dynamic Changes in Epithelial and Mesenchymal Composition. Science **2013,** 339 (6119), 580-584.
[196] Brinkmann, F.; Hirtz, M.; Haller, A.; Gorges, T. M.; Vellekoop, M. J.; Riethdorf, S.; Muller, V.; Pantel, K.; Fuchs, H., A Versatile Microarray Platform for Capturing Rare Cells. Sci Rep-Uk **2015,** 5.

Vita

Shunqiang Wang was born to Zhiming Wang and Yueping Ye on June 25, 1990 in Yueqing, Zhejiang Province, China. He attended Zhejiang University and obtained the Bachelor degree in Mechatronics Engineering in 2011. He then joined Prof. Yaling Liu's group at Lehigh University to pursue the doctoral degree in Mechanical Engineering and was expected to graduate in May 2016. His research was focused on development of microfluidic devices for cell isolations by utilizing advanced micro-/nanotechnologies. After graduation, he will start his career as a postdoctoral research associate in Prof. Stephen Chou's group at Princeton University.

SUMMARY

Biomechanical engineer at Ph.D. level with thorough understanding of biofluid flow mechanics. Six years of hands-on experience in microfluidic device design, numerical simulation, microfabrication, surface characterization and biofluid test. Quick self-learner and strong problem solver with a strong passion in healthcare industry. Areas of expertise include:

• Microfluidic & MEMS	• Device prototyping	• Biosample processing
• Finite element modeling	• Surface functionlization	• Microfabrication
• Fluorescence	• Technical writing	•Team Leadership

EDUCATION

Lehigh University, Bethlehem, PA
Ph.D. in Mechanical Engineering, GPA: 3.9 May 2016
Zhejiang University, Hangzhou, China
B.S. in Mechatronical Engineering, GPA: 3.8 May 2011

PUBLICATIONS & CONFERENCES

Delivered research outcomes in 12 peer-reviewed journals (5 in process) and 5 conferences.

Journal Papers (In Preparation)

1. **Wang, S.**, Cheng, X., Liu, Y. Cancer Cell Capture and Release Assisted by Magnetic Particles in Hierarchical Wavy-HB Microfluidic Devices, *in preparation*.

2. **Wang, S.**, Liu, Y. Geometry Engineering of Herringbone Structures for Cancer Cell Capture in a Microfluidic Device, *in preparation*.

3. **Wang, S.**, Cheng, X., Liu, Y. Microfluidic Device with Hierarchical Micro-/nanostructures for Efficient Isolation of Rare Tumor Cells, *in preparation*.

4. Thomas, A., **Wang, S.**, Orr, C. and Liu, Y. Characterization of vascular permeability by using a biomimetic microfluidic blood vessel model, *in preparation*.

5. Sohrabi, S., **Wang, S.**, Tan, J. and Liu, Y. Nanoparticle Transport and Delivery to Pulmonary Heterogeneous Vasculature, *in preparation*.

Journal Paper (Published)

1. **Wang, S.**, Thomas, A., Lee, E., *et al.* (2016). Highly efficient and selective Isolation of Circulating Tumor Cells by Wavy-herringbone Micro-patterned Surfaces, *Analyst*, 141(7), 2228..

2. He, R., **Wang, S.**, Andrews, G., Shi, W. and Liu, Y. (2016). Generation of customizable micro-wavy pattern through grayscale direct image lithography, *Scientific Reports*, 6, 21621.

3. **Wang, S.**, Wan, Y. & Liu, Y. (2014). Effects of nanopillar array diameter and spacing on cancer cell capture and cell behaviors. *Nanoscale*, 6(21), 12482-12489. **Selected to be the cover story**.

4. **Wang, S**.*, Zhou, Y.*, Tan, J., Yang, J., & Liu, Y. (2014). Computational modeling of magnetic nanoparticle targeting to stent surface under high gradient field. *Computational Mechanics*, 1-10.

5. Tan, J., **Wang, S**., Yang, J., & Liu, Y. (2013). Coupled particulate and continuum model for nanoparticle targeted delivery. *Computers & structures*,122, 128-134.

6. Liu, Y., **Wang, S**., Song, Y. & Yang, J. (2012). Biospecies Capture and Detection at Low Concentration. *Micro and Nanosystems*, 4(4), 254-272.

7. Liu, Y., Guo, Q., **Wang, S.** & Hu, W. (2012). Electrokinetic effects on detection time of nanowire biosensor. *Applied physics letters*, 100(15), 153502.

Conferences:

1. **Wang, S.**, Ghosh, R., He, R., Liu, Y., "Isolation Of Rare Tumor Cells Using Adhesion Rolling In a Microfluidic Chip With Inclined Wavy Surfaces", *Summer Biomechanics, Bioengineering and Biotransport Conference*, June 2016. (Conference Paper & Poster Presentation)

2. Liu, Y., Thomas, A., Uhl, C., **Wang, S.**, "Microfluidic Device for Drug Particle Delivery and Permeability Evaluation", *International Conference on Nanochannels, Microchannels, and Minichannels*, July 2016. (Podium talk)

3. **Wang, S.**, Thomas, A., Lee, E., et al., "Highly-Efficient and Selective Isolation of Circulating Tumor Cells by Using a Wave-herringbone Microfluidic Device", *NGS, SCA, Mass Spec: The Road to Diagnostics*, September 2015. (Podium talk)

4. **Wang, S.**, Wan, Y., Liu, Y., "Effects of Nanopillar Array Geometry on Capture and Detachment of Circulating Tumor Cells", *7th World Congress of Biomechanics*, July 2014. (Poster Presentation)

5. **Wang, S.**, Thomas, A., Lee, E., et al., "Capturing of Circulating Tumor Cells in a Microfluidic device through Micro/Nanopatterned Surfaces", *7th World Congress of Biomechanics*, July 2014. (Podium talk)

WORK EXPERIENCE

Shanghai PerMed Biomedical Co, Ltd (Personalized Medicine), Shanghai, China
Engineering Intern Dec 2014-Jan 2015

• Created a protocol for patient blood processing and fluorescent tumor cells imaging and counting

• Collaborated with application specialists from GE Healthcare to troubleshoot cell image analysis

• Developed objective-tracking MatLab codes to study the cell motion

• Learned techniques for PCR, DNA extraction/gel electrophoresis and automated cell staining

PreScouter Inc., Evanston, IL
Part-time Consultant Scholar Apr 2014-April 2015

• Pursued academic/industrial searches and proposed possible solutions for Fortune 500 companies

SKILLS

Software: COMSOL Multiphysics, AutoCAD, Solidworks, MatLab, Mimics, Ansys, Lammps, ImageJ, Blender
Applications: Immunoaffinity Assay, Fast Prototype, Fluorescent Microscopy, Regulatory Affairs, ISO Standards

AWARDS & HONORS

Joseph Petraglia Community Service Award, Lehigh University 2013
Rossin Doctoral Fellowship, Lehigh University 2013
Dean's Doctoral Assistantship, Lehigh University 2011
Outstanding Bachelor Thesis Award, Zhejiang University 2011

LEADERSHIPS & VOLUNTEERS & TUTORS

MRI Department in St. Lukes Hospital, *Volunteer* (3 hours every week for one year) 2014
S.T.A.R. (one-year program to help academically disadvantage middle school students), *Tutor* 2013
Relay for Life (Raising money to benefit cancer research), *Volunteer* 2013
I.L.R. (one-year program to engage in real-world business plan write-up for startups), *member* 2012

PROFESSIONAL SERVICE

Peer reviewer for journals including:
- ACS Applied Materials and Interfaces
- Micron
- International Journal of Nanomedicine
- Journal of Nanomaterials

REFERENCES

1. **Prof. Yaling Liu** (Ph.D. advisor)
Department of Mechanical Engineering and Mechanics
Lehigh University
Bethlehem, PA 18015, USA
Email: yal310@lehigh.edu Phone: 610-758-5839

2. **Prof. Xuanhong Cheng**
Department of Materials Science and Engineering
Lehigh University
Bethlehem, PA 18015, USA
Email: xuc207@lehigh.edu Phone: 610-758-2002

3. **Prof. Shu Yang**
Department of Materials Science and Engineering
University of Pennsylvania
Philadelphia, PA 19104
Email: shuyang@seas.upenn.edu Phone: 215-898-9645